Electron Holography for the Analysis of Magnetic and Electric Microfields in Nanostructured Systems

SILVIA SIGNORETTI

Diss. ETH No. 15170

Diss. ETH No. 15170

Electron Holography for the Analysis of Magnetic and Electric Microfields in Nanostructured Systems

A dissertation submitted to the
SWISS FEDERAL INSTITUTE OF TECHNOLOGY
ZURICH

for the degree of
Doctor of Natural Sciences

presented by

SILVIA SIGNORETTI
Dottore in Fisica
Università degli Studi di Bologna
born on the 5th February 1975
Citizen of Italy

accepted on the recommendation of

Prof. Dr. H. R. Ott, examiner
Prof. Dr. P. Stadelmann, co-examiner
Dr. C. Beeli, co-examiner

2003

To my family

Contents

Abstract

Electron holography has become a powerful tool for the analysis of electromagnetic fields of microstructures, in transmission electron microscopes down to nanometer resolution. In this thesis, the electron holography technique has been used on four different types of nanostructured samples for investigating their electromagnetic field. In fact, electron holography provides access to the phase shift and amplitude of an electron wave after it has traversed the sample, in relation to an electron wave passing through the vacuum, which is taken as a reference. This phase shift is caused by the mean inner electrostatic potential of the analyzed material and by electric charging with the electron beam. In the case of a magnetic material, a phase shift is produced due to the interaction of the electron wave with the magnetic microfield of the sample. Hence, information on the magnetization pattern inside the sample and on the magnetic leakage flux can be obtained.

This dissertation is divided into five chapters.

Chapter 1 is a brief introduction to the theory of electron holography with an overview to some specific applications. Moreover, a review of different techniques to image the magnetic structures of materials is presented.

Chapter 2 deals with the electron holography analysis of micrometric Fe particles with nanocrystalline structure, produced by mechanical milling. Electron holography has been employed to visualize the stray field emerging from isolated particles at selected temperatures $300 \leqslant T \leqslant 1200$K. By complementary x-ray diffraction and transmission electron microscopy investigations, a direct relationship has been established between the thermal variation of the stray field and of the particle microstructure. Indirect information on the magnetization pattern inside the particles

has been inferred. This work was carried out in collaboration with the group of Prof. E. Bonetti from the University of Bologna (Italy) and with Dr. G. Matteucci (Bologna University).

Chapter 3 is an extensive study on the magnetic properties of Fe nanoparticles, surrounded by an oxide surface layer, synthesized by gas-phase condensation and oxygen passivation.

Electron holography results on Fe nanoparticles with mean size of 50 nm, comparable to the characteristic Fe domain-wall thickness, indicate the existence of flux-closure magnetic configurations inside the particles. In particular, the magnetic phase maps, reconstructed from the holograms, are consistent with the presence of low-remanence vortex states of the magnetization.

Structural (x-ray diffraction, transmission electron microscopy and electron energy loss spectroscopy) and magnetic (SQUID magnetometry) characterization results for the core-shell Fe particles, with mean size varying from 6 to 50 nm, are also presented. Such results provide a clear picture of the relationship between magnetic properties and particle structural features and constitute a support to the electron holography conclusions.

This work was done in collaboration with the group of Prof. E. Bonetti (Bologna University), which also provided the samples, with Dr. G. Matteucci (Bologna University) and, for the magnetic measurements, with Dr. D. Fiorani (Istituto di Struttura della Materia, CNR Roma).

Chapter 4 is dedicated to the study of the stray field of CoPt magnetic force microscope (MFM) tips, produced by sputtering deposition. Numerical simulations allowed us to obtain quantitative values of the magnetic field due to the tip, as a function of the distance from the tip itself. This work was carried out in collaboration with the group of Prof. S.-H. Liou, from the University of Nebraska, Lincoln, who provided us the samples.

Chapter 5 is a study on the reliability of electron holography for the determination of the mean inner potential of dense materials, in particular Ni, Cu, Co and Ag. We found good agreement between the values measured experimentally and those calculated from the atomic scattering factors. The samples have been prepared by electrodeposition, in form of nanowires, by the group of Prof. B. Doudin from the University of Nebraska, Lincoln.

Abstract (Italiano)

L'olografia elettronica è ormai una tecnica ampiamente utilizzata nello studio dei campi elettromagnetici di microstrutture nei microscopi elettronici a trasmissione raggiungendo una risoluzione dell'ordine del nanometro. In questa tesi, l'olografia elettronica è stata impiegata su quattro tipi di campioni nanostrutturati diversi tra loro per l'analisi del loro campo elettromagnetico. Infatti, l'olografia elettronica fornisce informazioni sulla fase e sull'ampiezza dell'onda elettronica che attraversa un campione, in relazione ad un'onda elettronica che passa nel vuoto, considerata come onda di riferimento. L'ologramma registrato contiene quindi informazioni su tale sfasamento, causato dal potenziale interno medio del campione analizzato, dall'effetto del caricamento elettrico del campione dovuto al fascio elettronico del microscopio. Nel caso di un materiale magnetico, lo sfasamento è il risultato dell'interazione tra l'onda elettronica e il microcampo magnetico del campione. Quindi, è possibile ottenere informazioni sull'andamento della magnetizzazione all'interno di un campione magnetico e sul campo magnetico di fuga.

La tesi si divide in cinque capitoli.

Capitolo 1 È una breve introduzione della teoria dell'olografia elettronica con una breve introduzione a qualche applicazione specifica. In più, sono descritte diverse tecniche che permettono di visualizzare la struttura magnetica dei materiali.

Chapter 2 Sono presentati i risultati dell'analisi di olografia elettronica sull'evoluzione della magnetizzazione nelle particelle di Fe nanocristalline preparate per ball-milling. È stata stabilita una relazione diretta tra la variazione del campo di fuga con la temperatura e l'evoluzione della microstruttura delle particelle; infine sono state ricavate informazioni indirette sulla struttura magnetica interna delle particelle. Questo

attività di ricerca è stata svolta in collaborazione con il gruppo del Prof. E. Bonetti (Università di Bologna, Italia) ed è stata finanziata dall'istituto Nazionale di Fisica della Materia (INFM).

Capitolo 3 Il capitolo descrive un ampio studio sulle proprietà magnetiche di nanoparticelle di Fe sintetizzate mediante condensazione da fase vapore in atmosfera di gas inerte. Le particelle sono state passivate in-situ in atmosfera di ossigeno. I risultati dell'olografia elettronica su particelle di Fe, le cui dimensioni sono confrontabili con quelle tipiche dello spessore delle pareti di dominio, indicano l'esistenza di una configurazione magnetica interna della particella tale da consentire la chiusura parziale del campo di fuga. I diagrammi della fase magnetica, ottenuti processando digitalmente gli ologrammi, indicano la presenza di una configurazione della magnetizzazione di bassa rimanenza, di tipo a vortice. Questa conclusione è stata supportata da risultati di caratterizzazione magnetica e strutturale di particelle con size medio compreso tra 6 e 50 nm. A questo lavoro di ricerca hanno collaborato il gruppo del Prof. E. Bonetti (Università di Bologna), che ha fornito i campioni, il Dr. G. Matteucci (Università di Bologna) e il gruppo del D. Fiorani (Istituto di Struttura della Materia, CNR Roma).

Capitolo 4 Sono illustrati i risultati della analisi del campo di fuga di punte magnetiche per microscopi a forza magnetica (MFM). Simulazioni numeriche ci hanno permesso di valutare quantitativamente l'andamento e l'intensità del campo magnetico uscente dalla punta. Questo progetto è stato realizzato in collaborazione con il gruppo del Prof. S.-H. Liou (Università del Nebrasca, Lincoln) che ci ha fornito i campioni.

Capitolo 5 Il capitolo è dedicato alla presentazione dei risulatati di olografia elettronica utilizzata per determinare il potenziale interno medio in materiali densi, in particolare per Ni, Cu, Co e Ag. Abbiamo constatato che i risultati sperimentali ottenuti sono in buon accordo con quelli ottenuti calcolando il potenziale interno medio utilizzando i fattori atomici di scattering. I campioni sono stati preparati per elettrodeposizione sottoforma di nanofili dal gruppo del Prof. B. Doudin dell'Università del Nebrasca, Lincoln.

Preface

Since its invention 50 years ago by Dennis Gabor, electron holography has proven to be a powerful tool for the analysis of electric and magnetic microstructures in the transmission microscopes down to atomic resolution. Filling the gap of conventional electron microscopy, electron holography provides phase contrast for the mapping of electric and magnetic fields. Holography is a qualitative and quantitative method, giving direct evidence of the magnetization distribution inside and also outside thin samples.

The objective of this PhD thesis was to apply electron holography to the study of nanostructured magnetic and non-magnetic systems. It also demonstrated the potential and versatility of the electron holography technique for investigations at the mesoscopic level. To perform electron holography at high resolution, the capabilities of our microscope have been expanded by introducing a Lorentz lens, a special objective lens whose very weak magnetic field does not interfere with the sample.

Electron holography is a two step imaging technique. In the first step an interferogram between an object wave (running through the sample) and a reference wave (running in the vacuum) is recorded. The recorded interferogram, the holographic image, contains the phase shift between the two interfering waves. In the second step this hologram is analyzed and the phase and amplitude distribution is reconstructed. This is usually done with the help of a commercial software employing the Fourier transformation technique. This allows the separation of the autocorrelation function of the hologram from the two sidebands, which contain linear information about the object phase and amplitude distribution. By selecting and centering in Fourier space one of the sidebands, the phase and amplitude information can be reconstructed via an inverse Fourier transformation.

In this research work, electron holography has been applied to study four sets of samples, with the common feature being nanostructured systems, namely materials in which at least one of the microstructure components has nanoscale dimensions. For each of the chosen samples we carried out individual research activities. Over the past 15 years, the study of nanostructured systems has experienced an incredible expansion in both basic and applied research. This interest has been motivated by several factors: the ability to produce nanometer-scale features, the ever-increasing demand for miniaturization, the desire for materials that exhibit properties not encountered naturally and specific applications of magnetic materials.

More specifically, the goal of our work was two-fold:

1. To establish the necessary know-how and to extend the application possibilities of electron holography for a new type of transmission electron microscope that became operational at the ETH Zurich in April 2000: a Philips Tecnai F30.

2. To investigate the structure as well as the electromagnetic microfield of different nanostructured materials: micrometric Fe particles with nanocrystalline structure, Fe nanoparticles with a mean size of about 50 nm, magnetic force microscope tips and nanowires of different pure materials.

1 Imaging techniques for magnetic structures

The term "nanostructured" can be used to indicate a wide class of materials in which at least one of the constituent components is modulated on a length scale of less than 100 nm in one, two or three dimensions. Hence, it is possible to classify the nanostructured systems according to the *number of nanometer-scale dimensions* of one of the components. Magnetic systems with three small dimensions include: granular solids, namely assemblies of particles (or nanocrystallites) embedded in a matrix with different composition, structure or magnetic characteristics; granular films, made by heat treating multilayers of immiscible solids; nanograined layers grown on columnar films and magnetic dots. Thin films with columnar structures, aciculate particles and nanowires are examples of two small dimensions systems, whereas multilayered materials are characterized by just one dimension on the nanometer scale [1].

To understand nanostructured magnetic materials in detail, we should understand the electrical and magnetic properties at the surface and the interfaces between different components as well as the physical, chemical and magnetic properties at the atomic and nanoscale level. With regard to the imaging of nanostructured magnetic materials, the main problem is their small volumes, implying that very sensitive probes are needed. The quantitative mapping of magnetic induction distributions, which is important in the study of modern magnetic material and devices, such as thin films and multilayers, has been a topic of high interest in the last decades. Therefore, domain observation and micromagnetic theory went together in the study of magnetic microstructure.

The most popular experimental techniques for imaging magnetic materials at the atomic level are neutron scattering, interaction with polarized electromagnetic radiation, direct imaging using scanning probe microscopy (SPM) and transmission electron microscopy (TEM) [2, 3]. Although neutron scattering is ideal for this purpose, it has only been used sporadically because large samples are necessary for the measurements. Recent studies have mostly used the two other complementary techniques, SPM and TEM, to determine the magnetic structure of very small areas of the surface of an antiferromagnet, and the relative orientation of the magnetic moments at the interface between a ferromagnet and a antiferromagnet.

In the following paragraphs, various methods to observe the magnetic microstructure of materials are described. The presentation of these techniques is subdivided in imaging techniques using TEM, and techniques based on other physical principles for imaging and measurements. For a more general overview, a section devoted to the comparison of the various techniques is presented in figure 1.10.

1.1 Imaging magnetic structures using TEM

Modern transmission electron microscopes are instruments that are very well suited for the studies of a wide range of novel materials with unusual magnetic properties. The main motivation for their use is related to the need of a detailed knowledge of both the physical and the magnetic microstructure. Therefore, TEM studies are ideal if the structure-property relation is to be understood as well as materials with optimized properties are to be produced. As a matter of fact, many of the materials of interest are inhomogeneous with features requiring a spatial resolution below 50 nm for detailed investigations. Hence the interest towards the TEM technique is related to its very high spatial resolution and to the various types of interactions that occur when fast electrons hit a thin solid specimen, from which it is possible to extract detailed insight into compositional, electronic, as well as structural and magnetic properties. The resolution that is achievable depends largely on the type of the sought information and may be limited by the specimen itself. Typical resolutions achievable for structural imaging are 0.2 - 1.0 nm, for the extraction of compositional information 1 - 3 nm, and for magnetic imaging $2-20$ nm.

Magnetic imaging studies of magnetic nanostructures can be made in the as-grown state, in the remanent state and in presence of applied fields. From these, it is possible to derive basic micromagnetic information, the nature of domain walls configuration and many other phenomena. For example, if the analyzed specimens are thin films used for information storage in magnetic or magneto-optic recording, the imaged domains are directly related to the written "bits".

The history of magnetic imaging in the TEM started almost 50 years ago with the first observation of magnetic domain structures made by the Fresnel (or defocusing) mode [4]. Since then a number of different imaging and diffraction modes have been developed, including Foucault mode, coherent Foucault mode, differential phase contrast imaging, a range of holographic techniques as well as low-angle electron diffraction technique. A brief description of each technique will be presented in the following sections. The most extended section will be dedicated to the off-axis electron holography that has extensively been used in this PhD work.

1.2 Electron Holography

Electron holography is a special technique that provides access to the phase and amplitude of an electron wave after it has traversed the sample [5, 6]. The phase of the electron wave is altered by magnetic and electric fields, therefore, electron holography can be used to study magnetic materials. The quantitative measurement of the magnetic and electric fields in and around the sample is facilitated by the digital recording of holograms. Moreover, because no loss of resolution associated with defocusing can occur (see paragraph 1.3.1 below), the technique is inherently capable of achieving a spatial resolution of the order of 1 nm, depending on the optics of the particular microscope. Electron holography is an attractive technique for studying small regions which are usually not accessible with other magnetic imaging technique. A disadvantage is that the sample must be thinner than 0.5 μm because this techniques requires electron transmission through the sample.

Holography is now a widely known method and it was originally invented in 1948 by Dennis Gabor [7], as a way of breaking the resolution limit of electron microscopes. In

the 90's, Lichte performed his studies in the direction of high resolution electron holography [8–10]. By a-posteriori corrections of aberrations, holography has transcended the resolution limit of conventional TEM down to atomic resolution. Today one probes structures with a resolution of 0.1 nm. By determining the atomic species from the magnitude of the electron phase shift, it also began to contribute to the solution of the *Which Atoms are Where*-problem [11]. Since this topic is not related to our application of the technique, we do not go into further details.

Electron holography relies on the interference of two coherent electron waves to produce a hologram. Subsequently, the hologram must be reconstructed in order to retrieve a complex electron wavefunction that carries phase and amplitude information about the sample. At least 20 forms of electron holography have been suggested [12], and many of these have also been realized in practice. The most commonly used is called "off-axis electron holography". To perform this kind of analysis, the electron microscope must be equipped with an electrostatic biprism, developed by Möllenstedt and Düker [13], which allows for the overlap of a reference wave (the wave that runs in the vacuum) with the object wave (the wave scattered by the object).

Traditionally, wavefunction reconstruction from electron holograms has been achieved off-line, using laser optical methods [14]. The introduction of slow-scan charge-coupled device (CCD) cameras for digital recording together with progress in computer technology has allowed a rapid spread of on-line digital processing of electron holograms, giving way to quantitative electron holography [15, 16].

Electron holography has a long history of applications to electrostatic fields. Some typical examples may be found in references [17–21]. Concerning its application to magnetic materials, electron holography has been limited to rather poor spatial resolution ($>$ 10 nm) because of the need to locate the sample in a field-free region to prevent saturation of the magnetization. Important milestones include the imaging of the field distribution associated with magnetic recording tapes [22], experimental confirmation of the magnetic Aharonov-Bohm effect [23], and observations of vortex lattices in type II superconductors [24]. In most TEM applications, the strong objective lens was usually switched off, and imaging was achieved using the remaining diffraction/projector lenses.

In order to achieve improved resolution without affecting the magnetic field of the specimen [25], special minilenses can also be inserted into the bore of the objective lens (see following paragraph).

1.2.1 Off-axis Electron Holography

The geometry of off-axis electron holography in the conventional TEM is illustrated in figure 1.1. The illumination, usually from a field emission gun (FEG) electron source, has to be coherent, thus the illumination is strongly defocused in order to get a parallel beam.

For many holographic experiments the phase shifts carried by the object wave are relatively small and, to a first approximation, one can assume that the fringes remain parallel to the biprism wire. In this case, the coherence must be kept only in the direction perpendicular to the fringes. The electron beam is strongly defocused only in one direction to obtain a beam with an elliptical cross section, the major axis being perpendicular to the biprism fiber. In this way, the coherence is maximized in one direction and the electron flux is optimized in the region of interest (see figure 1.2). It is then important that the angle between the major axis of the ellipse and the biprism fiber is 90° to a very high precision. Deviations from this configuration will result in a fast reduction in fringe contrast [26, 27].

The most common position for the biprism is just after the objective lens, in one of the selected-area apertures. In this case the interference pattern is formed at the first image plane, which is translated electron-optically below the selected area plane by increasing the excitation of the diffraction or intermediate lens so that the image is located just below the biprism. The spacing of the interference fringes and the extent of their overlap are related to the magnification of the image in this plane [16]. This magnification depends on the methods used to ensure that the magnetic sample is located in a field-free region. For example, by turning the objective lens off, the sample would be examined in a low magnification mode and correspondingly in a larger field of view, but with a relatively poor image resolution. The use of a weak imaging lens positioned in the bore of the lower part of the normal objective lens, the so-called Lorentz lens, allows for magnifications up to 245’000 x, when the so called energy filtered TEM mode (EFTEM) is on. This operational mode is described in paragraph 1.7. In figure 1.3 the position of the Lorentz

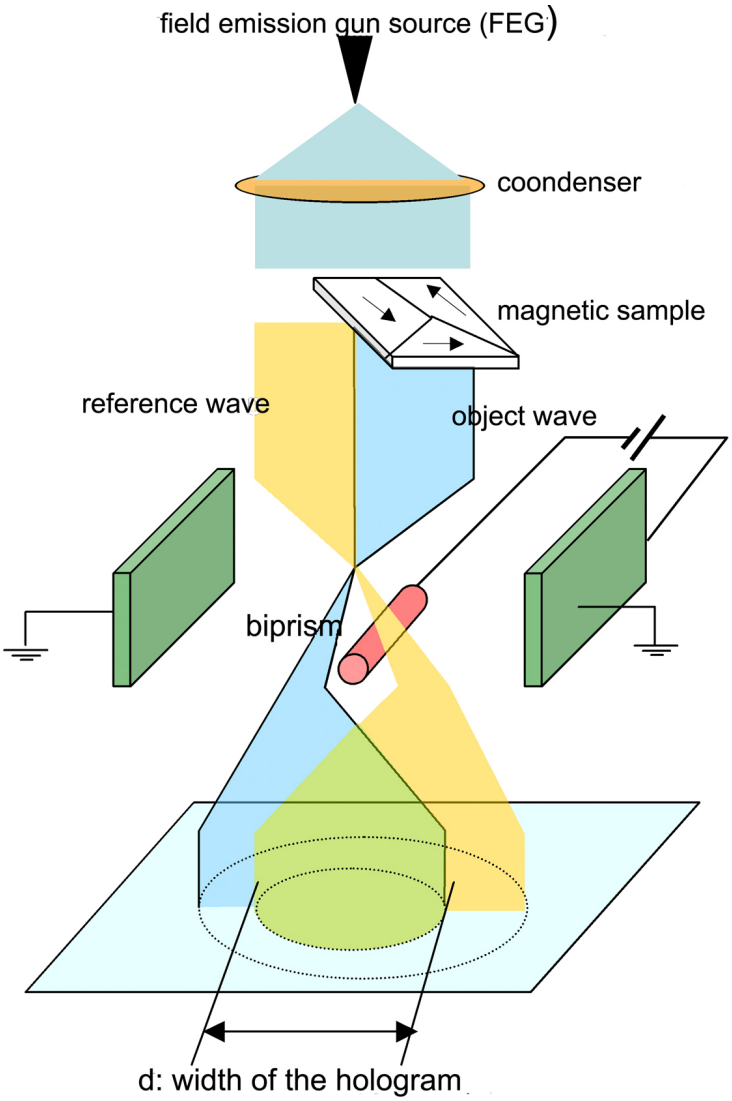

Figure 1.1: Schematic diagram showing the setup used for off-axis electron holography in the TEM. Essential components are the field emission gun (FEG) used to provide coherent illumination and the electrostatic biprism that causes the overlap of object and reference waves, respectively.

lens is shown. In such a configuration the sample is placed in an almost field-free space, with an induction density of less than 10 Gauss.

Usually the biprism is a thin metallic wire (< 0.5 μm diameter) or quartz fiber coated with gold or platinum, which is electrically biased by means of an external direct current power supply, typically to a voltage ranging from 50 to 200 V. It is useful if the

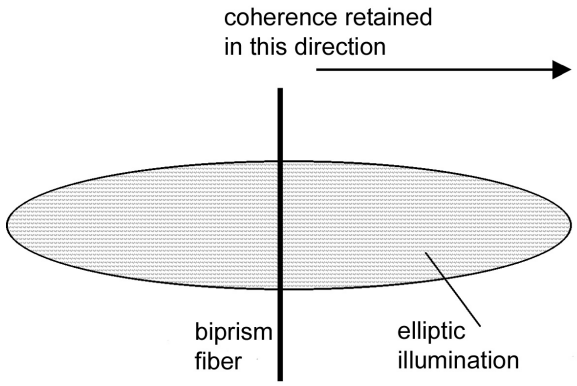

Figure 1.2: Schematic illustration of the astigmatic illumination used for electron holography. The coherence is retained in the direction of the major axis of the ellipse, perpendicular to the the biprism fiber.

biprism can be rotated around an axis parallel to the electron beam direction, as this allows for flexibility in aligning the interference fringes with respect to features of interest in the sample. The voltage used to form a hologram depends greatly on the experiment in progress. The importance of the fringe contrast is related to the resolution of the phase map in the reconstructed image and thus any phase measurement will have a higher signal to noise ratio (S/N-ratio) for higher fringe contrast. Inevitably, the biprism will become a little dirty with time: small particles tend to stick to the biprism and can take up charge under the electron beam. This will influence the fringe pattern and again lead to erroneous phase images. It is therefore important to find a clean part of the biprism wire which is used to form the interference pattern.

The most popular method to record holograms is to use a CCD camera. The advantages of this method are the following: the CCD response is linear, it has a high detection quantum efficiency (10 counts for 15 electrons) and the information is recorded digitally, thus facilitating the quantitative analysis and the processing of the images [28]. Most CCD cameras are only 1024 x 1024 pixels in size and this limits the number of hologram fringes that can be sampled accurately. 2k x 2k pixels cameras have been introduced to overcome this limitation. The spatial resolution of amplitude and phase images is determined primarily by the effective pixel size of the hologram, as well as by the size of the extracted sideband used for reconstruction (see below).

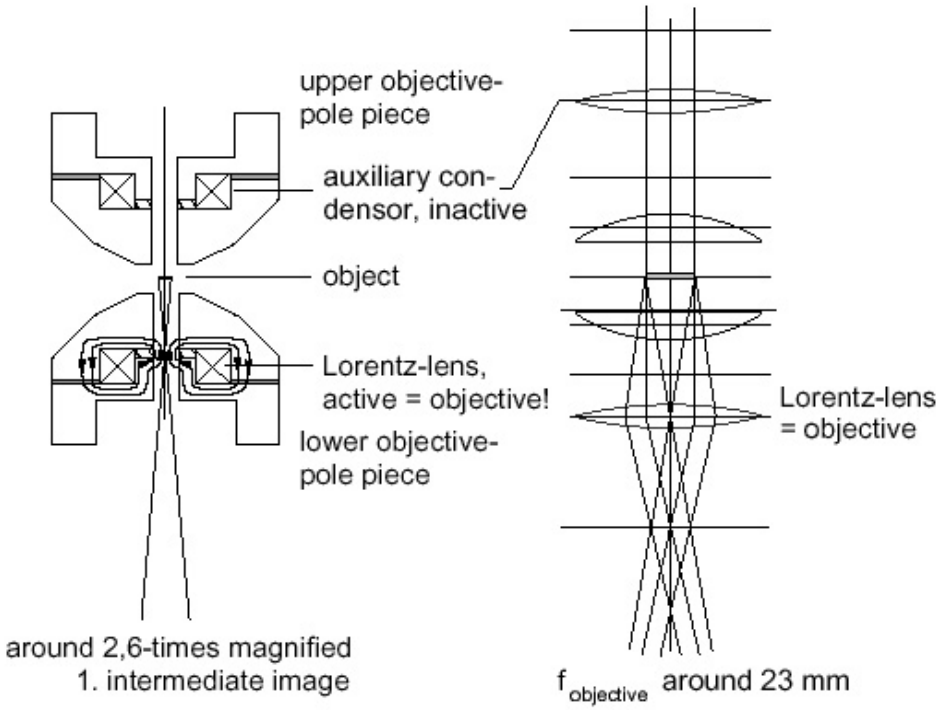

Figure 1.3: Schematic illustration of the position of the Lorentz lens in the column of the microscope (Tecnai F30 from FEI Company).

The intensity distribution in the holographic interference fringe pattern formed by two coherent waves can be written in the form [29]

$$\begin{aligned} I(x,y) &= |\Psi_1(x,y)|^2 + |\Psi_2(x,y)|^2 + |\Psi_1(x,y)||\Psi_2(x,y)|[e^{i(\phi_1-\phi_2)} + e^{-i(\phi_1-\phi_2)}] \\ &= A_1^2 + A_2^2 + 2A_1A_2\cos\phi(x,y) \end{aligned} \tag{1.1}$$

where Ψ is an electron wavefunction, $\phi(x,y)$ is the relative phase shift, and the subscripts 1 and 2 refer to the reference and object waves, respectively. Considering q_f the carrier frequency, μ the contrast of the fringes ($\mu = I_{max} - I_{min}/I_{max} + I_{min}$), A(r) and ϕ(r) the amplitude and phase of the image wave that modulate the cosinusoidal fringe pattern and I_{inel} the inelastic (incoherent) background of the hologram, we can rewrite the intensity of the hologram as follow:

$$I(\mathbf{r}) = 1 + A^2(\mathbf{r}) + I_{\text{inel}}(\mathbf{r}) + 2\mu A(\mathbf{r})cos(2\pi q_f \cdot \mathbf{r} + \phi(\mathbf{r})) \tag{1.2}$$

The recorded hologram thus consist of a series of sinusoidal fringes that are superimposed on a normal bright-field image. To illustrate the technique, the reconstruction of an off-axis electron hologram of a nickel nanowire is represented in figure 1.4. Figure 1.4a shows the hologram recorded when the wave passing through the nanowire is superimposed onto the reference wave passing through the vacuum, which avoids any influence of the sample. Figure 1.4b shows the distribution of intensity in the Fourier transform of the hologram, equivalent to the intensity distribution in the back-focal plane of a reconstructing lens system. The three separate diffraction patterns are clearly visible. Each of the two conjugated sidebands contains the complete information about the phase and the amplitude of the image wave, while this information is unavailable from the central autocorrelation function. The separation of these sidebands arises from the respective tilt of the object and reference waves and depends on the voltage applied to the biprism. One of the side-bands is selected (figure 1.4c) to perform an inverse Fourier transform resulting in the amplitude and phase distribution (figure 1.4d and e). Across the nanowire a discontinuity of 2 π in the phase is experienced. Figure 1.4f represents the reconstructed phase map amplified 6 times, to enhance the number of equiphase lines, where the gray scale jumps from black to white. The use of one of these sidebands in the reconstruction process gives rise to the term "off-axis" electron holography.

The Fourier transform (FT) of the hologram is thus composed of three parts:

$$FT\{I(\mathbf{r})\} = \begin{cases} FT\{1+A^2(\mathbf{r})+I_{\text{inel}}(\mathbf{r})\} & \textit{Central band} \\ +\mu FT\{A(\mathbf{r})e^{-i\phi(\mathbf{r})}\}\bigotimes\delta(q+q_{\text{f}}) & \textit{Side band}1 \\ +\mu FT\{A(\mathbf{r})e^{i\phi(\mathbf{r})}\}\bigotimes\delta(q-q_{\text{f}}) & \textit{Side band}2 \end{cases} \tag{1.3}$$

The central band (or autocorrelation) is the FT of a conventional image. The two sidebands at $q = \pm q_{\text{f}}$ are the Fourier transforms of the complex image wave function which contains the phase information ϕ(r) that we desire.

The phase is usually calculated modulo 2π, which means that 2π phase discontinuities that are not related to particular specimen features, appear at positions in the phase image at which the phase shift exceeds this amount. Frequently, the phase must be unwrapped carefully using suitable phase-unwrapping algorithms before a reliable interpretation of the image features is possible [16]. It is also customary to record reference

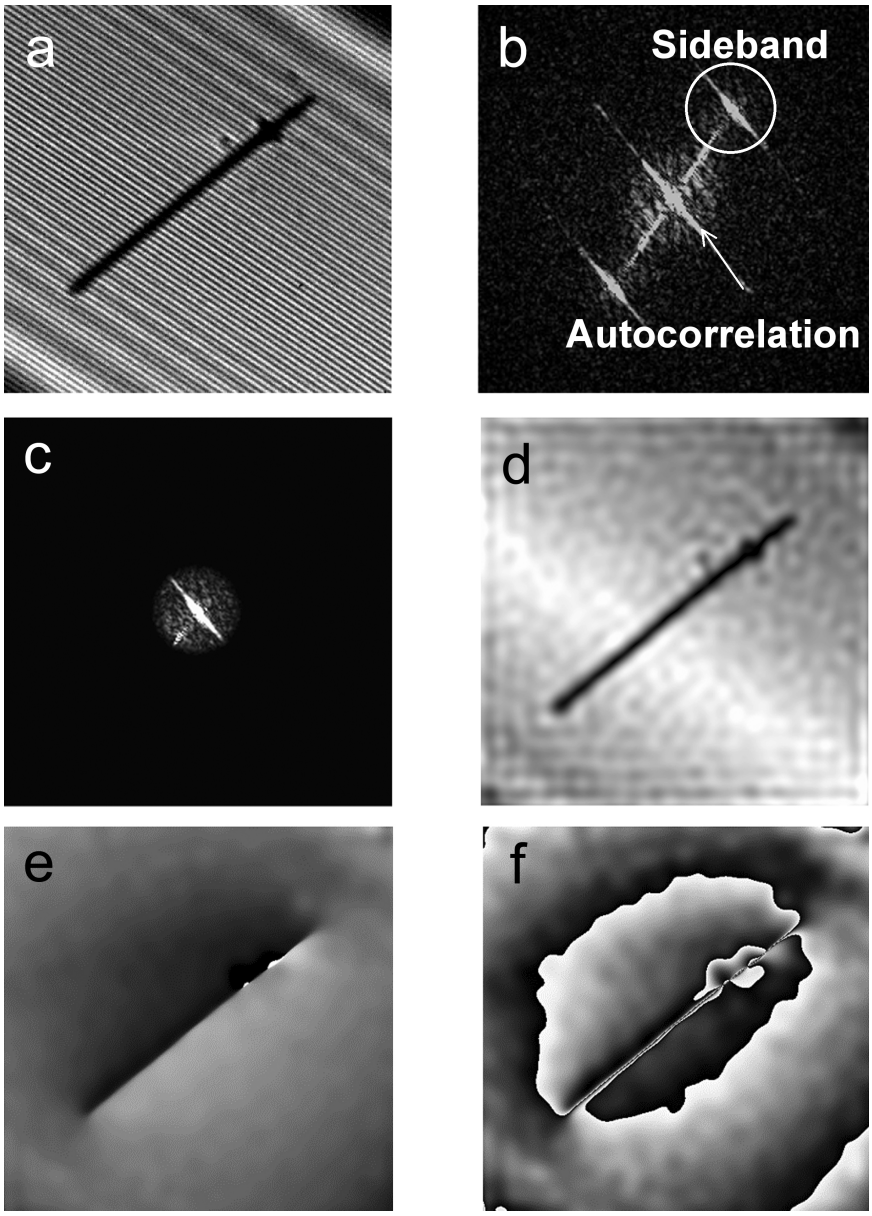

Figure 1.4: Reconstruction of the off-axis TEM hologram of a nickel nanowire. (a) Portion of the hologram crossed by fine interference fringes. (b) The Fourier transform of the hologram showing the central pattern and the two side-band patterns. (d, e) The amplitude and phase image, reconstructed from the selected side band (c), (f) the phase image amplified 6 times.

holograms in the absence of the sample so that artifacts associated with local irregularities of the imaging and the recording systems can be cancelled out.

Reconstruction of holograms with the use of a reference hologram is the most often used method for the reconstruction of the amplitude image and the phase image. Deviations from the ideal wave front situation in the electron microscope cause artifacts in the reconstructed phase image and amplitude image. These artifacts are also recorded in the reference hologram. It is therefore obvious that a reference hologram is used to cancel artifacts in the reconstructed amplitude and phase image.

As the fringe spacing is the same both in the reference and the regular hologram, it is sufficient for the reconstruction of both holograms to evaluate the position of the sideband in Fourier space from the reference hologram. Two complex images are obtained from an inverse Fourier transform after the regular and the reference hologram are isolated from the autocorrelation, as discussed above. An accuracy of $\pm 1/2$ pixel or less is suitable for the selection of the center of the sideband in this case, because the effects caused by a sideband not perfectly centered will be counterbalanced between the reference and the regular hologram in the last processing step. Dividing the reconstructed complex image by the (reconstructed) complex reference image yields the final complex image wave function of the object. In the ideal case, the improved (complex) image wave function is free of distortions, flat in the vacuum (unless electric or magnetic fields are present) and free of Fresnel fringes.

Softwares for reconstructing a hologram are available commercially as plug-ins for Digital Micrograph (HoloWorks [30], HolograFREE [31]).

1.2.1.1 Magnetic fields

In order to examine the magnetic configuration of a specimen, the magnetic field of the objective lens must be close to zero at the specimen site, therefore the objective lens is turned off and a Lorentz lens [25] is used. We consider a thin film of a magnetic material lying in the xy plane. The phase difference detected in the image between the reference wave and the object wave can be written as [6, 32]

$$\Delta\phi(x,y) = C_E \int V_{cryst}(x,y,z)dz - \frac{2\pi e}{h} \int\int B(x,y)\cdot dS, \tag{1.4}$$

where the first integral is taken along a trajectory parallel to the beam direction z, V_{cryst} is the crystal potential of the object, B is the magnetic flux density and S is the area between the two trajectories going from the source to the detector through the vacuum and the sample respectively, both ending in the same point at the electron hologram. C_E is a wavelength-dependent constant, determined from the electron-optical refractive index in the absence of a magnetic field [33]

$$n(r) = \frac{\lambda}{\lambda_m} = \left[\frac{2(E-V)E_0 + (E-V)^2}{2EE_0 + E^2}\right]^{1/2} \tag{1.5}$$

where E is the kinetic energy and λ the wavelength of the electron beam and E_0 is the rest mass energy of the electron. This formula can be simplified if it is assumed that $V(r) \ll E$ and E_0 (e.g., the mean inner potential of silicon is $V(\mathrm{r}) = V_i = -13.5$ V),

$$n(r) \approx 1 - \frac{V(\mathrm{r})}{E}\frac{E_0 + E}{2E_0 + E} + ...; \tag{1.6}$$

with n(r) $\gtrsim 1$ because $V(\mathrm{r})$ in matter is negative. Accordingly, an optical path difference $\Delta = (n-1)t$ and hence the phase shift ϕ, that corresponds to a layer of thickness t, can be introduced by writing

$$\phi = \frac{2\pi}{\lambda}\Delta = \frac{2\pi}{\lambda}(n-1)\,t = \frac{2\pi e}{\lambda E}\left(\frac{E_0 + E}{2E_0 + E}\right) V_i\, t = C_E\, V_i\, t \tag{1.7}$$

(for example, at $E = 300$ keV, $C_E = 6.52 \cdot 10^{-6}$).

If neither V nor B vary with z, and neglecting magnetic and electric fringing fields outside the sample, the expression 1.4 can be simplified to

$$\Delta\phi(x,y) = C_E V_{\mathrm{cryst}}(x)t(x) - \frac{2\pi e}{h}\int\int B_\perp(x,y)\cdot dS \tag{1.8}$$

where $B_\perp$ is the component of the magnetic flux normal to the plane determined by S. Differentiation with respect to x leads finally to

$$\frac{\partial\Delta\phi}{\partial x}(x) = C_E\frac{d}{dx}\{V(x)t(x)\} - \frac{2\pi e}{h}B_\perp(x,y)t(x). \tag{1.9}$$

In a sample of uniform thickness and composition, the first term of equation 1.9 disappears, and the in-plane induction is thus proportional to the phase gradient.

When the magnetic flux is not confined to the sample and the leakage flux spreads into the vacuum, the reference wave is no longer a plane wave because it will be passing through a region of space in which $B \neq 0$. Thus $\Delta\phi$ is now the phase difference experienced by the wavefront passing through two different parts of the B-field, i.e.,

$$\Delta\phi(x) = \phi(x - d/2) - \phi(x + d/2) \tag{1.10}$$

where x is a coordinate measured perpendicular to the biprism axis and to the electron beam direction; d is the "interference distance", i.e., the distance between two points of the ray paths that meet under the action of the biprism [34]. This distance d is also the width of the interference region, i.e., the hologram width.

The retrieval of the phase information is performed by digital processing of the hologram. As a result of this procedure, contour lines in the phase image are obtained which represent the loci of points with constant phase and can be interpreted directly as magnetic flux lines of the leakage field around the object. A quantitative evaluation of the magnetic flux can be obtained since between two adjacent contour lines a magnetic flux of $h/e = 4.1 \cdot 10^{-15}$ Wb is included, thus a phase difference of 2π corresponds to a magnetic flux of h/e. Previous work by Frost *et al*. [35] concerning strong leakage fields (causing a phase shift of several tens of 2π) shows, although the reference wave is modulated by the field around the particle, the qualitative configuration of the leakage field is not significantly affected.

1.2.1.2 Electric fields and thickness of a sample

If the sample is free from magnetic fields then from equation 1.4, the phase difference between a wave passing through vacuum and one through the sample is given by

$$\Delta\phi(x,y) = C_{\mathrm{E}} \int V(x,y,z)dz \tag{1.11}$$

where V is the electrostatic potential of the object which may include a contribution from permanent electric fields. The constant C_E is defined in equation 1.7.

However, in many cases the sample is not uniform in thickness and in the recorded phase difference there are contributions both from the magnetic field and the mean electrostatic inner potential. The latter contribution can be calculated as

$$\Delta\phi = \frac{2\pi e}{h} V\tau = \frac{2\pi e}{h}\frac{Vt}{v_e} \tag{1.12}$$

where τ is the transit time of an electron through a film, and is consequently given by the film thickness t divided by the electron velocity v_e. As a result, the contour lines of $\Delta\phi$ cannot easily be interpreted in physical terms as they can be in the case of purely electric or purely magnetic fields.

The method used to separate the electric and magnetic effects is based on the differing effects of time reversal on electric and magnetic fields [36]. Consequently, in order to experimentally separate electric from magnetic phase shifts, it is necessary to record two holograms of the same feature of the specimen. These holograms are taken one after the other, the second one extracting the sample from the microscope and reversing it upside-down by 180°. In these holograms, the electric contribution (mostly related to the thickness) to $\Delta\phi$ is the same, but the magnetic contribution is of opposite sign.

The occurrence of the opposite sign can simply be explained by using the equation for the electron motion in the electric and magnetic fields, E and B, respectively,

$$m\frac{d\mathbf{v}}{dt} = -e(\mathbf{E} + [\mathbf{v}\times\mathbf{B}]) \tag{1.13}$$

If the electron beam is incident to the specimen along the same trajectory but from the opposite direction, the situation is equivalent to a time reversal transformation $t \rightarrow -t$ and $\mathbf{v} \rightarrow -\mathbf{v}$. Thus the equation of motion becomes

$$m\frac{d\mathbf{v}}{dt} = -e(\mathbf{E} - [\mathbf{v}\times\mathbf{B}]). \tag{1.14}$$

Figure 1.5: Schematic illustration of the magnetization reversal employed to extract separately the electric and magnetic information. The sample is reversed by 180 degree with respect to an axis that is in the optimal case perpendicular to the magnetization vector.

For purely electric cases (B = 0), the resultant trajectory is represented exactly by the original equation 1.13. For $B \neq 0$, however, the trajectory is not the same unless the direction of the magnetic field B is reversed (-B) (see figure 1.5).

The phase differences due to the electric and magnetic potentials are then represented by $\Delta\phi_E$ and $\Delta\phi_M$, respectively, the total $\Delta\phi$ is given by $\Delta\phi_E + \Delta\phi_M$. When the electron beam is incident to the specimen from the opposite side, the total $\Delta\phi$ is given by $\Delta\phi_E - \Delta\phi_M$. If the summation and subtraction of the two phase differences are calculated, the thickness contours ($2\Delta\phi_E$) and magnetic lines of force ($2\Delta\phi_M$) can be separately observed [36]:

$$\Psi_1 = A_1 exp[i\phi_1] \qquad 1.\ Hologram \tag{1.15}$$

$$\Psi_2 = A_2 exp[i\phi_2] \qquad 2.\ Hologram \tag{1.16}$$

where the phases of the two wave function relative to hologram 1 and hologram 2 are given as

$$\phi_1 = \phi_E + \phi_M \tag{1.17}$$

$$\phi_2 = \phi_E - \phi_M \tag{1.18}$$

and therefore, by multiplication and division of the two wave functions it is possible to have two new wave functions that contain information only related to the magnetic field

and only related to the electric field, respectively

$$\Psi_1 \cdot \Psi_2 = A_1 A_2 exp[i(\phi_1 + \phi_2)] = A_1 A_2 exp[i2\phi_E] \quad (1.19)$$

$$\Psi_1 / \Psi_2 = \frac{A_1}{A_2} exp[i(\phi_1 - \phi_2)] = A_1 A_2 exp[i2\phi_M] \quad (1.20)$$

Due to the factor 2 in front of the phase, the reconstructed phase map is already amplified by a factor of 2.

1.3 Other TEM magnetic imaging technique

1.3.1 Fresnel and Foucault imaging: Lorentz microscopies

TEM imaging techniques where the sample is in a magnetic field free space are commonly called Lorentz microscopies. This is due to the fact that the electrons of the beam are influenced by the Lorentz force, thus leading to the contrast features caused by the magnetic structure of the sample. The most commonly used Lorentz imaging techniques for revealing magnetic domain structures are the Fresnel (or defocused) and Foucault imaging modes [37] and both can be practiced in a conventional TEM without modification, however offering limited resolution. The schematics of how magnetic contrast is generated are shown in figure 1.6.

We consider a simple specimen, comprising three domains separated by two 180° domain walls. In Fresnel microscopy the imaging lens is taken out of focus so that the optical object plane is no longer coincident with the specimen plane. Narrow bright and dark (bands) contrasts in the image now indicate the positions of the domain walls. The fringe structure visible inside the bright (band) contrast (called convergent domain wall image) reflects the fact that a simple ray treatment is incomplete and that the detail, in this case interference fringes, can arise due to the wave nature of the electrons. In Foucault microscopy, a contrast forming aperture must be present in the plane of the diffraction pattern. The aperture is used to suppress one of the two components into which the central diffraction spot is split due to the deflections of the beam suffered as the electrons pass through the magnetic domains in the specimen. In general, the splitting of the central spot

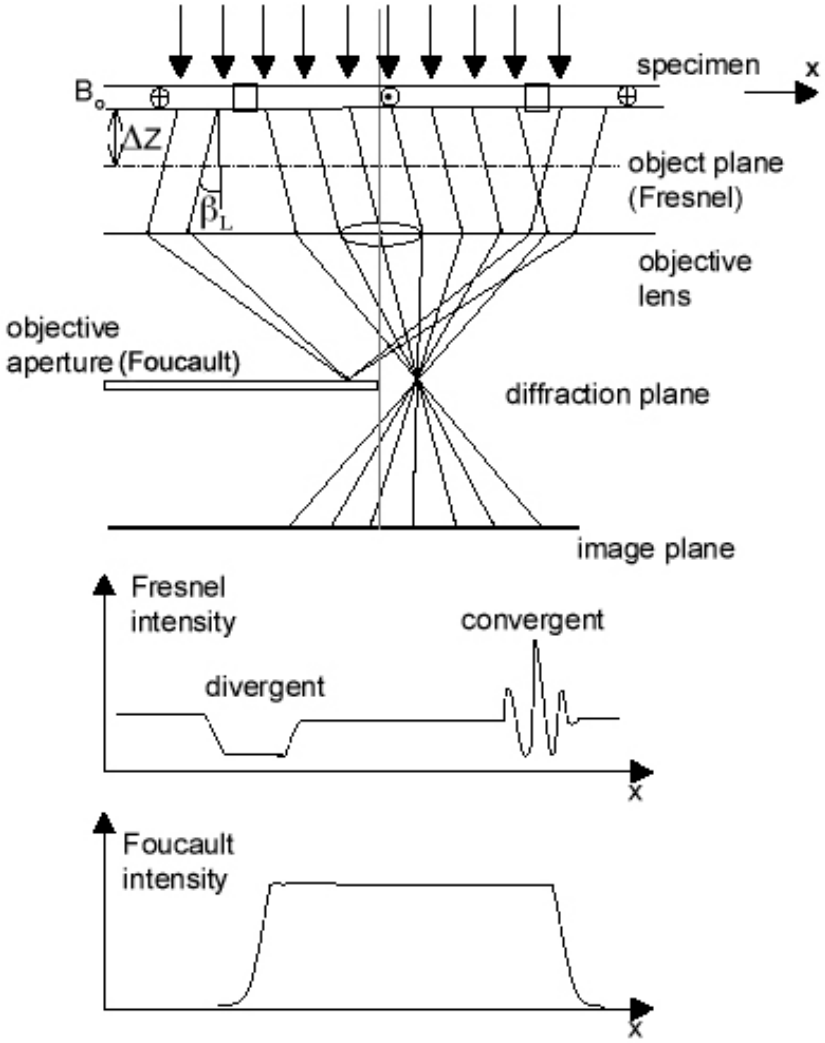

Figure 1.6: Scheme of Fresnel and Foucault imaging.

is more complex than for the simple case considered here. The domain contrast can be seen in the image as a result of the partial obstruction of the diffraction spot. Bright areas correspond to domains where the magnetization orientation is such that electrons are deflected through the aperture and dark areas to those where the orientation of magnetization is oppositely directed and thus the electrons passing through this region are blocked by the aperture (see figure 1.7, [38]).

Fresnel and Foucault microscopy together are the preferred techniques for in situ experimentation because they are generally fairly simple to implement and they provide a clear picture of the overall domain geometry and a useful indication of the directions

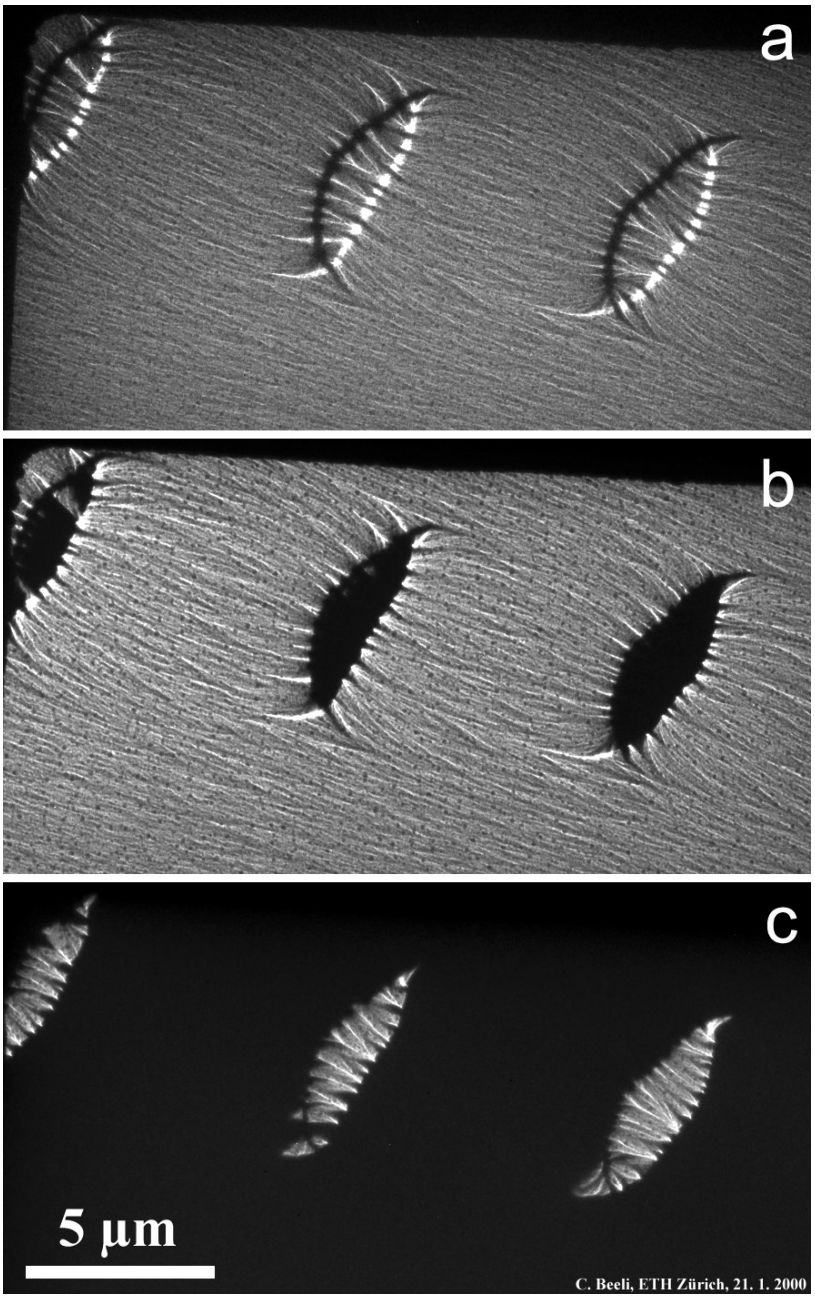

Figure 1.7: (a, b) Fresnel and (c) Foucault image of a Co film

of magnetization in the larger domains. However, both imaging modes suffer from the disadvantage that the relation between image contrast and the spatial variation of magnetic induction is usually non-linear [39]. Thus the extraction of quantitative data, especially from regions where the induction varies rapidly, is problematic. To partially solve the problem it is preferable to use the novel coherent Foucault imaging mode, for which a

TEM equipped with a field emission gun (FEG) is required [40, 41]. Here the opaque aperture is replaced by a thin phase-shifting aperture, an edge of which must be located on the optic axis. For example an amorphous film containing a small hole works well if the aperture and the thickness are chosen so that the experienced phase difference is π. The technique can only be applied close to a specimen edge because the beam passing through free space is considered as a reference beam. Under such conditions the magnetic interferogram has the same form of the one obtained by electron holography.

1.3.2 Low angle diffraction

A different way of determining quantitative data from the magnetic samples with the help of a TEM is by direct observation of the form of the split central diffraction spot. This is achieved by low angle diffraction patterns (LAD). The main requirement for low angle diffraction is that the magnification of the intermediate and the projector lenses of the microscope is sufficient to reveal the small Lorentz deflections, $\approx 10^{-6}$ to 10^{-4} rad. Thus, camera constants (defined as the ratio of the displacement of the beam in the observation plane to the detection angle itself) in the range of 50 to 1000 m are typically required. Furthermore, highly coherent illumination is essential in order to observe fine details of the detailed form of the low angle diffraction pattern. In practice, the angle subtended by the illuminating radiation at the specimen must be considerably smaller than the typical deflection angle caused by the magnetic domains under investigation. The latter condition is particularly easy to fulfill in a TEM equipped with an FEG electron source. The LAD method complete the deficiency of Fresnel and Foucault imaging.

1.3.3 Differential phase microscopy

Differential phase (DPC) microscopy [42,43] is based on a scanning transmission electron microscope. The sample is scanned with a fine electron beam focused to a spot on the sample. In the diffraction plane of the microscope, a special split detector (typically four segments) converts the diffracted beam into a signal that may be displayed on a video screen or digitized and stored in a memory (figure 1.8). If the detector consists of two halves, the difference between the two signals is proportional to the magnetic

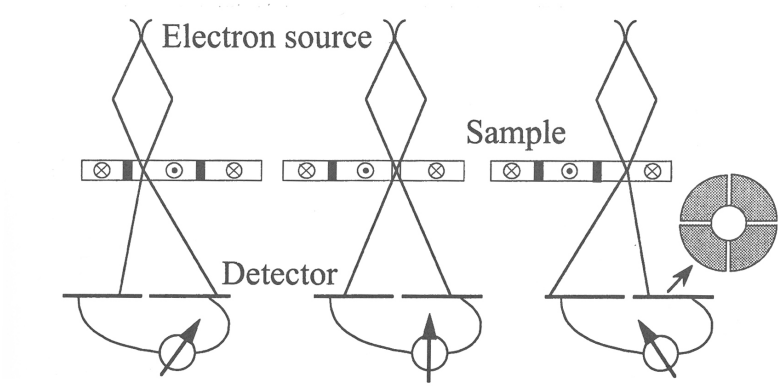

Figure 1.8: Schematic drawing of DPC imaging.

deflection of the beam and therefore to the average magnetization component parallel to the axis along which the detector is split. By rotating the detector, the microscope becomes sensitive to other components of the magnetization. In practice, a quadrant detector is used, whereby the signals from different elements can be combined in various ways. If stray fields outside the sample are neglected (as is typical for soft magnetic materials), the combination of two such images gives a quantitative determination of the magnetization directions. Morrison *et al*. managed to work with a beam spot size < 10 nm using a FEG microscope, with the specimen located in the field-free space [44].

1.4 Different magnetic imaging techniques

1.4.1 Scanning electron microscopy with polarization analysis (SEMPA)

The secondary electrons ejected from the specimen during the scanning process in a scanning electron microscope retain the spin polarization of their initial state. Initial studies [45] of the energy distribution of the spin polarized electrons from a ferromagnetic specimen suggested that measurements of this type may be useful for magnetic imaging with SEMPA [46–50]. The advantages lies in a vector determination of the magnetization direction and its ability to image large areas of a specimen with a spatial resolution of the order of up to 10 nm.

The determination of the in-plane magnetization in a particular direction requires the measurements of both in-plane polarizations. If one considers the two in-plane directions as *x* and *y* then the polarization along the *x* direction is given by $P_{\mathrm{x}} = (N_+ - N_-)/(N_+ + N_-)$ where the N_+ and N_- are the number of imaged electrons with a polarization parallel and antiparallel to the *x*-axis. Both in-plane magnetization components are determined during the SEMPA imaging process. By either diverting the beam to a second spin analyzer or by using a spin rotator, the magnetization component perpendicular to the plane may be determined [51]. However, this component is of interest only for certain samples and is not normally measured.

The spatial resolution of SEMPA is essentially that of the primary SEM beam which in turn is determined by a number of experimental conditions. The principle factor is the beam diameter, which defines the smallest spot that can be analyzed. It also determines the magnitude of the current and thus with a decreased current the time for imaging increases. Therefore problems with drift, sample deterioration, etc. currently limit the resolution to the order of 10 nanometer. Just as a SEM image, SEMPA images have a large depth of focus and the ability to image small areas at high magnification or large areas at lower magnification. A limitation of this technique is its sensitivity to magnetic fields: any stray or applied fields will generate a Lorentz force on the electrons, therefore the external magnetic fields must be less than 10 Oe.

1.4.2 Kerr microscopy

Magneto-optical (MO) imaging is another technique for imaging the magnetic domains in magnetic materials. It is based on the interaction of photons with the electron spins via the spin orbit coupling which provides an image contrast proportional to the magnetization. This makes the technique non-invasive, allowing for probing the direction of the magnetization without any alterations of the magnetization. In addition, photons have relatively large penetration depth of about 20 nm and are thus bulk sensitive [52, 53]. Since the sensitivity depends on the spin-orbit coupling, the largest magneto-optical signals arise from the rare earths and alloys containing rare earths.

The digital difference technique is the present standard for Kerr microscopy. The main purpose of difference techniques is the subtraction of the non-magnetic background

so that the resulting image can be improved by averaging and contrast enhancement. The background can be determined by measurements in the saturated state or can be an averaged image obtained during AC excitation. MO imaging also provides the possibility to determine the vector components of the magnetization. Furthermore, MO signals are unaffected by an external applied magnetic field (although some optical components exhibits MO effects). Provided the signal intensity is sufficient, it is possible to detect hysteresis loops. With this technique it is possible to image large areas while obtaining microscopic information with a spatial resolution of the order of 150 nm.

1.4.3 Magnetic force microscopy

The magnetic force microscope (MFM) is an extension of the atomic force microscope (AFM). In recent years MFM has become a standard tool to investigate surface magnetism, since it allows for the visualization of the stray field distribution above the surface of a sample. The principle of an MFM is shown in figure 1.9.

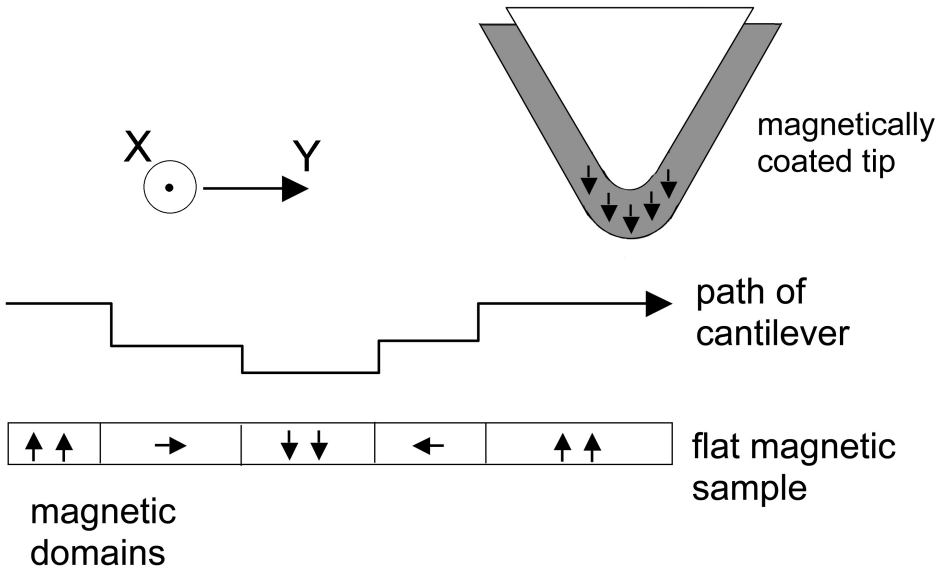

Figure 1.9: Schematic representation of the MFM technique.

The MFM consists of a flexible cantilever, which carries a ferromagnetic tip-shaped probe at its end. When a magnetic surface is brought close to this tip, they will interact

by the magnetic stray field. Magnetic force microscopy is a non-contact technique and during scanning the sample is kept at a distance of several nanometers from the tip. The interaction between the tip and the sample can be measured by a detector (for instance a piezoelectric transducer) which is placed on the back side of the cantilever. When the sample is moved with respect to the tip a one dimensional array of interaction data is measured and stored in the computer. The direction of this motion is called the fast scan direction (X). A number of parallel scan lines will form a two dimensional array of data in the computer (Y). A computer assigns grey or color values to different strengths of interaction forming a microscopic image of the interaction on the sample surface. Little sample preparation and no special vacuum conditions are required for operation, but the images are difficult to quantify or to interpret.

Provided there is no mutual disturbance of the magnetic properties of the sample and the magnetic tip, a situation which can experimentally be controlled under certain conditions [54, 55], MFM imaging allows to qualitatively characterize, e.g., the domain structure of a given sample being either hard magnetic [56] or soft magnetic [57]. Even the nature of domain walls, either Bloch- or Néel type [55, 58, 59], can be analyzed qualitatively.

However, an image taken with a magnetic tip contains information about both the topography and the magnetic properties of a surface. Which effect dominates depends on the distance between the tip and the surface, because the interatomic magnetic force persists for greater tip-to-sample separations than the Van der Waals force. If the tip is close to the surface, in the region where standard non-contact AFM is operated, the image will be predominantly topographic. As the separation between the tip and the sample is increased, magnetic effects become apparent. Collecting a series of images at different tip heights is one way to separate magnetic from topographic effects. Nevertheless, the image interpretation is limited by the usually complex nature of the interaction between the sensing probe and the sample. In particular the magnetic state of the tip may not be well defined and may be perturbed by the stray field of the sample under investigation thus providing a non-uniform response. This poblem is particularly encountered using soft magnetic tips.

The tip-sample interaction in MFM may be viewed either as (i) the interaction between the tip magnetization and sample stray field or (ii) the interaction between the

sample magnetization and tip stray field. Therefore although MFM is thought to provide a picture of the sample stray field interacting with the tip magnetization, the images may be thought as essentially a convolution between the tip stray field and the sample magnetization. If the tip stray field is known, the reconstruction of the sample magnetization is then a deconvolution process from the information in the image. Studying the stray field from the tip, therefore provides extremely usefulness information regarding the imaging properties of a tip. Electron holography has demonstrated its usefulness for imaging the stray field distribution of MFM tips. A detailed description of this topic is presented in chapter 4.

1.5 Comparison of domain imaging techniques

The limits of domain observation techniques are divided in three areas: in spatial resolution, in the recording time and in the information depth of the method. High quality preparation of the surface to be analyzed is assumed in the consideration of this last characteristic, while the recording time limits the dynamic capabilities of the methods. In figure 1.10 a comparison of the different domain observation techniques is represented.

1.6 Why electron holography?

As a conclusion of this introductory chapter, we point out the advantages of the electron holography technique.

1. Electron Holography allows for an intuitive interpretation of the collected results because the magnetic lines of force appear as contour fringes in the reconstructed phase map.

2. Magnetic structures can be related to structural features of the specimen: electron holograms are in-focus images, whereas Lorentz micrographs are strongly defocused images. As shown in figure 1.11, the difference between an image recorded by either Lorentz microcopy or electron holography demonstrates that the latter

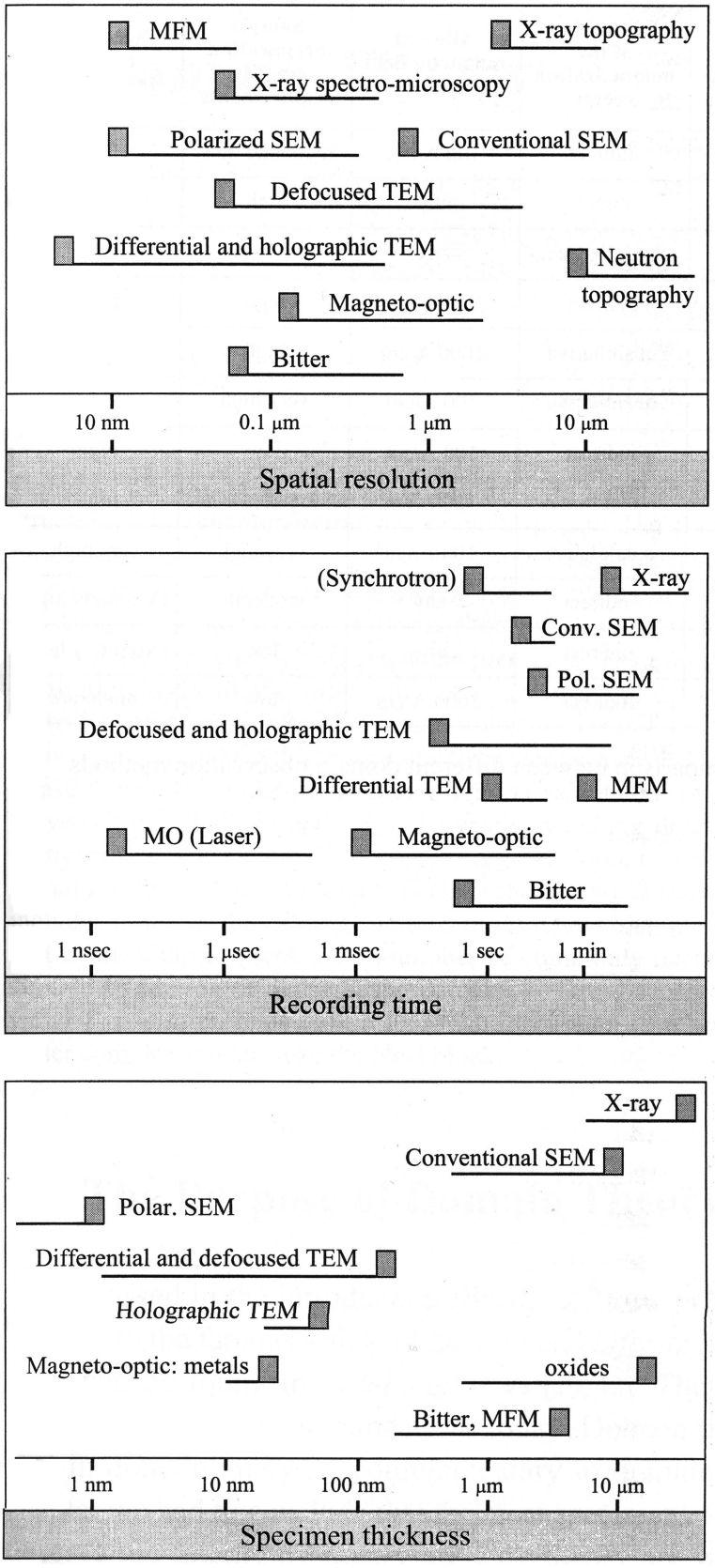

Figure 1.10: Comparison of different techniques employed to observe magnetic domains (after [53]).

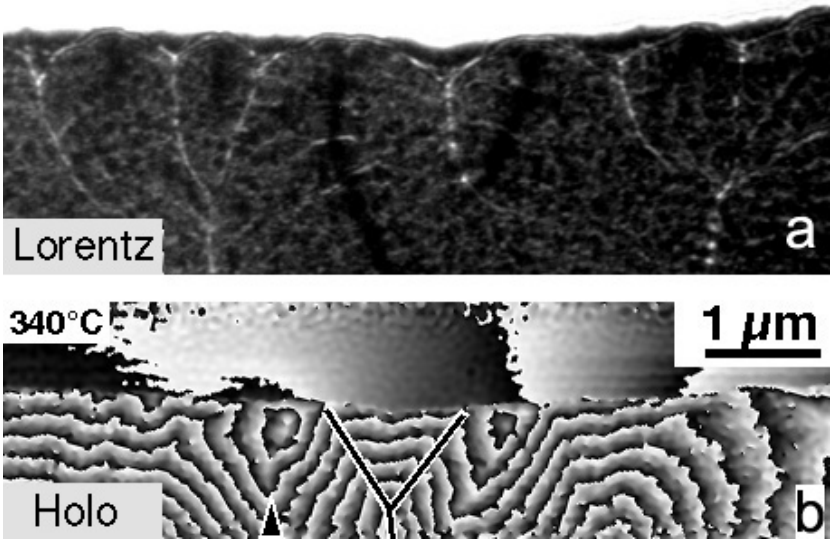

Figure 1.11: Images of a thin nickel film which have been obtained by (a) Lorentz microscopy and (b) electron holography. The dark and bright lines in (a) indicate domain walls. In (b) a y-shaped domain wall configuration is marked by lines.

provides information about the magnetic configuration of the sample, inside and outside.

3. The magnetic state is not perturbed by the measurement because, as mentioned before, the objective lens of the microscope is switched off and the sample is in a field-free space.

4. Quantitative measurements are also possible. A flux of h/e = 4.1 $\cdot 10^{-15}$ Wb corresponds to a 2π phase difference between two adjacent contour fringes.

Unfortunately, also the electron holography technique presents some limitations. For example the flux sensitivity is limited to about $2\pi/50$ to $2\pi/30$, i.e. 2 to 3% of the ratio h/e. Another limit is related to the spatial resolution of the Lorentz lens, that is about 2 nm. A further constraint is the signal to noise ratio (S/N ratio), which is rather low because the specimen is supported on an amorphous thin film. Therefore, recorded holograms are characterized by a considerable background noise.

1.7 A short introduction to our microscope

This paragraph summarizes the main features of the electron microscope that has been extensively used for this research work, a TECNAI F30 from FEI Company. This is an advanced transmission electron microscope with a field emission gun electron source (FEG, a Schottky-type field emitter with an energy spread < 0.8 eVs) and equipped with a super twin lens system. The accelerating voltages range from 50 to 300 kV.

The microscope can reach magnifications up to 250.000 times, and it is capable of a point-to-point resolution higher than 2 Å(the information limit is about 1.2 Å). The spherical aberration C_S, caused by the lens field acting inhomogeneously on the off-axis rays, is about 1.1 mm. The chromatic aberration C_C is about 1.4 mm.

The microscope, apart from the conventional camera, is equipped with a slow-scan charge coupled device camera (CCD) for the recording of digital images. This is a 1k x 1k camera, with 24 μm pixel size. Attached to the CCD camera is a Gatan imaging filter (GIF, a spectroscopic device produced by Gatan Inc.). The GIF is used as an additional lens system and offers 2k x 2k images, where the pixel size is 30 μm.

The microscope combine high-resolution imaging with analytical tools such as electron diffraction or X-ray microanalysis. An energy dispersive spectroscopic device (EDS) is attached to the microscope allowing for the detection of all elements down to and including beryllium. The resolution of the EDS is 136 eV or better, measured at MnKα, and the take-off angle is 20°.

EELS (electron energy loss spectroscopy) is another technique used for the analysis of samples. This technique allows for the selection of the electrons that finally form the image and most importantly, filter out those electrons that do not contribute to the image information. The capability to use electrons with specific energy losses for the image formation provides structural or element specific contrasts that can provide new insight and better information. The resulting two-dimensional compositional maps can have nanometer-scale resolution.

2 Nanocrystalline Fe particles: thermal evolution of the magnetization

2.1 Introduction

The most simple representatives of nanostructured systems with 3-small dimensions are the single-phase nanocrystalline materials, which essentially are polycrystalline solids with grains of nanometric dimensions. Typically, the mean grain size is of the order of 10 nm. Figure 2.1 shows a simulated atomic structure of a nanocrystalline material. Due to the reduced grain dimensions, the number of atoms located at the interfaces between the crystallites can be a relevant fraction (up to some tens of %) of the total number of atoms [61].

The main feature of nanostructured magnetic systems, strongly affecting their macroscopic behavior, is the similarity between the characteristic structural and magnetic lengths. Perhaps the most fundamental of the magnetic length scales is the exchange correlation length L_0. This is expressed as $L_0 = (A/K)^{1/2}$, where A is the exchange stiffness parameter and K the magnetic anisotropy coefficient. L_0 represents the scale within which the magnetic moments are forced to align parallel by exchange interaction and provides a measure of the domain wall width. It follows that particles with sizes smaller than L_0 cannot have a multidomain structure. L_0 takes the following values: 23 nm for Fe, 5.5 nm for Co and 51 nm for Ni.

For ferromagnetic material, it can be assumed that the atomic magnetic moments are aligned parallel, by exchange interaction, along directions which are determined by

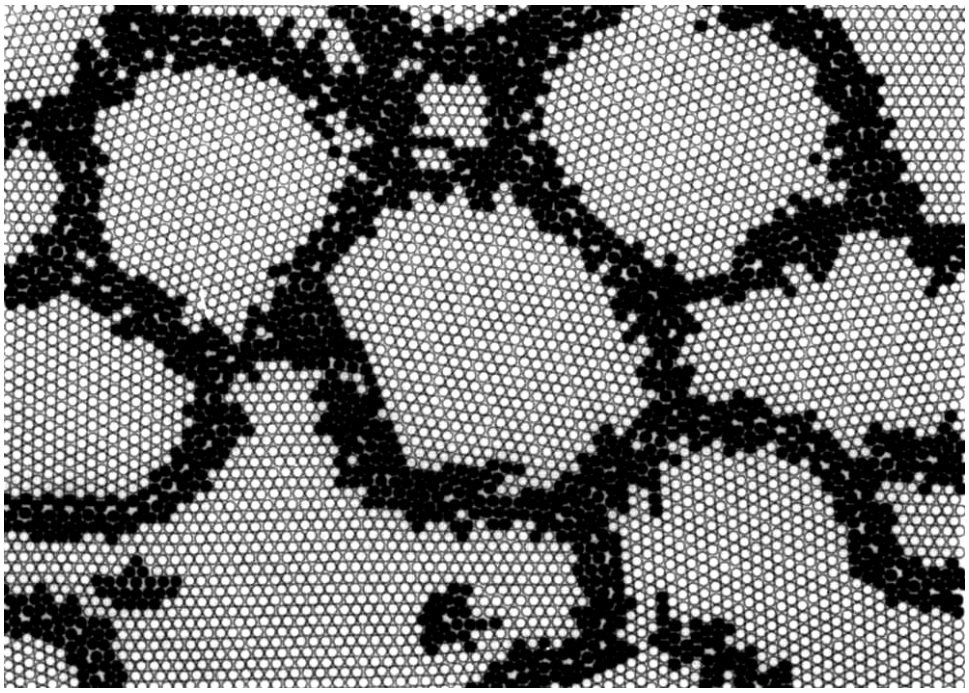

Figure 2.1: Atomic arrangement of a nanostructured material simulated by computational calculation. The empty dots represent the atoms in the crystallites and the dark dots the atoms in the grain boundaries (after [60]).

the magnetocrystalline anisotropy. In a nanocrystalline material, the anisotropy easy axis changes on a length scale corresponding to the mean grain size and hence comparable to L_0. Therefore, the resulting magnetic behavior stems from the competition between magnetic anisotropy and exchange interaction. Herzer proposed a mathematical description of such effects, the Random Anisotropy Model (RAM) [62], to which we also refer in the discussion of our experimental results. A brief description of the RAM is presented in the appendix.

In light of the above considerations, some peculiarities of the magnetic behavior of nanostructured systems have been accounted for. For instance, the magnetic properties of ferromagnetic systems, constituted by single-phase nanocrystallites embedded in a matrix, may vary from soft to hard as the effective value of the magnetic anisotropy depends on the interplay between structural parameters (mean grain size and intercrystallite distance) and the exchange correlation lengths of both phases [62, 63]. A further example is the low-temperature magnetic behavior of nanocrystalline Fe, which exhibits a transition

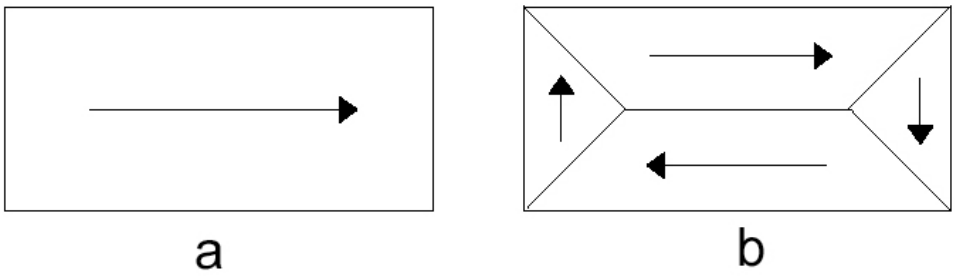

Figure 2.2: Domain formation in a large rectangular magnet. The black arrows indicate the direction of the magnetization each domain [60].

from a ferromagnetic regime to a spin-glass-like state [64]. This effect has been associated with temperature driven changes in the relationship between the above parameters, with the only difference that the embedding matrix is replaced by the grain boundaries among the crystallites. Accordingly, it is expected that the magnetic domain configuration of nanostructured magnetic materials and its thermal evolution are also affected by the particular structural features.

It is useful to recall briefly the factors involved in domain formation [65]. The magnetic domain configuration in a bulk magnetic material is the result of the minimization of different energy terms including the anisotropy energy, the exchange energy and the magnetostatic or stray field energy. The effect of each of these can be illustrated using a large rectangular magnet magnetized along its easy axis. In figure 2.2a, the exchange energy and the anisotropy energy are both zero. However, the magnetostatic energy (the energy due to the field produced by the magnet) is maximized since the magnet acts like a single, giant dipole. In order to minimize the total energy, two parallel domains and two closure domains will form, as shown in figure 2.2b. This increases the anisotropy and exchange energies due to the transition regions between the domains, but significantly reduces the magnetostatic energy. Therefore, as this example shows, although the formation of domains is driven by the magnetostatic energy, the actual domain configuration is determined by the total anisotropy energy and the competition between the exchange and anisotropy energies during domain wall formation.

The sample geometry is crucial in the determination of the most suitable technique for imaging magnetic domains (this topic was discussed in chapter 1). At present, a large

number of results are available on the domain patterns in thin films or at the surface of thicker samples (laminated samples, ribbons, disks - see [53] for a complete review).

In the case of nanocrystalline soft-magnetic ribbons, information on the domain pattern was gained using magneto-optic Kerr microscopy [66]. The general appearance of the domain pattern was found to resemble those of metallic glasses - characterized by very large domains and wide domain walls - as a consequence of the exchange coupling among the nanocrystallites, which dominates the anisotropy of single crystallite.

In our work, electron holography has been employed to image the stray field leaking out of micrometric Fe particles with ultrafine grain structure, in the range of nanometers. The particles have been prepared by mechanical attrition through ball-milling and suffer from a high degree of structural metastability. This is generally encountered in this class of samples because of the far-from-equilibrium synthesis technique (see paragraph 2.2.1). The remarkable point regarding the use of electron holography for the study of these samples is that it allows for the direct observation of the stray field emerging from an individual, isolated particle, regardless of its irregular shape, in a wide temperature range (300–1200 K) and without inducing any magnetic perturbation.

In our case, the micrometric Fe particles are not transparent to electrons and hence electron holography is unable to provide direct evidence on the magnetization distribution inside the particles. Note that this would be virtually impossible for most of the presently available domain imaging techniques. However, useful information on the interior domain pattern has been inferred from analyzing, both qualitatively and quantitatively, the leakage field and especially its modifications with temperature using complementary X-ray diffraction and electron microscopy analyses.

This research project has been done in close collaboration with the group of Prof. E. Bonetti (University of Bologna), which also provided the samples, and for electron holography in collaboration with Dr. G. Matteucci (University of Bologna). The electron holography work has been carried out at the Center for Interdepartmental Electron Microscopy (CIME) of EPFL in Lausanne. Therefore we gratefully acknowledge Prof. P. Stadelmann for his continuous support.

2.2 Experimental

2.2.1 Mechanical attrition technique

In the last decade, the mechanical attrition technique by ball milling has been widely used for the production of various metastable structures including amorphous materials, solid solutions of immiscible elements, and nanostructured materials [67]. Regarding this last class of systems, it is now well established that the crucial parameters for the resulting physical properties are the mean grain size, the presence of a relevant volume fraction of grain boundaries and also their thermodynamic state [68]. As a non equilibrium processing technique, mechanical attrition can produce systems with different degrees of metastability, provided that some synthesis parameters are well controlled [67, 69]. During the milling process, reticular defects are produced, "pumping" energy into the crystalline powder with diameters ranging from 10 to 50 μm and grain dimensions of the order of the micron. The internal refinement process, with a reduction of the mean grain size by a factor of $10^3 - 10^4$, results from the creation and reorganization of dislocations with formation of small angle grain boundaries, and subsequently, high angle grain boundaries.

The samples that were studied in this project were prepared by means of this technique, using a planetary ball mill. The experimental apparatus used for the synthesis of these samples was a horizontal planetary mill, with original features, different from systems that are normally used (a schematic drawing is displayed in figure 2.3).

The planetary motion of two vial holders is generated by an external electrical motor and transmitted to the internal rotating tree by two transmission chains and a mechanical joint. The vials, made of hardened steel, are cylindrical with an internal volume of about 50 cm^3 and a rounded bottom to guarantee a homogeneous deposition of the powder; the vials are closed by a cover with a central hole, to allow for dynamical vacuum conditions during milling. The balls for the mechanical milling are also made of hardened steel; the diameter is 0.8 cm and the weight is 2.1 g. The optimal ball to powder weight ratio is in the range 8:1$\rightarrow$ 20:1.

The performance of the machine includes:

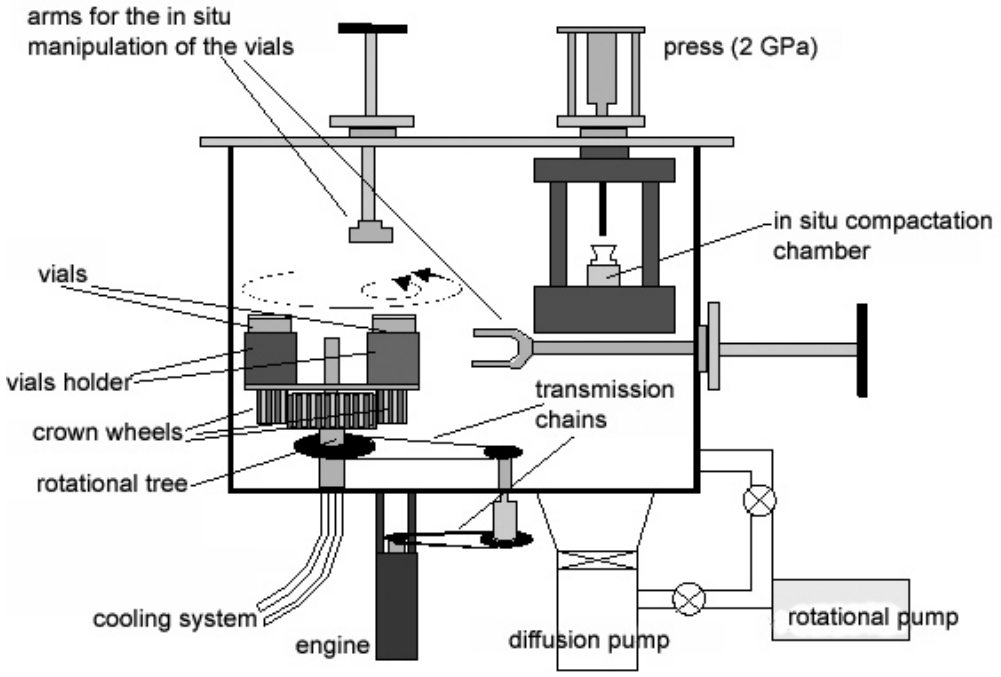

Figure 2.3: Schematic representation of the planetary mill used to prepare the nanocrystalline Fe powders.

1. The possibility to operate at controlled atmosphere.
   The milling chamber is connected to a vacuum system (rotation pump, diffusion pump and liquid nitrogen trap) that allow to perform the mechanical synthesis under dynamical high vacuum conditions (10^{-5} Pa), and hence to control the oxidation process (of free surfaces).

2. The possibility to operate at low temperature.
   The apparatus is connected to a cooling system that allows the flow of liquid nitrogen through the central body of the mill; therefore, it is possible to realize the mechanical attrition in a wide temperature range (150-300 K). At low temperature the brittleness of the material increases, thus enhancing the efficiency of the collisions between spheres and powders; under such conditions, welding effects of the powders to the vial's walls are avoided.

3. The possibility of *in situ* manipulation of the as-milled powders.
   Two manipulating handler arms, inserted in the milling chamber through two linked vacuum joints, allow to lift and shift the vials, thus to transfer the powder into

a stamp/mould for compaction. The *in situ* manipulation of the milled powders allows the production of *bulk* samples, reducing their oxidation .

2.2.2 Synthesis of the sample and characterization techniques

The nanocrystalline Fe powders to be investigated were obtained by ball-milling 99.9% pure Fe powders (Alfa Products) for 60 hours in a vacuum of 10^{-4} Pa at a temperature of 220 K. The ball-to-powder weight ratio was 10:1

X-ray diffraction (XRD) was carried out with a Philips PW 1710 vertical powder diffractometer employing Ni-filtered Cu-Kα radiation and a graphite monochromator in the diffracted beam. The volume-weighted average grain size D and the root-mean-square microstrain $< \varepsilon >^{1/2}$ were evaluated by the Warren-Averbach method [70] via a convoluted profile fitting procedure [71]. The thermal evolution of D and $< \varepsilon >^{1/2}$ was determined by performing XRD both on powders as-milled and annealed in a furnace for 30 min in a flowing-Ar atmosphere at several selected temperatures $T \leq 770$ K (we did not reach higher temperatures because at that stage the grains of the particles were already in a stable configuration; secondly that temperature was also near the maximum temperature reachable with the furnace in use).

Transmission electron microscopy and off-axis electron holography observations were made on Fe particles dispersed in ethanol and transferred onto a thin amorphous carbon film, which was supported by a standard Cu grid. Electron holograms were recorded with a Hitachi HF-2000 FEG electron microscope operated at 200 kV and equipped with a slow scan charge coupled device camera. The electron holograms were obtained under isothermal conditions in the temperature range from 300 to 1200 K. The temperature changes were induced at a typical rate of 20 K/min and the acquisition of the hologram was preceded by 30 min thermal equilibration at the set point temperature (we assume that the *in situ* and the furnace annealing procedures induce a similar evolution of the microstructure). Images and phase maps were reconstructed with the software Holo Works 1.0 plug-in of Digital Micrograph 2.5 by Gatan Inc [72].

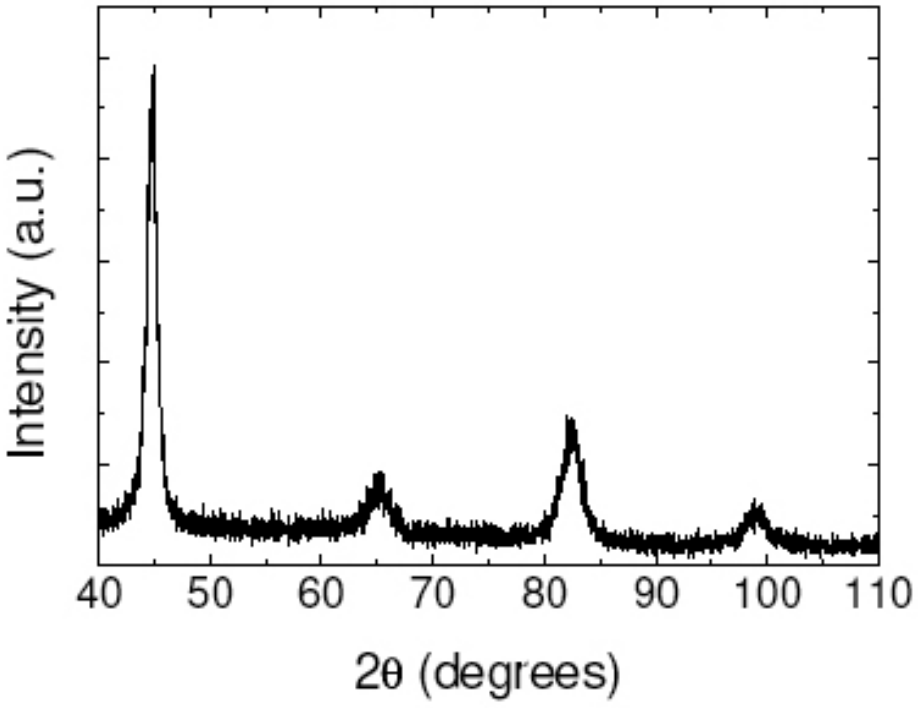

Figure 2.4: X-ray diffraction spectrum, using Cu-Kα radiation, of as-milled nanocrystalline Fe powders.

Conventional TEM observations using X-ray microanalysis (EDS) and high resolution imaging were also made on a Philips CM30 TEM operated at 300 kV. The point-to-point resolution of this TEM corresponds to 0.2 nm. These analysis were carried out both on as-milled particles and on particles after being subjected to *in situ* heating procedures during the electron holography analysis.

2.3 Results

2.3.1 Structural characterization

The XRD spectrum of as-milled Fe powders is displayed in figure 2.4. The peaks relative to bcc iron are well visible whereas no Fe oxide phase can be detected. The Warren-Averbach analysis of the (110)-(220) reflections yields a volume weighted average grain size D = (12 $\pm$ 2) nm and a root mean square microstrain $<\varepsilon>^{1/2} = (4.5 \pm 0.5) \times 10^{-3}$.

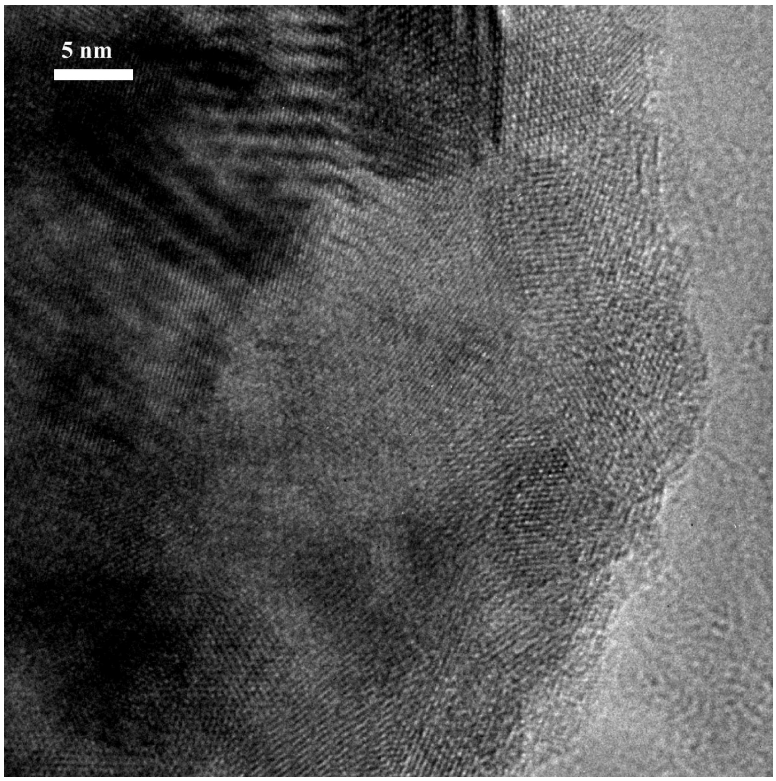

Figure 2.5: High-resolution TEM image of the thin border of an as-milled Fe particle.

If we look at the typical high-resolution TEM image of an as-milled Fe particle, shown in figure 2.5, we observe lattice and Moiré fringes, due to the different grain orientations. In good agreement with XRD, the estimated grain size is approximately 10 nm. It can be seen that the grains have random orientations relative to each other, as expected for the last stages of milling [67]. The EDS analysis in the transmission electron microscope indicates that in the as-milled powders, the amount of oxygen and other metallic impurities is below the detection threshold ($\sim$ 0.1 at. %), in agreement with previous results on similar samples [73]. No change in the oxidation level can be observed upon annealing. Figure 2.5 also suggests that the oxide is present only as a very thin ($\sim$ 1 nm) amorphous layer on the particle surface (no lattice fringes with large spacings corresponding to magnetite and hematite can be observed).

The evolution of D and $< \varepsilon >^{1/2}$ with the annealing temperature is depicted in figure 2.6. The mean grain size is approximately constant up to 620 K, whereas a marked reduction ($\sim$ 70%) of the internal lattice strain is experienced. At higher temperatures, a

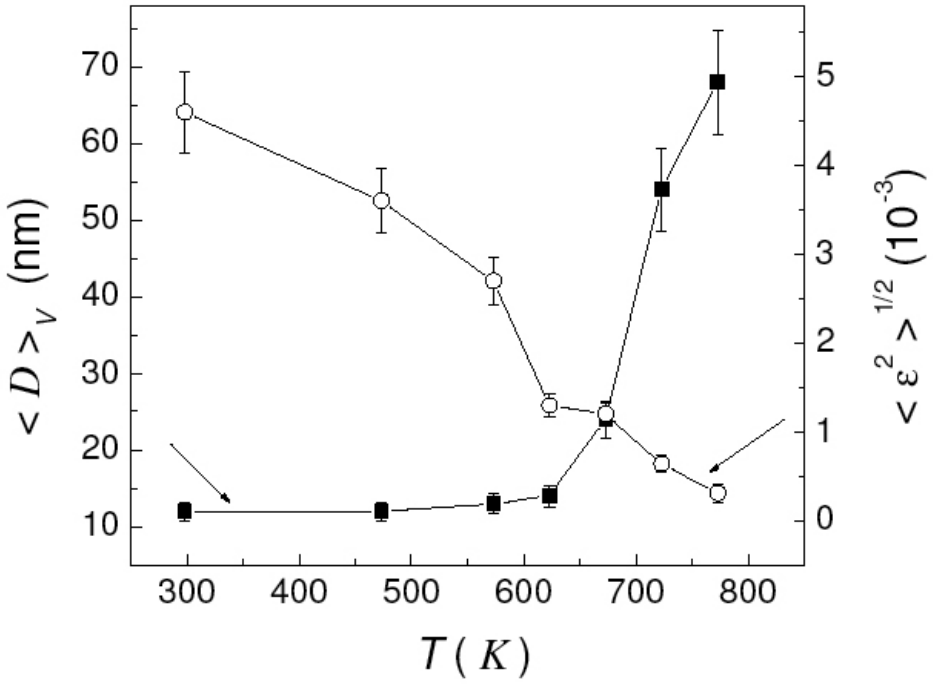

Figure 2.6: Evolution of the average grain size D and of the microstrain $< \varepsilon >^{1/2}$ with the annealing temperature, as estimated by X-ray diffraction.

strong grain growth occurs. Unfortunately, the analysis of the XRD spectra of samples annealed at higher temperatures does not provide reliable estimates of the grain size because the width of Bragg peaks is close to the instrumental resolution. However, TEM observations performed on particles annealed at 970 K, indicate that the grain size D is of the order of 500 nm, in agreement with the values reported by other authors [74, 75].

2.3.2 Electron holography analysis

Typical contour maps recorded at room temperature on isolated as-milled Fe particles are shown in figure 2.7. The black central region representing the projected TEM image of the particle has been superposed for the sake of clarity (note that the TEM image was taken at the end of the holography analysis in order to avoid any exposure of the particle to the magnetic field of the objective lens of the microscope). On the outside of the particle, alternating black and white lines are clearly visible. As explained in paragraph 1.2, such

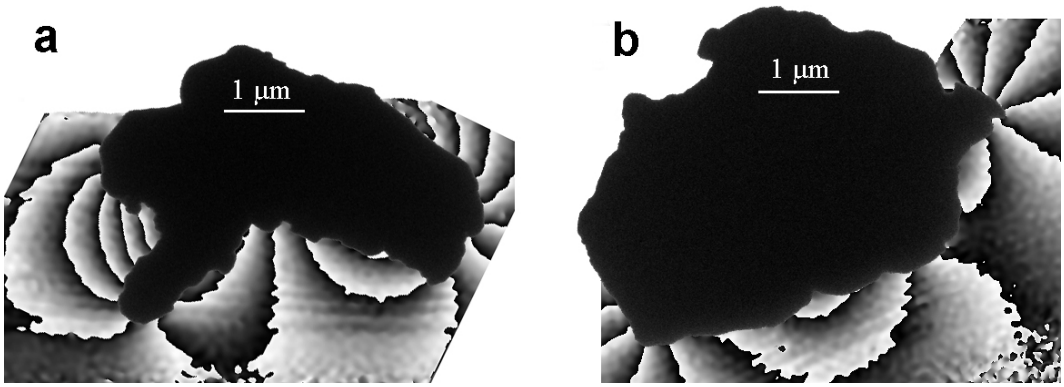

Figure 2.7: Phase maps of as-milled Fe particles, recorded at 300 K.

fringes can be interpreted as magnetic flux lines which emerge from the free magnetic poles in the particles [65].

The results of the electron holography analysis as a function of temperature are exemplified by the sequence of images in figure 2.8. In each contour map the phase has been amplified four times, i.e., the phase maps are represented modulo $2\pi/4$. A large number of lines fans out from the particles at T = 300 K (figure 2.8a). Their number does not change substantially by increasing the temperature up to 570 K (figure 2.8b) whereas it is clearly reduced in figure 2.8c, recorded at 770 K. No further strong modifications are observed in the stray field intensity by increasing the temperature up to 970 K (figure 2.8d). After cooling down the sample to 300 K, the number of flux lines practically does not change (figure 2.8e). Figure 2.8f is an example of a contour map recorded above the Curie temperature, where no flux lines are visible.

Therefore, the first evidence is that, as a consequence of the thermal treatment, a strong reduction in the number of flux lines spreading out from the particle at 300 K is experienced. It is also noteworthy that the positions of the magnetic poles from which the flux lines emerge are practically unchanged in the five patterns.

Both the above remarks were found to be generally valid for all the examined particles; another significant example is shown in figure 2.9. Here the phase maps are represented modulo 2π. In this case, the analyzed particle (see inset in figure 2.9a) is larger than the one, shown in figure 2.8, and therefore the dark region on each pattern only represents the image of the lower portion of the particle. The flux lines are seen to leak out

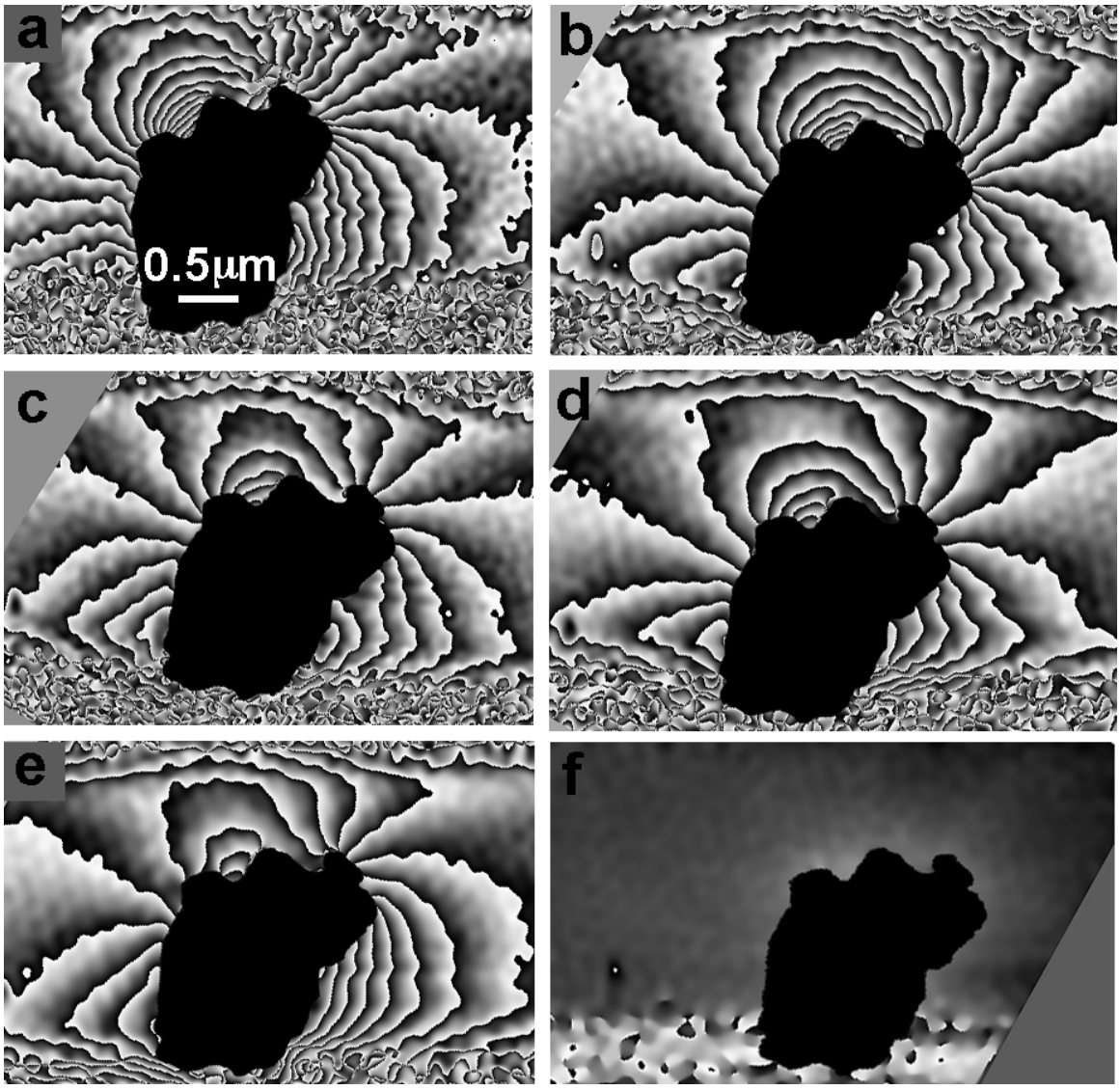

Figure 2.8: Phase maps of a ball-milled Fe particle recorded at the following temperatures: a) 300 K (as-milled state), b) 570 K, c) 770 K, d) 970 K, e) 300 K, after cooling from 970 K, and finally f) at 1170 K, above the Curie temperature.

of a magnetic pole localized in the lower part of the particle. In this case, the stray field intensity decreases progressively passing from room temperature (figure 2.9a) to 770 K (figure 2.9b) and 970 K (figure 2.9c), as revealed by the reduced number of contour fringes which fan out of the particle. After lowering the temperature down to 300 K (figure 2.9d), the field intensity is even further reduced. However, the positions of the magnetic poles from which the flux lines emerge remain practically unchanged.

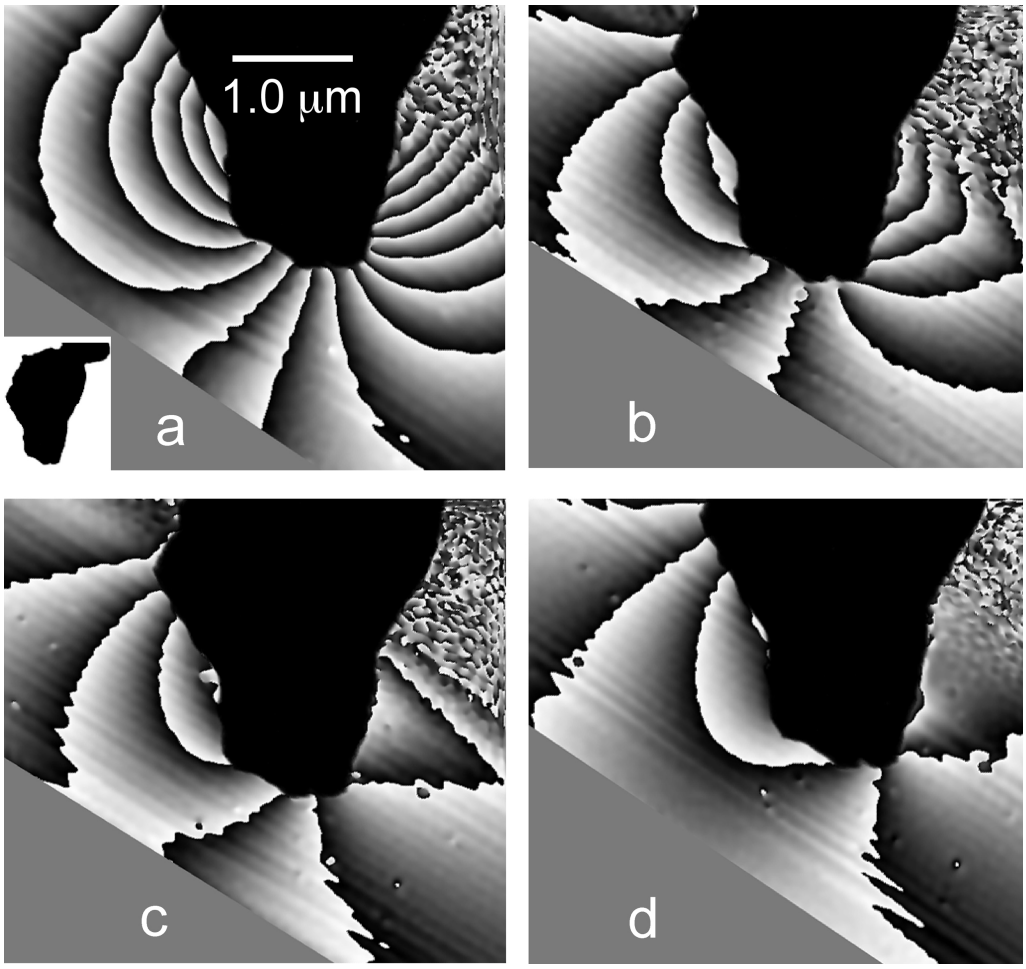

Figure 2.9: Phase maps of a ball-milled Fe particle, shown in the inset, recorded at: a) 300 K (as-prepared state); b) 770 K; c) 970 K; and d) 300 K, after cooling from 970 K.

Further indications on the localization of the magnetic poles have been gained by performing observations on the two particles shown in figures 2.10 and 2.11. After having recorded the hologram of the as-milled particle in figure 2.10a, the objective lens was switched on, which implied that a magnetic field H of the order of 20 kOe was applied perpendicular to the plane of the sample grid. After about 60 seconds, the lens was switched off and a new hologram was taken; the reconstruction (figure 2.10b) clearly indicates that the magnetic poles stayed at the same locations.

The images in figure 2.11 of an as-milled Fe particle were taken at (a) room temperature, (b) at 1170 K, (c) and 300 K after cooling. Apart from the reduction in the number of flux lines upon annealing, again one observes that free magnetic poles form in the same

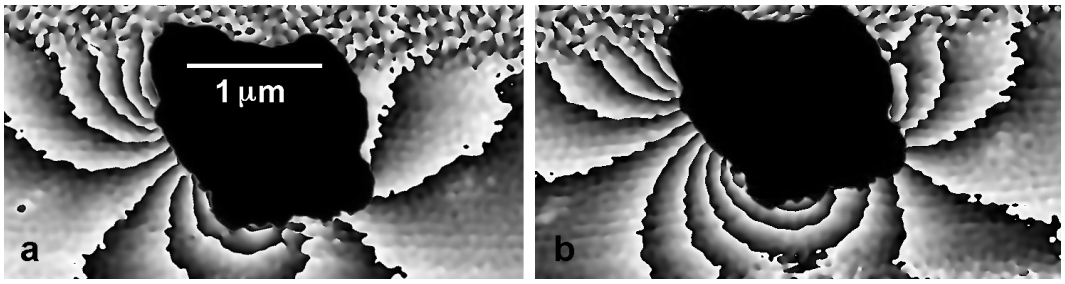

Figure 2.10: (a) Phase maps of an as-milled Fe particle, recorded at 300 K; (b) the same particle, after application of a 20 kOe field, perpendicular to the figure plane, for 60 s.

positions before and after annealing. It should be considered that in this case the temperature was raised to well above the Curie temperature of Fe, which explains the absence of magnetic flux lines in figure 2.11b, corresponding to a demagnetizing treatment (the single fringe that appears around the particle is due to the fact that the particle is slightly electrically charged by the electron beam, because of the very thin oxide film present on the grain).

2.3.3 Discussion

In order to provide an explanation for the electron holography results, some preliminary considerations are needed.

In the case of soft magnetic materials with very small magnetic anisotropy, a sample much larger than L_0 will contain a true domain pattern in most of its volume, such as to avoid the formation of free magnetic poles and therefore the formation of a stray field. On the contrary, in a sample smaller than or comparable to L_0, a classical domain configuration with formation of domain walls is not possible. In this situation, the presence of free magnetic poles may be avoided by the formation of an anomalous magnetization pattern presenting typical flowing structures, particularly near unfavorably oriented surfaces [53]. In this kind of configuration the magnetostatic energy decreases at the expenses of the exchange energy, and a reduction of the stray field may be achieved, especially as long as the sample presents a regular geometric shape.

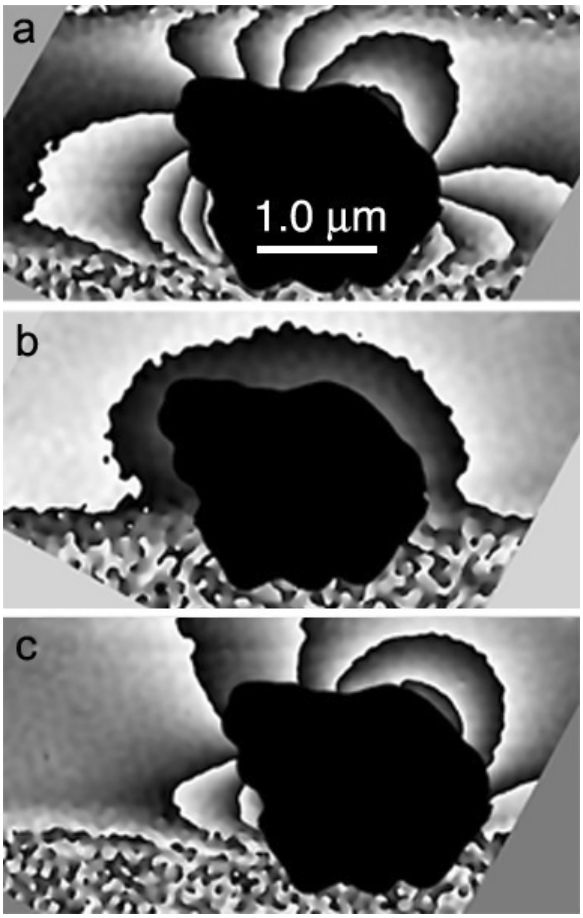

Figure 2.11: Phase maps of a ball-milled Fe particle recorded at: (a) 300 K (as-prepared state); (b) 1170 K; and (c) 300 K, after cooling from 1170 K. The equipotential in (b) indicates an electrostatic field due to weak charging of the particle.

In regard to the samples analyzed here, further considerations are necessary for the discussion. The mean crystallite size D in the as-milled Fe particles is ~ 12 nm, whereas the exchange correlation length of coarse-grained polycrystalline Fe is approximately 23 nm [76]. According to the random anisotropy model (RAM) for exchange-coupled nanocrystalline magnetic systems [62] (see also appendix), the condition $D < L_0$ implies that a reduced value of K, compared to coarse-grained Fe, results from averaging over all the grains that are contained in the volume of the exchange correlation length. As a consequence of the decrease in K, the scale on which the exchange interaction dominates expands. Therefore the exchange correlation length is rescaled and is given by the expression $L^* = 16A^2/9K^2D^3$ [62, 77]. Taking $A = 10^{-11}$ J/m and $K = 10^4$ J/m^3 it can be calculated that L^* is much larger than the natural L_0, of the order of a micron. Moreover,

it has to be considered that D increases irreversibly owing to the thermal treatment (figure 2.6). In fact, TEM observations show that after annealing at 970 K, the crystallite size increases to value as high as 500 nm, much larger than $L_0(300K) \backsimeq 23$ nm; i.e., the condition $D < L_0$ is no longer fulfilled. As a consequence, with respect to as-milled Fe, an irreversible increase in K and a decrease in the exchange correlation length towards its natural value L_0 are induced in the annealed sample.

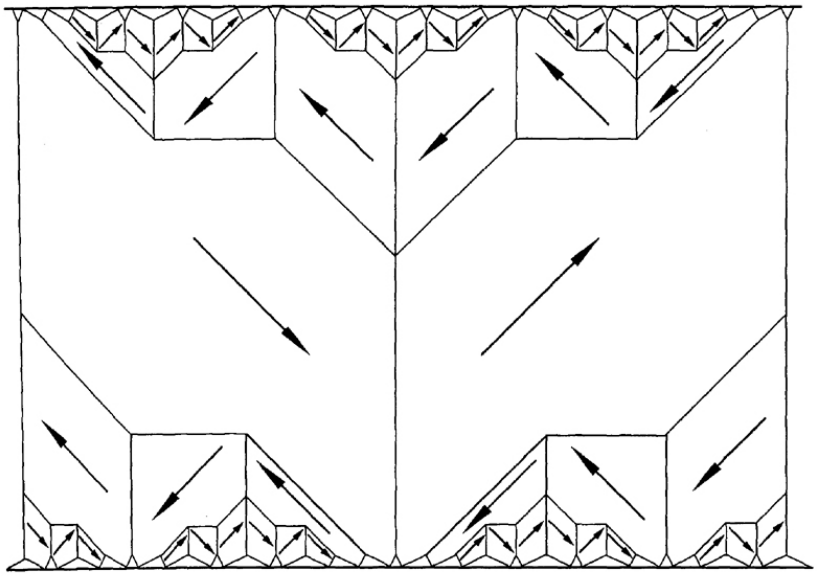

Figure 2.12: Principle of the domain branching encountered in large crystals with strongly misoriented surfaces. Close to the surface a fine domain pattern is enforced to minimize the closure energy. The branching process connects the wide and the narrow domains in a way that depends on the crystal symmetry and in particular on the number of available easy directions [78].

On account of the above discussion, large extended magnetic domains with wide walls should be expected in the as-milled particles, in agreement with previous investigations on Fe-based nanocrystalline ribbons [66]. However, we are confronted with the very special case of individual particles whose size is comparable to L^*. Therefore, it can be argued that a true domain pattern with canonical domain walls is not really present and that the stray field reduction occurs, mainly at the expenses of exchange energy, by means of inhomogeneous magnetization structures. On the contrary, in the annealed particles (figures 2.8e, 2.9d, 2.11c), L_0 is much smaller than the particle dimension and therefore

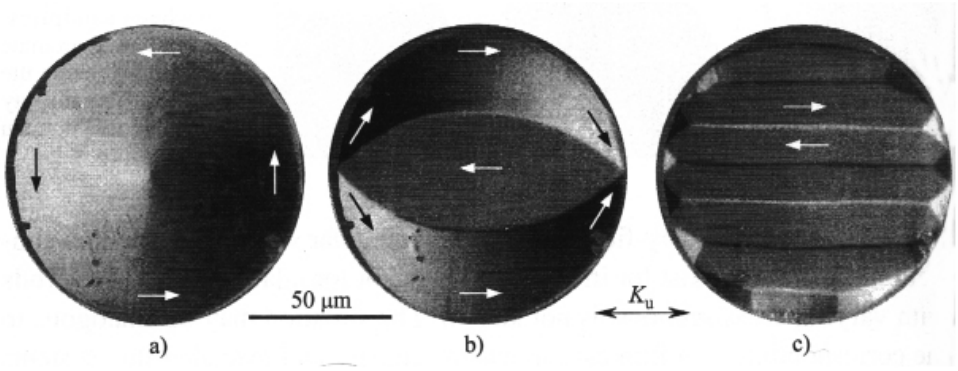

Figure 2.13: A disk-shaped thin film iron-permalloy multilayer system displays an isotropic magnetization pattern (a). A compressive stress introduces anisotropy (b, c). The images were taken with magneto-optical Kerr effect [80].

the presence of several magnetic domains is expected to be possible. It must be taken into account that the investigated particles present a very irregular shape and probably strongly misoriented surfaces, with respect to the direction of the easy axis of magnetization. In this situation, the formation of a fine domain pattern analogous to the domain branching phenomenon observed close to the surface in large cubic crystals may be enforced [53]. The principle can be seen in figure 2.12 [53, 79].

A phenomenon similar to the one we are hypothesizing was found to occur by Hubert in a disk of permalloy [80]. As shown in figure 2.13, as a consequence of the increase in the anisotropy of the system, induced by the application of an externally applied stress (magnetoelastic anisotropy), the magnetic configuration of the system completely changes from freely flowing magnetic domains (2.13a) to a well defined multidomain structure (2.13c).

The electron holography analysis clearly indicates that the magnetic configuration in as-milled particles is highly metastable. Both in as-milled and the annealed state, a flux leakage is observed. However, due to annealing, a more stable configuration is achieved that is more effective in closing the stray field, as clearly indicated by the reduction in the number of flux lines observed at 300 K after the *in situ* thermal treatments (figures 2.8e, 2.9d and 2.9c). Our hypothesis is that this magnetic instability is strictly connected to the structural instability of the as-prepared particles. In particular, the increase of the mean grain size D in annealed compared to as-milled samples is the parameter discriminating

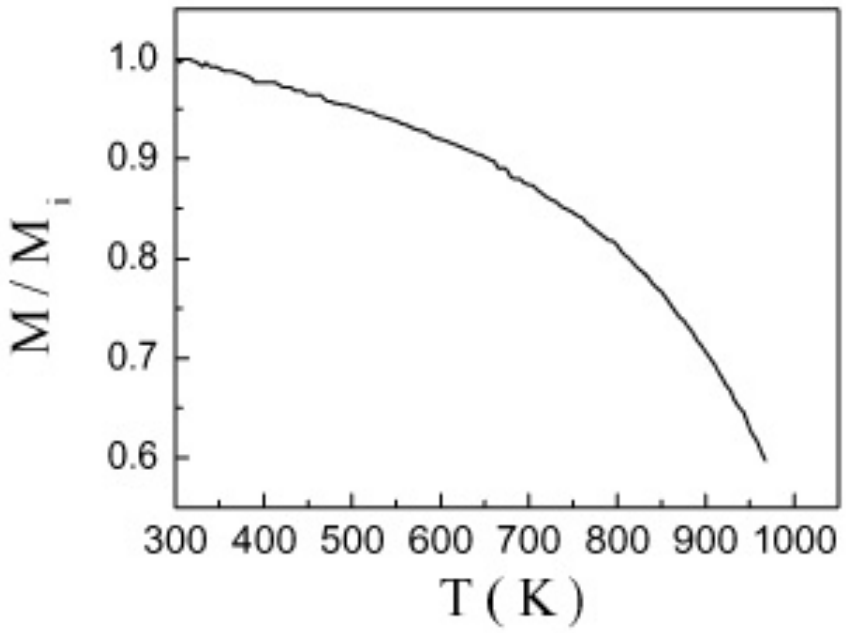

Figure 2.14: Magnetization (M) as a function of temperature (applied field H = 10 kOe) of un-milled Fe powder. M_i is the room temperature magnetization value.

between the domain configurations outlined above, since it directly implies a variation of the exchange correlation length.

The analysis of the contour maps recorded at high temperature deserves further attention. In particular, the reversible decrease of the saturation magnetization M_s and the increase of the exchange correlation length with increasing temperature must also be taken into account. This last effect is due to the more rapid decrease of $K \propto {M_s}^{10}$ compared to $A \propto {M_s}^2$ with increasing temperature (in bcc Fe). As a reference curve for the variation of M_s with temperature, we consider a measurement on un-milled Fe powder (figure 2.14; M_i is the magnetization value at 300 K) carried out using a LDJ 9500 Vibrating Sample Magnetometer under an applied field H = 10 kOe, sufficient to induce an almost complete saturation. Indeed, by raising the temperature up to 570 K, the main variation in the sample microstructure, revealed by XRD, is shown by the microstrain reduction (figure 2.6), whereas the change in M_s becomes relevant at higher temperature (figure 2.14). However, nearly no changes are observed passing from figure 2.8a to figure 2.8b which suggests that internal stresses – which are supposed to be mainly localized at the grain boundaries [81] – do not affect strongly the domain configuration. This seems to indicate

that the magnetoelastic anisotropy does not contribute substantially to the total anisotropy, as expected also on account of the low saturation magnetostriction of polycrystalline Fe ($\lambda_s = -7 \times 10^{-6}$, [65]). Therefore, it may be neglected, as we did when applying the RAM.

A simple calculation indicates that at 770 K the natural L_0 increases up to ~ 50 nm and reaches ~ 150 nm at 970 K. At these temperatures, D grows up to ~ 70 nm and ~ 500 nm, respectively. A straightforward application of the RAM would lead to the conclusion that the value of the exchange correlation length to be considered in these cases is the natural one since no re-scaling occurs. Obviously, this is a simplified assumption if one considers for instance that, at those temperatures, a time dependence of the mean grain size as well as of the grain size distribution takes place.

With reference to the images in figure 2.8, the decrease in the leakage field intensity observed on passing from 300 K to 770 K (Figs. 2.8a, 2.8c) may therefore be attributed to a rearrangement of the magnetic domain configuration resulting in a more effective closure of the flux inside the particle, but could be also connected with the decrease of the saturation magnetization. Surprisingly, this last effect seems to have no consequence on the stray field intensity, on passing from 770 K to 970 K (figure 2.8d), namely to a temperature very close to the Curie point of Fe (1043 K). This indicates that, in spite of the very similar flux line pattern, a quite different domain configuration should be present at 970 K allowing for a rather intense stray field to emerge. This supports the hypothesis according to which, in these particles, a larger value of the exchange correlation length generally implies a less efficient closure of the stray field. The same argument may explain why, in spite of M_s(970 K)/ M_s(300 K) ≈ 0.6, the stray field intensity after cooling to 300 K (figure 2.8e) is very similar to that observed at 970 K (figure 2.8d). In fact, we can assume with certainty that the exchange correlation length at 970 K is larger than the value of ~ 23 nm expected at 300 K. A further significant support to this point comes from the evolution of the flux line pattern found in many other particles further strengthens this argument, as exemplified by the images in figure 2.9 which show that the stray field at 970 K (figure 2.9c) is even stronger than after cooling down to 300 K (figure 2.9d). Indeed, a slightly different thermal evolution has been observed in the particle of figure 2.9 compared to figure 2.8, but this is not surprising since many parameters compete in determining the resulting leakage field (M_s, L_0, D, grain size distribution and the particle geometrical shape, as discussed below). For instance, for the particle in figure 2.9, the

reduction in the number of contour fringes on passing from 300 K (figure 2.9a) to 770 K (figure 2.9b) is stronger than for the particle in figure 2.8, and cannot be entirely accounted for the limited decrease in M_S. Therefore, a strong change in the domain pattern must also be assumed.

Despite the observed changes in the stray field intensity upon annealing, the positions of the magnetic poles from which the flux lines spread out are not seen to vary. In fact we have observed that free magnetic poles form in the same positions both after the application of a strong magnetic field (figure 2.10) - which was expected to change dramatically the domain pattern, saturating the particle - and after performing a demagnetizing procedure by annealing above the Curie temperature (figure 2.11). These observations are indicative of the influence of the overall geometrical features of the particles in determining the arrangement of the magnetic poles. Tips or concavities along the particle surface constitute a geometrical constraint favoring the formation of magnetic poles in preferential locations.

2.3.4 Conclusions

In this chapter we have presented the results of the electron holography analysis of the magnetic thermal evolution of ball-milled nanocrystalline Fe particles. In particular, we have analyzed qualitatively the changes in the stray field emerging from the particles as a function of temperature, from 300 K to above the Curie temperature. The results have been discussed based on the structural characterization data, obtained by XRD and high-resolution TEM. A direct relationship between the stray field variation with temperature and the structural evolution has been established and indirect information on the interior magnetization pattern have been derived. The decrease in the stray field observed at 300 K after annealing the nanocrystalline Fe particles at 970 K is suggestive of a significant modification of the magnetization pattern connected with grain growth. In the framework of the RAM, we have suggested that the as-milled particles are characterized by flowing magnetization patterns due to an enhanced value L^* of the exchange correlation length, similar to the particle size. On the contrary, in the annealed particles, the large D/L_0 ratio allows for the formation of classical magnetic domains. The electron holography analysis allows to conclude that the domain configuration settled in the annealed particles is more effective in reducing the stray field.

The overall evolution of the stray field with increasing temperature confirms the leading role played by the exchange correlation length in determining the actual magnetic domain configuration. In particular, the leakage field intensity at 970 K, similar or, for some particles, even higher than observed after cooling to room temperature, confirms that the thermally induced enhancement of L_0 at 970 K results in a less effective closure of the stray field.

Finally, it is pointed out that for these particles the overall geometrical features play a major role in establishing the lowest energy magnetization pattern. In this respect, we have directly verified that in a single particle the magnetic free poles tend to form in preferential locations close to shape irregularities, regardless of the thermal and magnetic history of the particle itself.

3 Gas-phase condensed Fe nanoparticles: magnetic and structural properties

3.1 Introduction

The study of magnetic properties of fine particles was traditionally driven by both a technological and theoretical interest, connected with the possibility to develop a better understanding of magnetic phenomena related to size effects. In recent times, new methods of synthesis (inert gas condensation, layer deposition, ultrarapid quenching, chemical sol-gel method) have been set up allowing a quite good control of the particles size in the nanometer range. That has been also the occasion for a renewed interest in the field of magnetism of ultrafine particles, which has invariably led to the discovering of unexpected magnetic behavior strictly depending on the reduced dimensional regime [82].

The macroscopic behavior of nanostructured magnetic systems is determined by the structure, size and morphology of the constituent phases and by the type and strength of magnetic coupling between them. For an assembly of non-interacting particles, the magnetic properties mainly depend on their volume: for instance, single-domain particles can show superparamagnetic behavior when their thermal energy is comparable to the anisotropy energy barrier for moment reversal, a quantity which is proportional to the particle volume [83, 84]. Inter-particle interactions (dipole-dipole or exchange interactions) compete with the anisotropy energy in determining the orientation of the particle moments. If strong enough, these interactions may turn the collection of individual superparamagnetic relaxation processes into a collective dynamical behavior [85–87].

Inter-particle interactions also dominate the magnetic properties of bulk nanostructured materials. Examples of systems with excellent hard [88] or soft [89] magnetic properties or with giant magnetoresistive response [90–92], generally constituted by nanoparticles embedded in a (magnetically and/or structurally) different matrix. In this case, the magnetic interactions are transmitted through the matrix, which therefore determines the magnetic behavior. It was recently demonstrated that even ultrafine ferrite particles [93–95] as well as ball-milled nanocrystalline Fe [64] can be considered as heterogeneous systems. Due to surface and interface effects, their magnetic properties are very different with respect to that of the bulk, coarse-grained counterparts. Broken bonds, lack of structural periodicity in the boundary regions and the presence of competing magnetic interactions may produce spin canting and spin-glass-like behavior.

Nowadays, the interest in ultrafine magnetic particles is still strongly motivated by the perspective of the possible technological applications. For instance, ferromagnetic particles with lateral dimensions of less than 100 nm have been proposed in applications as magnetic recording media. In particular, the arrays of submicron magnetic particles made by lithographic patterning [96], with a range of materials, geometries and dimensions, as well as the self-assembled particles systems, obtained by chemical route [97,98], are very promising candidates as ultra high density recording materials in which each magnetic element should store one bit of data. In this context, gaining a deeper insight into the magnetic microstructure of a single nanoparticle and into the magnetization reversal mechanism is the aim of many researchers [99].

Theoretical predictions have been reached by Monte Carlo simulations and computational micromagnetic modeling [100–102]. Wernsdorfer *et al*. [103] studied the static and dynamic magnetic behavior of a single Co nanoparticle, using a microscopic quantum interference device (SQUID) loop surrounding the particle itself.

A different experimental approach consists in performing average magnetic measurements on assemblies of many identical dots. The hysteresis loops of circular NiFeMo soft magnetic dots (500-55 nm diameter and 6-15 nm thickness), fabricated by high-resolution electron beam lithography, were measured by Cowburn *et al*. with a high-sensitivity magneto-optical method [104]. Ross *et al*. [105] measured the magnetic hysteresis and the remanent state of Co and Ni particles with truncated conical shapes and diameters of 80-120 nm, prepared by using interference lithography combined with an

evaporation and lift-off process; the results were compared with a 3-dimensional micromagnetic model.

Direct information on the magnetic configuration of thin magnetic dots has been obtained by MFM. In particular, Shinjo *et al*. [106], provide the first experimental evidence of a magnetic vortex state with a turned-up magnetization core in circular Permalloy dots 0.3 to 1 μm in diameter and 50 nm thick (see picture 3.1). Nucleation and annihilation of vortex states have been studied in two-dimensional arrays of densely packed Co dots by MFM and magneto-optical Kerr effect (MOKE) together with numerical simulations [107]. A similar investigation was carried out by Fernandez *et al*. [108] on arrays of polycrystalline Co structures fabricated by interference lithography.
The influence of the mutual interaction on the magnetic properties of an ensemble of ultraflat Co particles produced by molecular beam epitaxy (MBE), has been studied by Stamm *et al*. [109] using scanning Kerr effect microscopy (SKEM) and SEMPA analysis.

Despite the strong interest, very few experimental results [110] exist for 3-dimensional particles probably because demagnetized particles are still inaccessible for most of the presently available domain imaging techniques (see chapter 1).

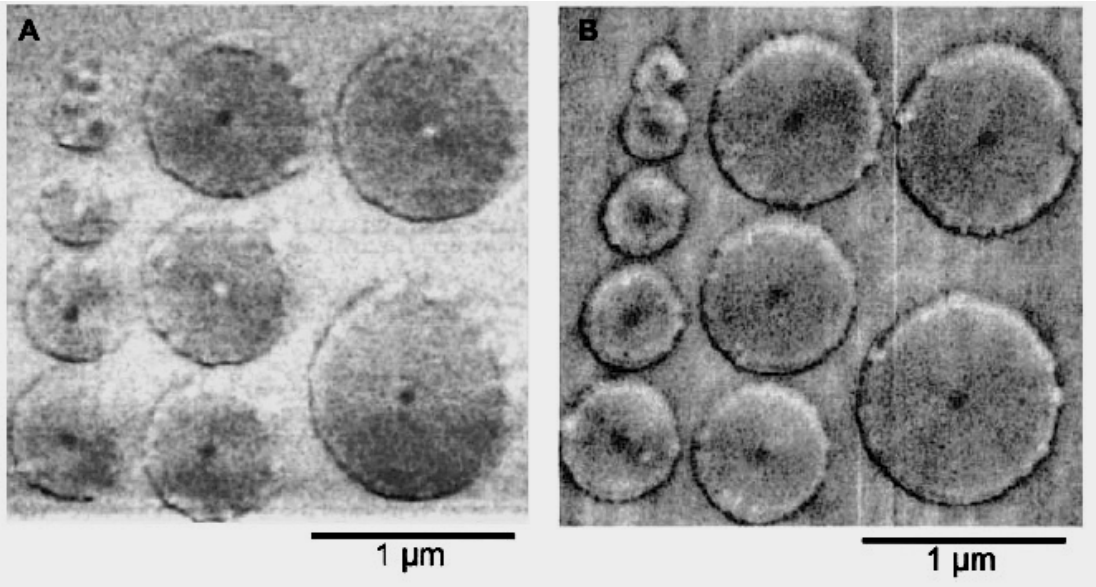

Figure 3.1: Image of an ensemble of 50-nm-thick permalloy dots with diameters varying from 0.1 to 1 μm after applying an external field of 1.5 T along the in-plane direction (A) and perpendicular to the plane (B). Image from Shinjo *et al*. [106].

In view of this situation, we have carried out electron holography investigations on Fe nanoparticles with a mean size of $\sim$ 50 nm, produced by the Inert Gas Condensation (IGC) method. Before exposure to air, the particles were oxygen passivated in order to prevent self ignition. Some general details about the IGC technique and about the apparatus used in our case are given in paragraph 3.2.1.

Recently transmission electron holography technique has been usefully employed for studying different nanostructured system. Matteucci *et al*. [111] used electron holography to monitor directly the magnetization configuration in a thin Permalloy film when the temperature was gradually raised towards the Curie point. The same authors also employed the technique for the direct observation of magnetic flux lines in a thin Ni film when the temperature was slightly changed near the Curie point [112]. Beeli *et al*. applied electron holography to image the magnetic flux leaking out of ferromagnetic Co and Ni wires of radii ranging from 20 to 150 nm and a length of a few microns [113]; the study aimed to gain information on the remanent magnetization state and also on the magnetization reversal of an individual nanowire [114]. Snoeck *et al*. characterized, using off-axis electron holography, the magnetic remanent state of 4-nm-diameter single-crystalline Co nanowires, isolated or arranged in bundles [115]. The magnetization reversal behavior and the magnetic interaction effects of submicrometer-sized patterned Co elements was also studied using off-axis electron holography [116]: linear arrays of rectangular Co elements, of 30 nm nominal thickness, were prepared using standard electron beam lithography and lift-off processes (each element was 275 nm in width and between 220 and 800 nm in length). Transmission electron holography provided information on the magnetic properties of carbon-coated Co and Ni nanoparticles with sizes ranging from 25 to 90 nm [117]. In that case, the hologram spatial resolution was around 100 nm and the magnetization of the sample was derived from the phase change of the electron wave transmitted through the sample.

In our case, the aim was to explore the potential of the electron holography technique to study the magnetism of 3-dimensional Fe nanoparticles. Fe is very suitable for investigations by electron holography because it has the highest saturation induction (B_S = 2.15 T) among the pure elements. Accordingly, the phase shift measured through a single particle of several tens of nm in size, can vary from 0.5 π up to 6 π, which falls in the optimal range for electron holography measurements. A special aspect of our work is that electron holography observations were made in a high-resolution mode. The spatial

resolution is between 5 and 10 nm, thanks to the features of the TEM at our disposition (see paragraph 1.7).

Our work was part of a wide study in the framework of a Research Advanced Project (PRA) entitled "Electronic Transport in Magnetic Granular Systems" (ELTMAG), sponsored by the INFM-National Institute for the Physics of Matter (Italy) and involving five different research groups. In particular, we collaborated with the group of Prof. Bonetti (Bologna University), that also provided the samples, and, for the electron holography analysis, with Dr. G. Matteucci (Bologna University).

The study of the low temperature magnetic and magnetotransport properties of oxygen passivated Fe nanoparticles was also among the goals of the ELTMAG project. By cold-compacting the core-shell Fe particles, a granular system is built up, which is constituted by two different magnetic phases (the Fe crystallites and the surrounding Fe oxide matrix) modulated on a nanometer scale. The system is particularly suitable for investigations aimed to gain an insight into the leading role of magnetic interactions on the magnetic behaviour of nanostructured materials.
The compositional, structural and magnetic properties of the granular Fe/FeOxide system were studied by means of TEM, XRD and magnetization measurements.
The system was found to exhibit a peculiar low-temperature magnetic behaviour, dependent on the Fe particle mean size and on the Fe and oxide fractions and strongly determined by the exchange coupling between the metallic crystallites and the disordered (both structurally and magnetically) oxide phase.

Hence, in section 3.3, I will present a resume of the principal results obtained in this research work, in which I was also involved, and which therefore has been part of my PhD activity [118–121]. Indeed, some of the conclusions were obtained by the interpretation of the electron holography results, shown in section 3.4. Both the structural characterization data and the magnetic properties analysis have represented an important background of knowledge for the interpretation of the electron holography results.

3.2 Experimental

3.2.1 The Inert Gas Condensation technique

The inert gas condensation technique (IGC) is a well established method for the production of clusters or nanoparticles under controlled thermodynamic conditions [122]. Initially it was adopted to prepare dispersed nanoparticles, and only starting from about ten years ago, Gleiter suggested to use the same method to prepare bulk samples by in-situ consolidation of the gas-condensed ultrafine nanoparticles in vacuum [123].

The IGC apparatus we used for our research is shown schematically in figure 3.2. The main component is the evaporation chamber, separated from the compactation chamber and the load-lock chamber by two gate valves. The chambers can be evacuated down to $10^{-7} - 10^{-8}$ Torr by a turbomolecular pump. Once the desired vacuum is achieved, the evaporation chamber is isolated from the pumping system and filled with inert gas (Ar or He) at a pressure of typically between 1 and 10 Torr. The material to be evaporated is placed into a tungsten boat heated resistively with an alternate electrical current (max current 1000 A). The apparatus is equipped with two independent sources allowing for the simultaneous evaporation of two different materials.

The physical principle of the technique is simple. The evaporated atoms loose energy via collisions with the atoms or molecules of the inert gas and condensed into atom clusters in the highly supersaturated vicinity of the precursor source. The growth of the nucleated clusters occurs in a region close to the source by a successive accretion of atoms or molecules and by cluster-cluster coalescence (figure 3.3).

In order to maintain a small size, the particles must be removed rapidly from the region of high supersaturation and this is accomplished by the convective flow of the gas towards a rotating metallic cylinder (‘cold finger’ in the scheme) cooled by liquid nitrogen. The cooling of the cylinder enhances the collection efficiency of the particles by favoring their extraction from the gas through a thermophoresis process and by increasing the convection flow towards the cylinder. Then, the nanoparticles are removed from the cylinder using a metallic scraper and are collected in a cup. Finally, they can be transferred into the compaction chamber for consolidation.

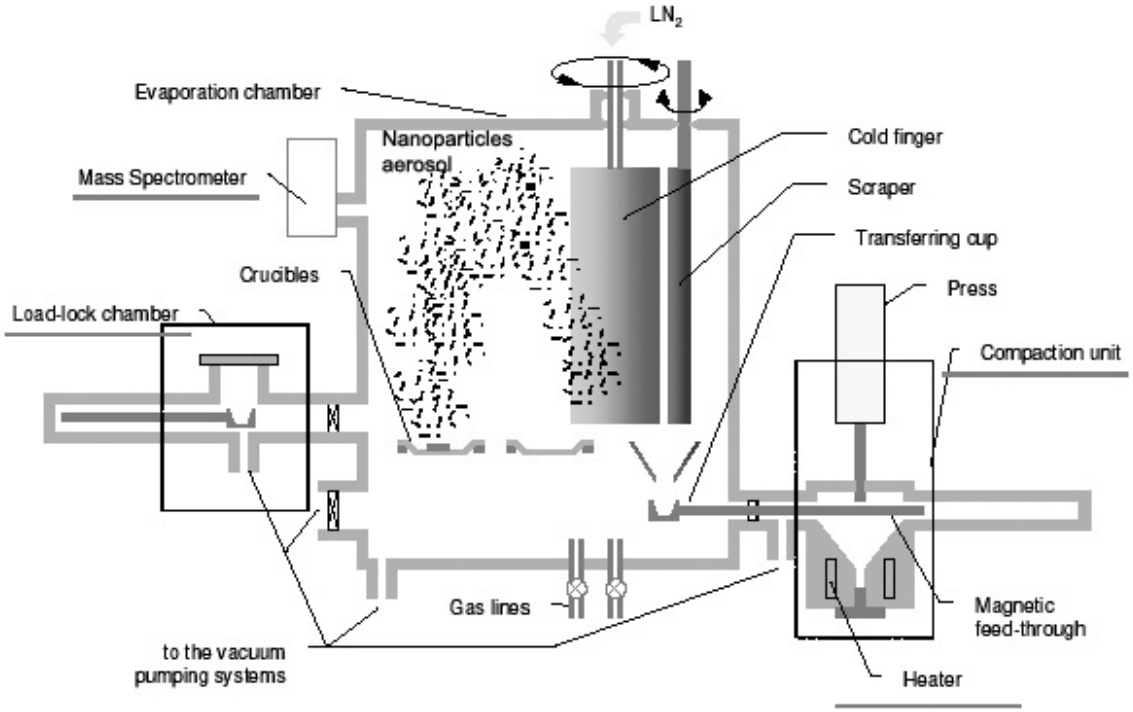

Figure 3.2: Schematic of the Inert Gas Condensation machine.

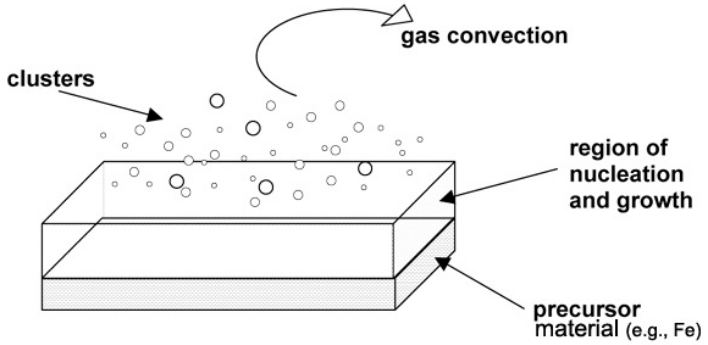

Figure 3.3: Schematic of the formation of nanoparticles by evaporation of a precursor material in inert atmosphere.

Experimentally, it has been observed that particles with a larger mean size are obtained when operating at a higher gas pressure or using a gas with higher atomic mass, i.e., Ar instead of He [124]. Hence, by varying the type and the gas pressure as well as

the source temperature, it is possible to control the final dimensions of the nanoparticles with good precision and versatility.

If further processing of the nanoparticles is needed to form the desired nanostructured system, for example an oxidation process to create an oxide ceramic or core-shell nanoparticles, this can be accomplished by introducing oxygen in the evaporation chamber either during or after the evaporation process.

3.2.2 Synthesis of samples and characterization techniques

The Fe nanoparticles were produced by the IGC method (starting from 99.98 % pure Fe), in He atmosphere at a pressure of 1 Torr. Subsequently, they were exposed to a mixture of 1 Torr O_2 and 9 Torr He for 12 hours to achieve passivation. Transmission electron microscopy (TEM) observations were performed on nanoparticles collected on a carbon-coated copper grid put inside the evaporation chamber during the synthesis process. We have employed a microscope from FEI/Philips Tecnai F30, installed in our laboratory, equipped with a Gif 2K x 2K CCD camera (see paragraph 1.7). Nanoparticles with increasing mean size have been obtained by increasing the heating current of the tungsten boat, and hence the vapour temperature, during three evaporation processes. After the passivation, the particles were scraped from the cold finger and pressed in high vacuum with a uniaxial pressure of 1.5 GPa, to obtain the pellets labeled D6, D10 and D15. The pellets were investigated by X-ray diffraction (XRD) using a Philips PW1710 diffractometer with $CuK\alpha$ radiation. Compacted pellets of powders were subsequently fragmented to obtain micrometric samples for magnetic characterization. Each micrometric fragment consisted of a dense agglomerate of nanoparticles.

Low temperature magnetic properties of the samples were investigated by means of a commercial SQUID magnetometer operating in the range between 5 and 300 K and equipped with a superconducting magnet (H_{max} = 55 kOe). A special software option allowed for a full control of the warming/cooling rates (e.g. 4 K/min, for the present experiments). The magnetic characterization measurement were carried out in collaboration with the group of Dr. D. Fiorani (Istituto di Struttura della Materia, CNR Roma).

3.3 Structural and magnetic characterization

3.3.1 Transmission electron microscopy

Figure 3.4a shows the TEM micrograph of a typical Fe particle obtained by IGC and oxygen passivation. The dark core corresponds to metallic iron whereas the surrounding light gray layer is the oxide phase. The thickness of such a layer is ~ 2 nm, independent of the Fe core size. The TEM contrast of the oxide phase resembles that of an amorphous structure and contains very small defective crystallites (figures 3.4a−d). The interface region between metallic core and oxide phase appears as a rather sharp boundary indicated by the strong Fresnel fringes, e.g. the dark contrast in figure 3.4b and c.

The TEM analysis reveals that the as-prepared particles are not always distinguishable as singular and well-separated entities, as shown in figure 3.4a. More generally, the products of the evaporation and passivation procedures are agglomerates of several nanoparticles. As shown in figure 3.4d, in the case of small Fe cores (mean diameter < 10 nm), the particles are well separated by the oxide layer even if small contact regions may exist. Larger metallic cores exhibit an enhanced tendency to merge together, forming welded neck junctions and grain boundaries (figure 3.4e). Moreover, it has generally been noted that the metallic cores have an elongated shape (figure 3.4f), a characteristic that is more pronounced with increasing the Fe core dimensions. We have found that very fine particles, with a mean size below 5 nm, are of spherical shape, as shown in figure 3.4g. Note that such particles do not show the characteristic core-shell morphology because they are so small that the passivation procedure induced their complete oxidation (each particle consists of several crystal grains). In agreement with previous studies [125], our findings indicate that during a synthesis process carried out at low vapour temperature, the growth of small spherical particles, similar to those shown in figure 3.4g, occurs by aggregation of atoms. At high vapour temperature, the coalescence of the primary particles seems to be particularly favored. Larger Fe cores are obtained whose symmetry departs more and more from a spherical one (figure 3.4h shows the detail of the incomplete coalescence of two metallic cores).

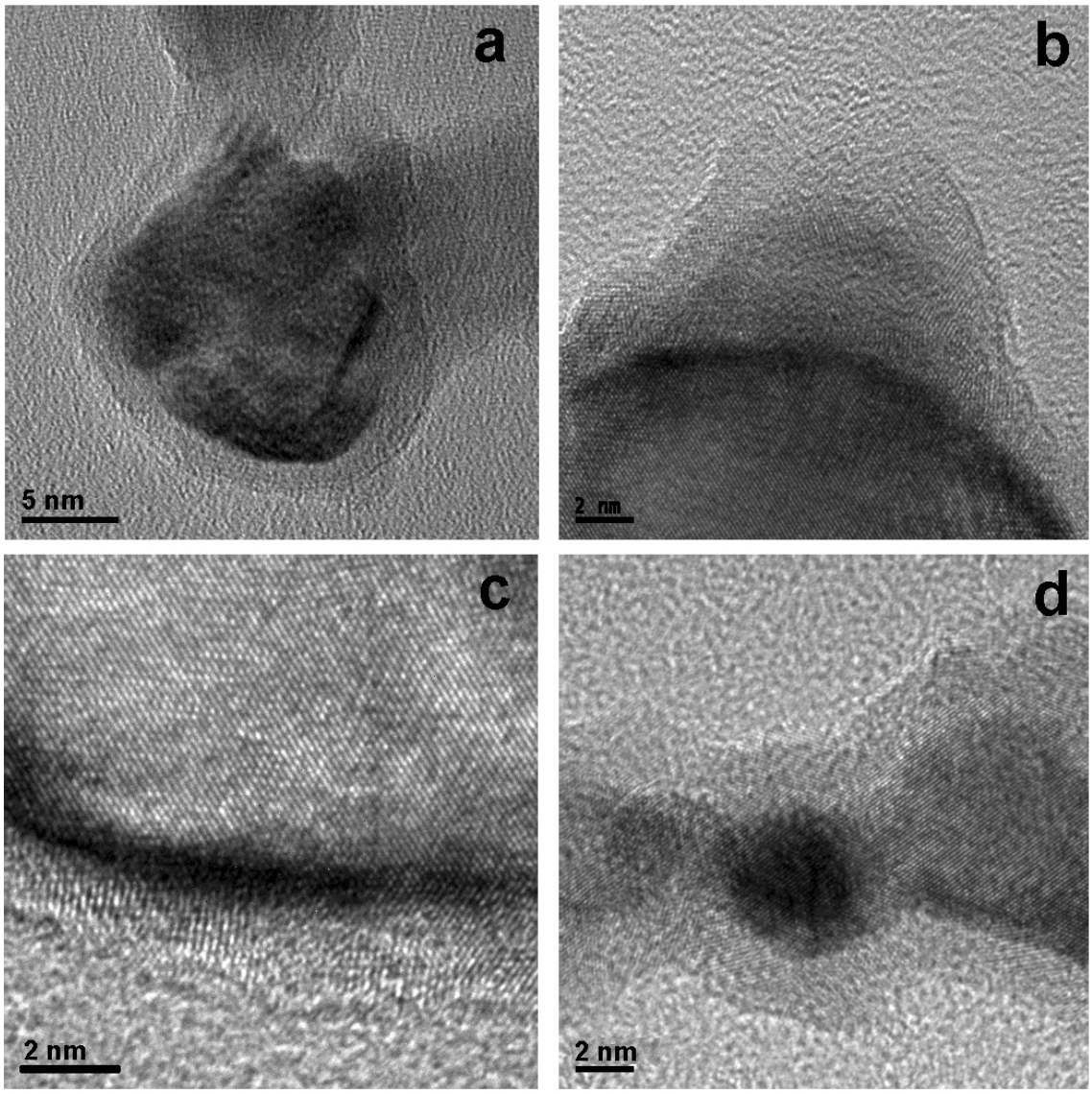

Figure 3.4: (Both pages) TEM micrographs of oxygen passivated Fe nanoparticles produced by IGC, supported on an amorphous carbon film. The particles in figures a−h present a core-shell structure. The dark core corresponds to metallic iron whereas the surroundings light gray layer is the oxide phase. Note that the very small particles in figure g do not have such a core-shell morphology. A detailed description of the images is given in paragraph 3.3.1.

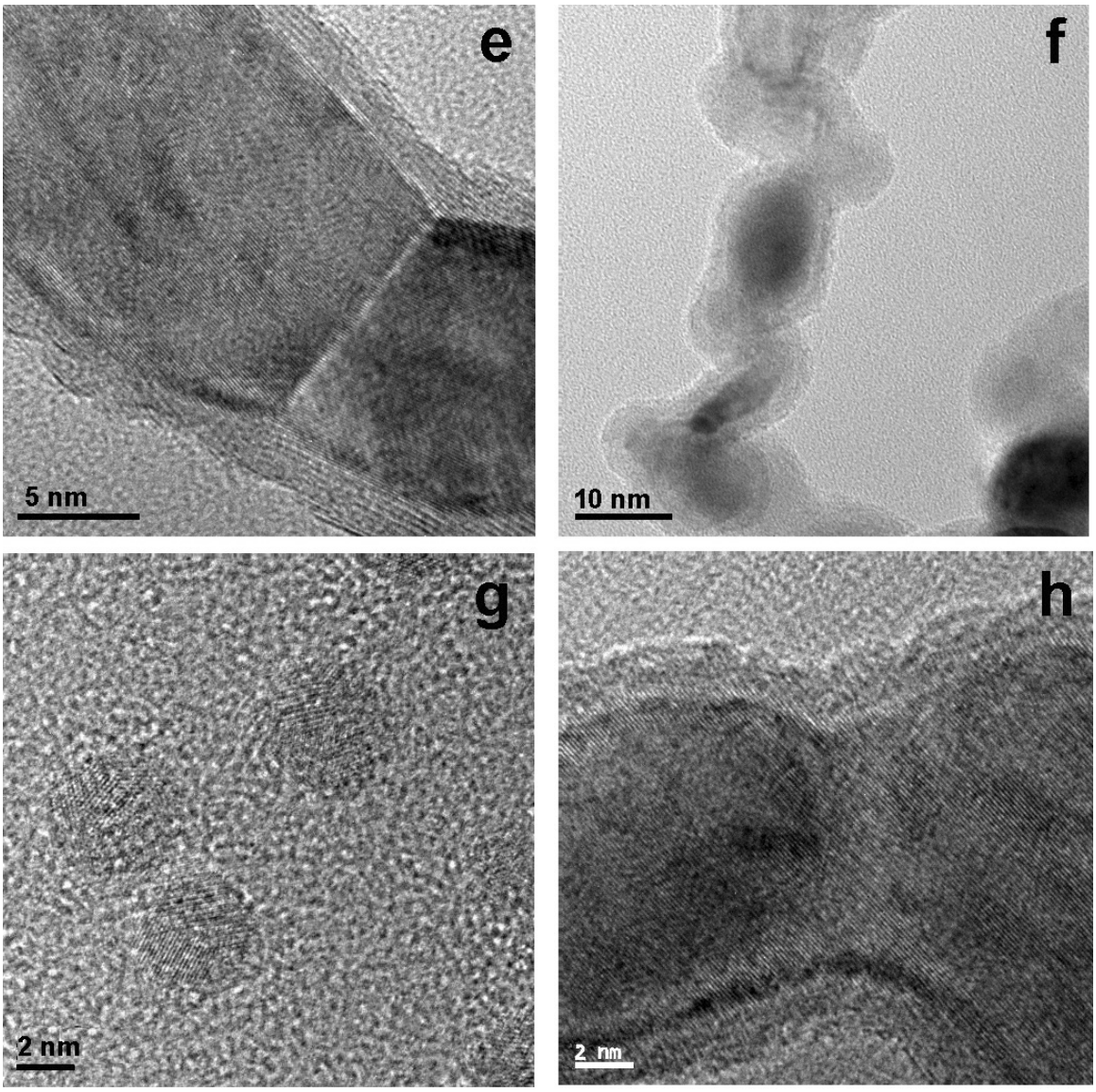
e
5 nm
f
10 nm
g
2 nm
h
2 nm

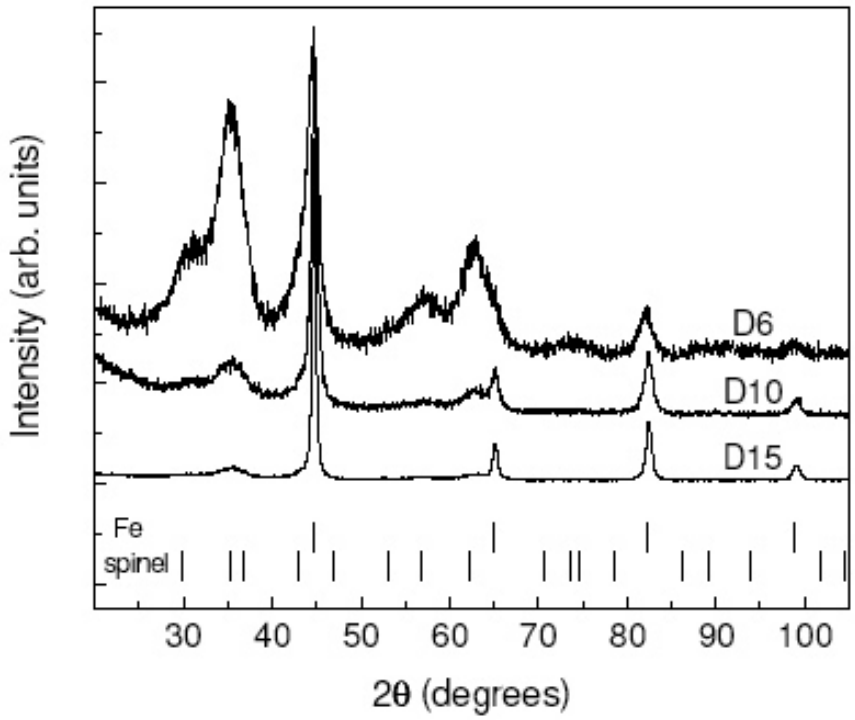

Figure 3.5: X-ray spectra for samples D6, D10 and D15 (using Cu-Kα radiation).

3.3.2 X-Ray Diffraction

The XRD spectra of the samples D6, D10 and D15 are shown in figure 3.5. Two components are detected: the broad peaks of bcc Fe and the broadened and thus overlapping peaks of the oxide phase. The position and the integrated intensity of the latter correspond to the values usually quoted for magnetite (Fe_3O_4) and maghemite (γ-Fe_2O_3), both adopting a spinel structure. However, the peak broadening does not allow us to distinguish between them. No reflection different from those of the cubic spinel structure were observed.

The XRD patterns were analyzed using a full profile-fitting program [126] following the Rietveld method [127] and assuming a spinel structure for the oxide phase. In particular, the refinement of the peak profile parameters and the quantitative phase analysis of the program were used to determine the volume averaged grain size (D), the microstrain ($< \varepsilon^2 >^{1/2}$) of the iron and oxide phases and their volume (and weight) fractions. This

type of analysis was carried out on a series of more than 20 samples including D6, D10 and D15 [124].

For both phases the intensity and width of the peaks are consistent with an isotropic model for crystallite size and strain. The results obtained for the Fe component are summarized in table 3.1.

Table 3.1: Results of the Rietveld analysis on the XRD spectra in figure 3.5. D and $<\varepsilon^2>^{1/2}$ are the volume averaged size and the microstrain of the Fe phase, respectively. The iron fraction (the volume Vol_{Fe} and the weight W_{Fe}) and the oxide fraction (the weight W_{Ox}) are also reported.

Sample	D (nm) ($\pm$ 10 %)	$<\varepsilon^2>^{1/2}$ (10^{-3}) ($\pm$ 10 %)	Vol_{Fe} (%) ($\pm$ 3)	W_{Fe} (%) ($\pm$ 3)	W_{Ox} (%) ($\pm$ 3)
D6	5.6	14	13	18	82
D10	9.6	9	21	28	72
D15	15.2	3	48	59	41

The Fe fraction increases with increasing *D*. Due to the particular morphology of the compacted nanoparticles, namely the characteristic core-shell structure evidenced by TEM (figure 3.4), we take the volume averaged grain size *D* to be a measure of the mean size of the Fe cores. In the series of 20 samples, the observed trend of the iron volume fraction vs. *D* was also in agreement with the assumption of spherical core-shell particles with a shell thickness of $\sim$ 2.5 nm, independent on the particle size, distributed according to a log-normal distribution with width $\log\sigma$ = 0.46. This last value was determined from the analysis of the XRD data as described in [124] and in agreement with those typically reported for a size distribution of gas-evaporated nanoparticles [122].

For the oxide lattice parameter, the Rietveld analysis provides an intermediate value between those of magnetite and maghemite (8.399 to 8.335 Å). We cannot exclude that the oxide phase is a mixture of both Fe_3O_4 and $\gamma - Fe_2O_3$, as suggested in previous work on similar samples [128, 129]. The average grain size of the oxide phase is $\sim$ 2 nm and the microstrain is of the order of 10^{-2}, one order of magnitude larger than for the metallic phase, consistent with high structural disorder. The very small grain size and the high

value of microstrain suggest that the oxide is a defective spinel due to high structural and topological disorder. A cation disorder, i.e., a non zero occupation factor of the octahedral c sites of the spinel structure and a reduction of the occupation factor for the usually occupied octahedral d sites, has been assumed to account for the (small) increase in the integrated intensity of the (440) peak, with respect to polycrystalline magnetite or maghemite.

3.3.3 Magnetic properties

Results

Magnetization vs. Field measurements

Hysteresis loops were measured on samples D6, D10, D15 at different temperatures T between 5 and 300 K. The loops obtained at T = 5 K, displayed in figure 3.6, show a non-saturating character. The non-saturating tendency is particularly noticeable in D6: at $T = 5$ K, the average slope dM/dH is equal to 2.6 $\cdot 10^{-4}$ between 20 and 50 kOe for sample D6, to be compared to dM/dH= 1.91 $\cdot 10^{-4}$ for sample D15. The values of magnetization $M_{(5T\_5K)}$ at H = 50 kOe and T = 5 K are reported in table 3.2 together with the extrapolated (1/H tending to zero) saturation values ($M_{(S\_5K)}$). They increase with increasing D and with the Fe content. Such values are compared to those calculated (M_{calc}) considering the amounts of Fe and oxide derived from the XRD analysis and their saturation magnetization (for the oxide phase we have considered a saturation magnetization of 86 emu/g, corresponding to the average of bulk Fe_3O_4 and γ-Fe_2O_3). The ratio between $M_{(S\_5K)}$ and M_{calc} is also reported in table 3.2. The smaller D, the lower is the $M_{(S\_5K)}/M_{calc}$ ratio.

The coercivity H_C is reported as a function of temperature in figure 3.7a: H_C decreases with temperature for the three samples, the variation being more marked with decreasing D. In fact, at T = 5 K, H_C decreases with increasing D, whereas, at $T = 300$ K, it increases with D.

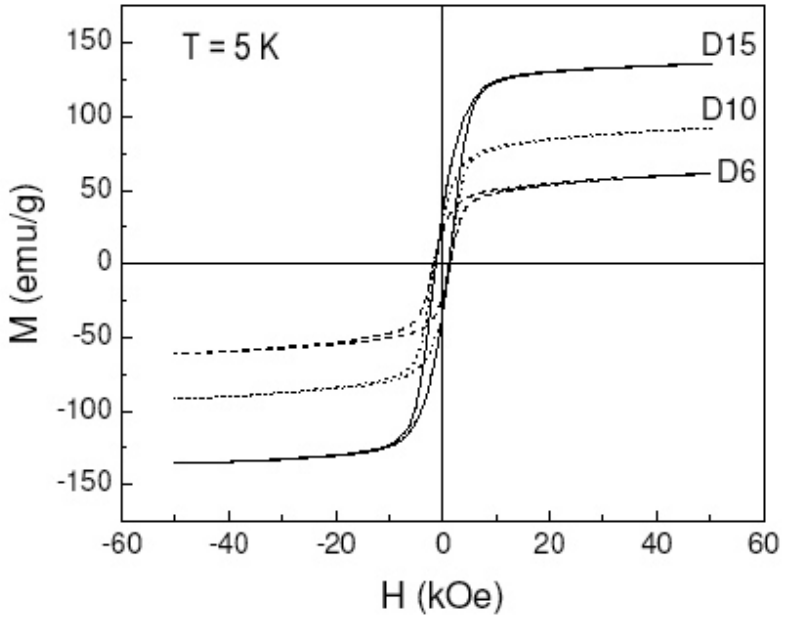

Figure 3.6: Hysteresis loops measured at T = 5 K on samples D6, D10 and D15.

The loops in figure 3.6 show a non-saturating character and a high value of the irreversibility field ($H_{\rm irr}$). This field is defined as the field above which the two branches of the loop in the first quadrant merge together in a single curve, the two corresponding magnetization values differing by less than 1%. At T = 5 K, $H_{\rm irr}$ has the largest value for D6 ($\sim$ 28 kOe) and it decreases with increasing D (figure 3.7b); in D6 it decreases with temperature up to $\sim$ 100 K and then it remains almost constant above $\sim$ 150 K. As for $H_{\rm C}$, a weaker thermal dependence is observed in D10 and still weaker in D15.

Table 3.2: $M_{(5T\_5K)}$, magnetization measured at T = 5 K and at H = 50 kOe; $M_{(S\_5K)}$, 1/H extrapolation of the magnetization at T = 5 K; $M_{\rm calc}$, calculated magnetization starting from XRD estimation of the constituent phases in table 3.1.

Sample	$M_{\rm 5T\_5K}$ (emu/g) ($\pm$0.5)	$M_{\rm S\_5K}$ (emu/g) ($\pm$0.5)	$M_{\rm calc}$ (emu/g) ($\pm$9)	$M_{\rm S\_5K}/M_{\rm calc}$ (%) ($\pm$5)
D6	61.4	68.8	110	62
D10	89.7	95.9	123	78
D15	135.8	141.2	165	86

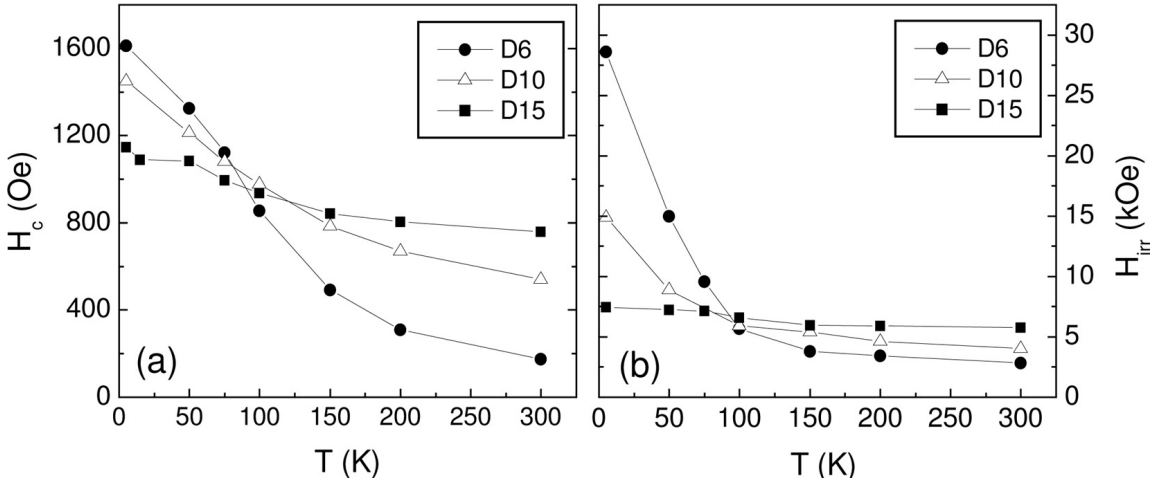

Figure 3.7: (a) Coercivity H_C and (b) irreversibility field H_{irr} as a function of temperature for samples D6, D10 and D15

Hysteresis loops were measured after cooling the sample in a magnetic field of 20 kOe, from T = 300 K down to a fixed temperature. At T = 5 K, a shift of the loop towards the negative field has been observed for the three samples. The amount of the shift is usually quantified through the positive exchange field parameter $H_{ex} = -(H_{right} + H_{left})/2$, where H_{right} and H_{left} are obtained from the intersection of the hysteresis loop with the x-axis. In figure 3.8, H_{ex} is shown as a function of temperature for the three samples. H_{ex} increases with decreasing D; for all the samples, it decreases with increasing temperature and it vanishes at $T \sim 150$ K.

Zero-field-cooled and field-cooled magnetization

The zero-field-cooled (M_{ZFC}) and the field-cooled (M_{FC}) magnetization vs T were measured at different applied magnetic fields (100 Oe $\leq H_{appl} \leq$ 20 kOe; M_{ZFC} was measured on warming and M_{FC} during the subsequent cooling). Some results for sample D6 are shown in figure 3.9a. For H_{appl} < 1000 Oe, the magnetic irreversibility persists up to temperatures close to 300 K. We define T_{irr} as the temperature where the difference between M_{FC} and M_{ZFC}, normalized to its maximum value at $T = 5$ K, for practical reasons, become smaller than 3%. With increasing H_{appl}, T_{irr} decreases, the shape of

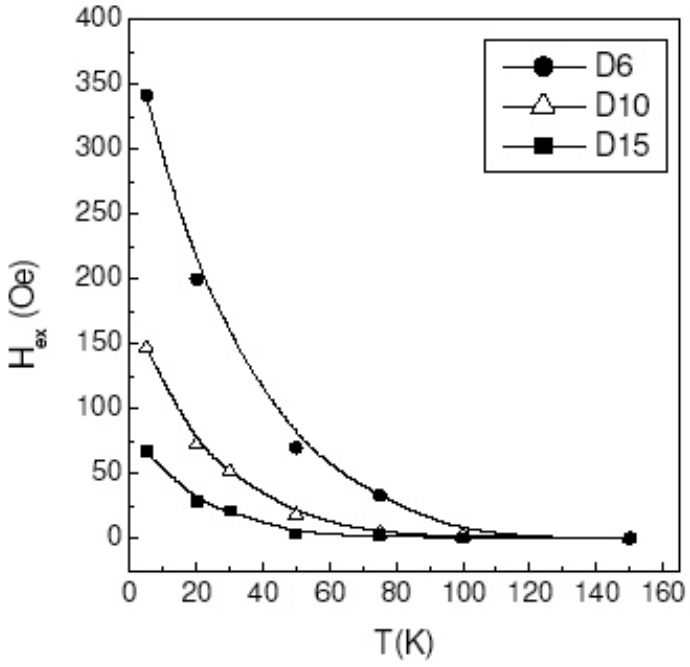

Figure 3.8: Exchange field (H_{ex}) as a function of temperature for sample D6, D10 and D15).

the M_{ZFC} curves exhibits a strong field-dependence, suggesting blocking/freezing phenomena at field-dependent temperatures. It can be noticed that magnetic irreversibility persists at low temperatures even at $H_{appl} = 20$ kOe. The temperature derivative of the difference (M_{FC}-M_{ZFC}) has been calculated: some representative $[-d(M_{FC} - M_{ZFC})/dT]$ curves are shown in figure 3.9b. A similar analysis was repeated on sample D15. In figure 3.10 we have reported: (a) M_{ZFC}/M_{FC} vs T for D6 and D15 at H_{appl} = 500 Oe, normalized to the M_{ZFC} value measured at $T = 5$ K (M_{ZFC_5K}) and (b) the corresponding $[-d(M_{FC} - M_{ZFC})/dT]$ curves.

Discussion

According to the TEM images 3.4 and considering the high oxide fraction (Table 3.1), the material can be modelled in terms of nanometric Fe particles dispersed in a poorly crystallized oxide matrix (figure 3.4b,c, figure 3.5).

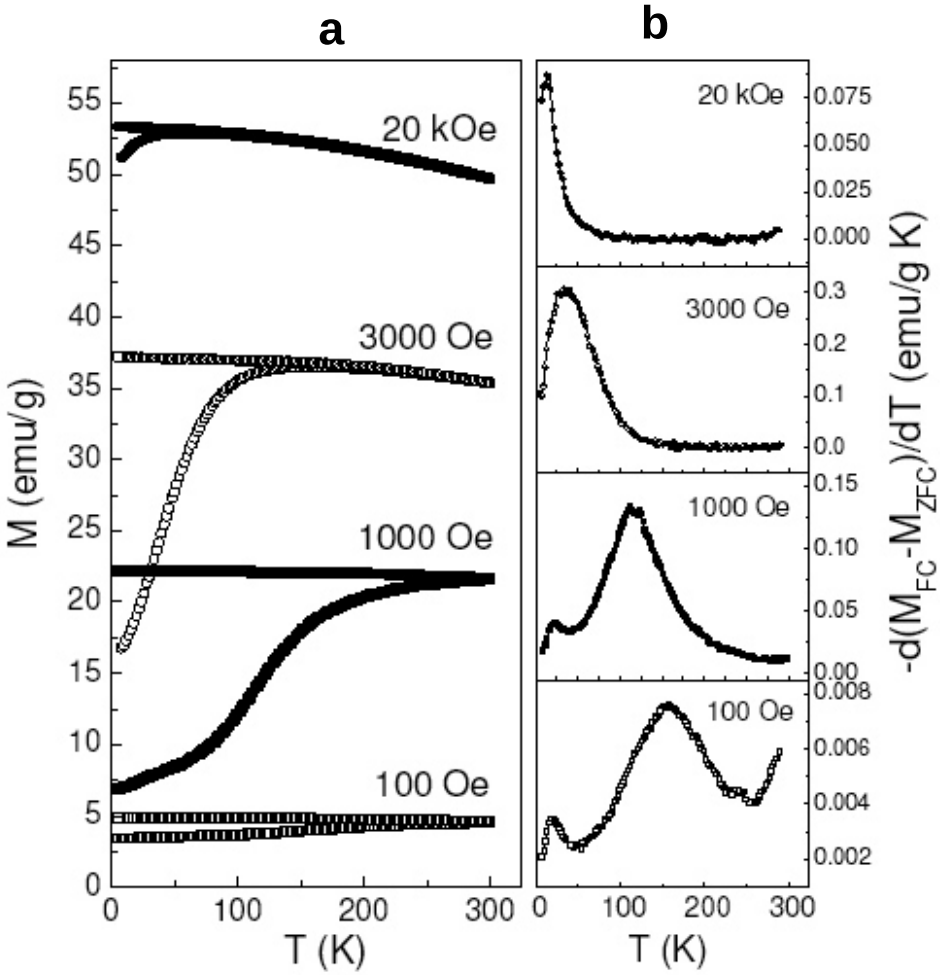

Figure 3.9: (a) Zero-field-cooled (ZFC, lower branch of each curve)) and field-cooled (FC, upper brunch) magnetization vs. T for different H_{appl} for sample D6. (b) Temperature derivative $[-d(M_{\text{FC}} - M_{\text{ZFC}})/dT]$ of difference between FC and ZFC magnetization.

Glassy magnetic nature of the oxide phase and progressive freezing of the system

We first discuss the properties of sample D6, in particular the hysteresis loop measured at T = 5 K (figure 3.6). The non-saturation tendency and the small magnetization value at H = 50 kOe well below the expected value, obtained by XRD on the basis of the Fe and oxide weight fractions listed in table 3.2, reveal a non-collinear arrangement of atomic moments. Such behavior is reminiscent of that found in ferrimagnetic particles (γ-Fe_2O_3, $NiFe_2O_4$) where the coexistence of topological disorder and frustration of

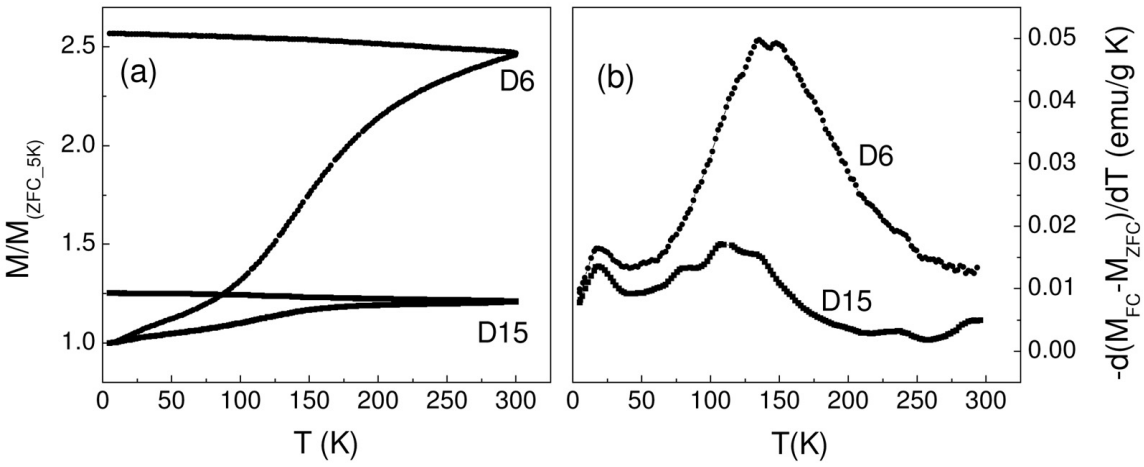

Figure 3.10: (a) $M_{\mathrm{ZFC/FC}}$ as a function of temperature measured at H_{appl} = 500 Oe on samples D6 and D15. The curves are normalized to the value of M_{ZFC} at T = 5 K ($M_{\mathrm{ZFC\_5K}}$); (b) temperature derivative of the difference between field-cooled and zero-field-cooled magnetization shown in (a).

magnetic interactions at the surface resulted in spin-canting and spin-glass-like behavior [130, 131]. In our sample, too, the spins of the structurally disordered oxide matrix could be frozen in a spin-glass-like state. This hypothesis is supported by the high irreversibility field $H_{\mathrm{irr}} \sim 28$ kOe at T = 5 K. The shift of the field-cooled hysteresis loop at T = 5 K (figure 3.8), is also consistent with this interpretation: it can be associated to the exchange anisotropy originating from the exchange coupling between the spin-glass-like matrix and the ferromagnetic crystallites.

Hence at very low temperatures, the interplay between matrix-particle exchange coupling and particle-particle dipolar interactions should result in a frozen disordered magnetic state for the whole system. In agreement with Mössbauer spectroscopy results [118], the hypothesized spin-glass-like state is not observed to evolve into a pure paramagnetic or superparamagnetic regime with increasing T up to 300 K.

The temperature derivative curves $[-d(M_{\mathrm{FC}} - M_{\mathrm{ZFC}})/dT]$ shown in figure 3.9b provide qualitative information on the effective distribution of anisotropy energy barrier of the system. A common feature of these curves is the presence of a weakly field-dependent peak at $T_1 \sim 20$ K, consistent with the presence of a low-temperature, frozen magnetic

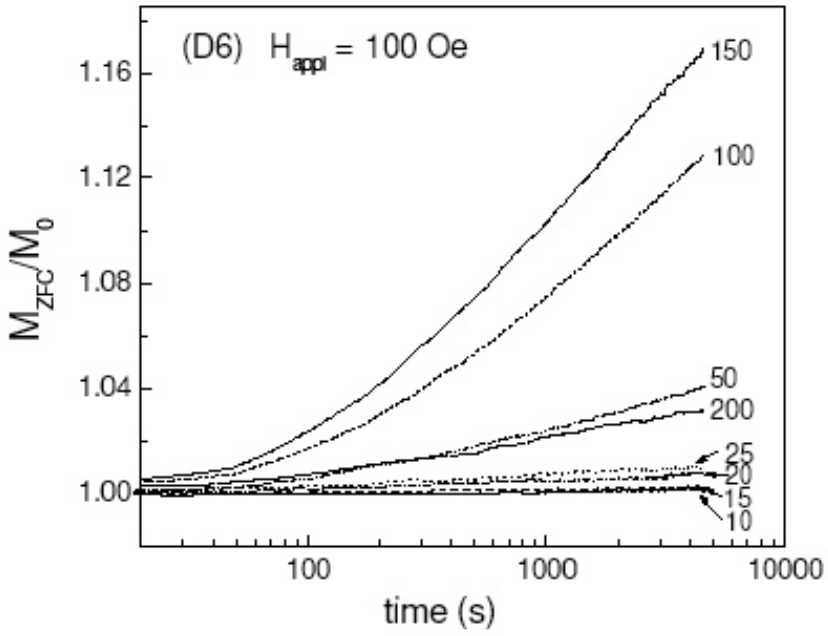

Figure 3.11: M_{ZFC} vs. time for H_{appl} = 100 Oe at the indicated temperatures. M_0 is the magnetization at the beginning of the measurements.

state for the whole system. This is also confirmed by the lack of magnetic relaxation below T = 25 K, as shown in figure 3.11, where the time dependence of M_{ZFC} is reported for sample D6 at different temperatures (H_{appl} = 100 Oe; note that the maximum relaxation is measured at T = 150 K). A second large peak is observed at a temperature T_2 ($T_2 \sim 150$ K for H_{appl} = 100 Oe): it becomes narrower and shifts to lower temperature with increasing field.

Dynamical magnetic behavior of the system: a simplified description

In a simplified picture, we can describe our system as constituted by two components, strongly coupled at the interface: a non-relaxing, (quasi-static) component (the Fe particles); a relaxing, magnetically disordered component (given by regions of exchange-interacting spins of the oxide matrix). Below T_1, the oxide region moments do not relax and are frozen in the spin-glass-like (or *cluster-glass*-like) state [132]. On increasing the temperature above T_1, these moments become progressively unfrozen, according to the distribution of effective anisotropy energy barriers, determined by their size and the strength of the magnetic interaction with the surroundings. The large peak in the

$[-d(M_{FC}-M_{ZFC})/dT]$ curve at H_{appl} = 100 Oe (figure 3.9b) reflects the width of such a distribution. Once the net moments of the oxide magnetic regions are able to thermally fluctuate, they tend to be polarized by the Fe particle moments, which thus prevent (or shift to higher temperature) the passage into the superparamagnetic regime. The polarizing action exerted by the Fe particle moments is enhanced by the magnetic field, favoring the formation of a ferromagnetic network throughout the sample.

Origin of the exchange field and thermal evolution of H_{ex} and H_C

It is found that H_{ex} appears below T = 150 K (figure 3.8), i.e., corresponding to the freezing of most of the moments of the oxide magnetic regions, as indicated by the value of T_2 in the $[-d(M_{FC}-M_{ZFC})/dT]$ curve at H_{appl} = 100 Oe (figure 3.9b); with lowering temperature below T = 150 K, H_{ex} shows a marked increase because of the progressive freezing of an increasing number of oxide region moments. The thermal evolution of H_c (figure 3.7a) is coherent with the above picture: at very low temperatures the frozen oxide matrix exerts a strong pinning action on the Fe particle moments whereas at T = 300 K, the oxide matrix is polarized by the Fe particles. Its contribution to H_c can be neglected compared to that of the Fe particles.

Dependence of the magnetic behavior on D

It is now useful to compare the results with those of samples D10 and D15. The features of the hysteresis loops reflect the differences in the chemical composition. $M_{(S\_5K)}$ increases with the Fe content and the difference between the calculated and measured magnetization decreases, confirming that the oxide phase is responsible for the magnetization reduction (figure 3.5, table 3.2). The non-relaxing component, and hence the ferromagnetic character, increases with D as revealed by the decrease of magnetic irreversibility in the M_{FC}/M_{ZFC} curves (figure 3.10a) and by the reduced non-saturating tendency in the loops of figure 3.6.

The observation that the low-temperature peak in the $[-d(M_{FC}-M_{ZFC})/dT]$ curves at H_{appl} = 500 Oe appears at the same temperature for D6 and D15 and that the strong peak is centered at a lower temperature $T_2 \sim 110$ K in D15 (figure 3.10b) confirms that none of the two is directly related to the relaxation of the individual Fe particles. If this were the case, the larger size of the Fe particles in D15 should imply higher anisotropy

energy barriers and hence the peaks should be centered at higher temperature. Actually, the peaks are probably associated with freezing processes involving spins of the oxide matrix. The low T_2 of D15, compared to D6, may be explained considering that the larger non-relaxing ferromagnetic component in D15 is the origin of a mean magnetic field, reducing the height of the energy barriers of the relaxing component and shifting the energy barrier distribution to lower values. H_C and H_{ex} at T = 5 K increase with decreasing D (figures 3.7a and 3.8), revealing that the exchange anisotropy effects at the interface between particles and matrix are more important when the surface to volume ratio of the particles increases. As observed for D6, in sample D15 H_{ex} appears below the temperature T_2 of the large central peak in the $[-d(M_{FC}-M_{ZFC})/dT]$ curve and then increases with reducing T. The temperature dependence of H_C, H_{irr} and H_{ex} becomes weaker with increasing D due to the increase in the ferromagnetic character and to the reduced oxide fraction.

Coercivity at room temperature: the inability of the oxide matrix to transmit the exchange interaction

On samples obtained by compacting Fe nanoparticles produced by IGC and not subjected to passivation, Löffler *et al*. found, at T = 300 K, $H_C \sim 30$ Oe for $D \sim 10$ nm (the maximum $H_C \sim 100$ Oe was measured for $D \sim 30$ nm) [133]. Their results have been explained considering that, despite the presence of voids and pores in the structure, the exchange interaction is able to couple the Fe particle moments, as described by the Random Anisotropy Model for nanocrystalline materials. The high room-temperature values of H_C of our samples rule out the possibility that the Fe particles are exchange-coupled and support the hypothesis that they are predominantly magnetic single-domain. Hence, the oxide matrix does not transmit the exchange interaction to neighboring Fe particles: this indicates a low effective exchange stiffness constant of the oxide matrix, which is consistent with the relaxing behavior of the oxide moments.

At T = 300 K, we could expect that an estimation of H_C is obtained by the Stoner Wohlfarth model according to which, for spherical single-domain Fe particles randomly oriented, the maximum coercivity value is given by the expression $H_C = 0.64\ K_{Fe}/M_S$ and amounts to ~ 180 Oe ($K_{Fe} = 4.8 \cdot 10^5$ erg/cm^3, magnetocrystalline anisotropy of bcc Fe) [134]. The H_C of D6 is in agreement with such a prediction, but in D15 $H_C \sim 800$ Oe. This could be due to the presence of a shape anisotropy contribution to the total anisotropy,

becoming more and more noticeable with increasing D, as confirmed by TEM analysis (figure 3.4e,f,h), which revealed elongated Fe-cores.

3.4 Electron holography investigation

3.4.1 The samples used for electron holography

The Fe nanoparticles for the electron holography analysis were produced by IGC in He atmosphere at a pressure of 10 Torr. Operating at such a high pressure gives a larger mean particle size D compared to the samples described in the previous section. The study of the magnetic properties of the nanoparticles, in relation to their two-phase character, required samples with a reduced size D and hence with a high oxide fraction. On the other hand, for the room temperature electron holography analysis, the particles have to be large enough to avoid the superparamagnetic phenomenon and to assure a good resolution in the holograms.

The nanoparticles were collected on a carbon coated Cu grid put inside the evaporation chamber during the synthesis process and then subjected to in-situ oxygen passivation. Hence, as the particles lie on an amorphous carbon film which gives a noise contribution to the phase map ($\approx 2\pi/30$), they should not be too small to avoid a decrement in the measurements quality. However, it should be remarked that the particles still present the characteristic core-shell morphology and so the conclusions we have achieved by the magnetic characterization in paragraph 3.3.3, especially regarding the role of the oxide layer as exchange interaction transmitter, are assumed to hold also in this case.

TEM observations reveal that also in very large particles of several tens of nm (see for instance figure 3.12), the thickness of the oxide layer is approximately 2 nm.

At the end of the evaporation process, in order to produce the samples for the electron holography observations, some nanoparticles were scraped from the cold finger of the IGC apparatus and subjected to the XRD analysis. The result is shown in figure 3.13: the peaks of the oxide phase are hardly visible, whereas those related to the bcc iron appear quite narrow. The Rietveld analysis gives a value of $D \sim 50$ nm whereas it does not

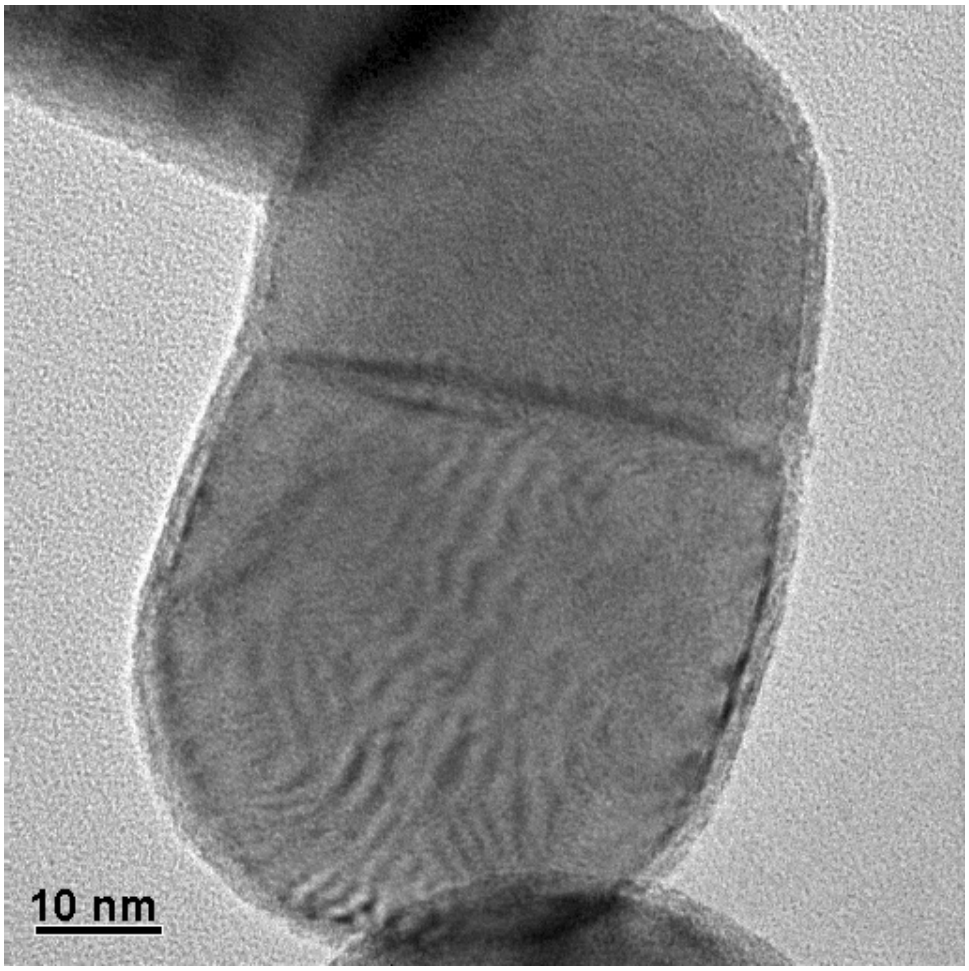

Figure 3.12: High resolution TEM micrograph of a selected particle in a chain

provide reliable results with regard to the iron and oxide fractions. However, assuming a spherical shape of the particles and an oxide layer of thickness d_s of about 2 nm (as it follows from TEM and XRD analysis in paragraphs 3.3.1 and 3.3.2), the iron volume fraction x_{Fe} can be estimated from the relationship [124]

$$d_s = (x_{Fe}^{-1/3} - 1)D_{Fe}/2. \tag{3.1}$$

It is found that $x_{Fe} \sim 80\%$ and accordingly the weight fractions are 86% and 14% for the iron and oxide phase, respectively.

The core shell morphology of the particle is well revealed also thanks to the observations employing energy filtered TEM (EFTEM, see paragraph 1.7). What we recognize

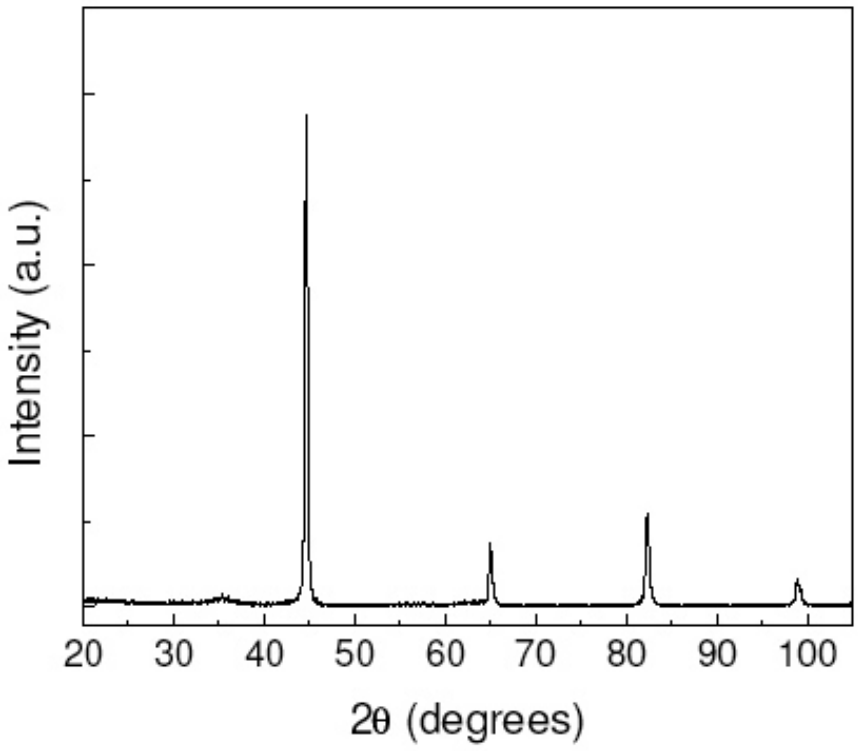

Figure 3.13: XRD spectrum of a sample evaporated by IGC for electron holography studies (using Cu-Kα radiation).

in these micrographs are the compositional maps of the Fe and the iron-oxide phase, obtained by selecting the energies of the transmitted electrons through the sample. Using this technique, we may evaluate the distribution of the elements in the sample: in figure 3.14b the lighter contrast represent the oxide layer, and we also see the core-shall structure of our particles. The thickness of the oxide layer can be determined from the image by measuring the width of the bright layer around the particles. The result is 3 ± 2 nm, in agreement with the values extracted from the high resolution TEM micrographs and also from the analysis of the X-ray spectra. As already said, this value seems to be independent of the size of the iron core.

Regarding the magnetic properties of this type of nanoparticles, at $T = 5$ K and H_{appl} = 50 kOe, the measured magnetization was 185 emu/g, as compared to the value calculated starting from the XRD results ($M_{\text{calc}} = 200$ emu/g). Note, that the ratio between the measured and calculated values is very close to 1 (0.93), as expected from the reduced oxide fraction in agreement with the discussion in paragraph 3.3.3. Figure 3.15 shows the

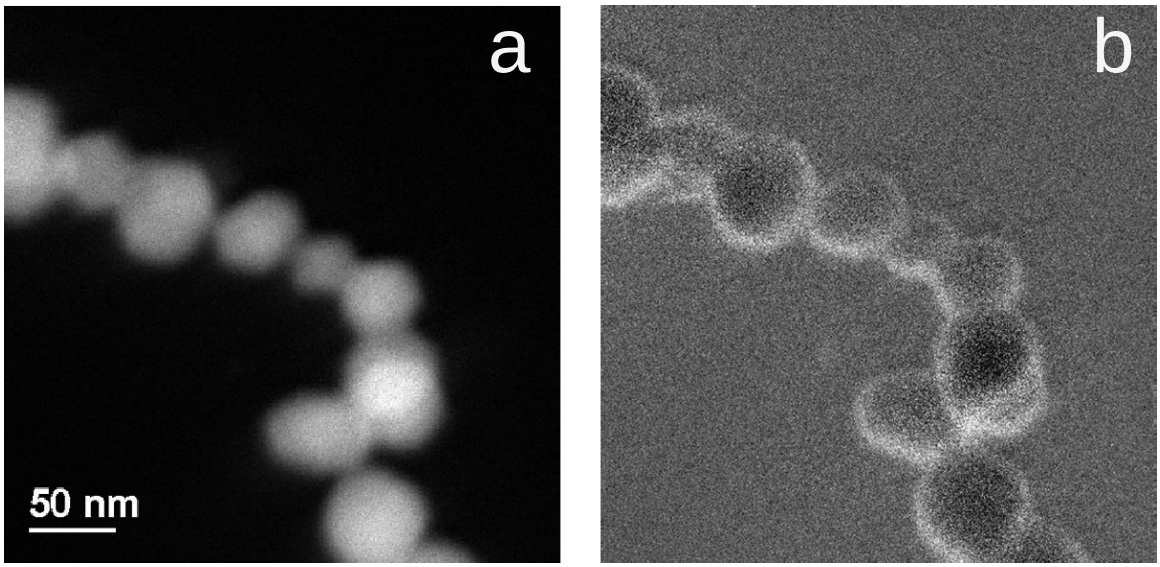

Figure 3.14: EFTEM image of a selected chain of particles: (a) represents the Fe map, and (b) represents the oxide map, where the lighter contrast indicates the oxide layer. Notice that the oxide map is affected by a specimen drift of the order of 1 nm during the 20 seconds exposure time to record the image.

coercivity H_C as a function of temperature: H_C decreases with increasing T passing from ~ 350 Oe at $T = 5$ K down to ~ 230 Oe at $T = 300$ K.

3.4.2 Electron holography results

As recognized from figure 3.14, the evaporated nanoparticles tend to arrange themselves in chains on the Cu grid. Figure 3.16 is the reconstructed hologram of a typical chain, composed of several particles with size between 30 and 70 nm. Because the chain was too long to be recorded in only one hologram, it has been necessary to shift the sample in the *xy* plane and then, three holograms have been recorded to get the reconstructed image of the whole chain of figure 3.16. The principal characteristic is that each particle shows circular contour lines, as it is expected for three dimensional particles close to a spherical shape. It should be noted that only a weak magnetic flux is leaking out of the particle chain, as can be recognized from the few black and white fringes running outside the chain. The contrast of the fringes is affected by noise, caused by the supporting

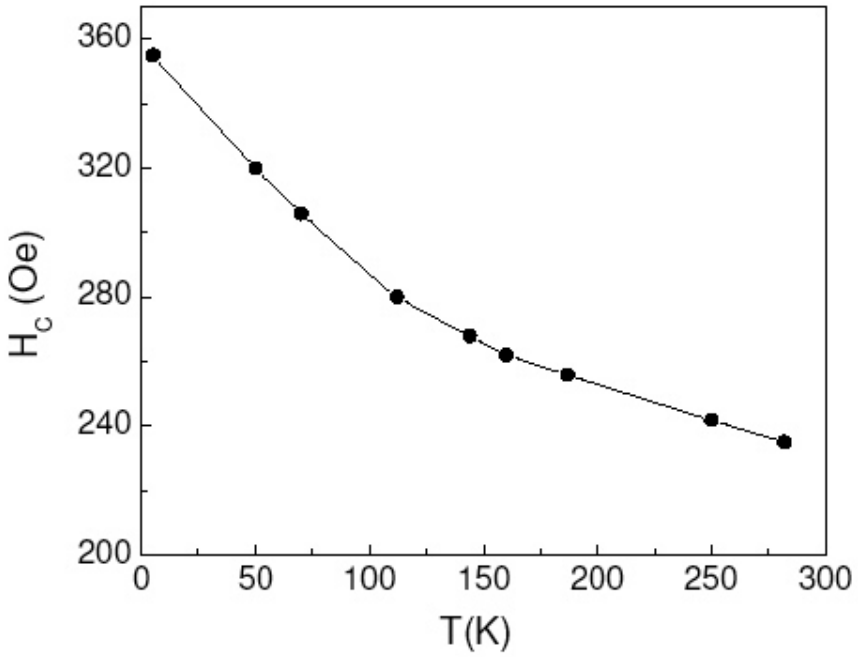

Figure 3.15: Coercivity H_C as a function of temperature for Fe nanoparticles, which are similar to those observed by electron holography.

amorphous carbon film. Similar results have been found for a large number of holograms recorded on selected regions of different particle chains.

The hologram of a chain of five Fe nanoparticles is displayed in figure 3.17a; figure 3.17b is the reconstructed phase map shown modulo $2\pi/6$. The thickness variation map (modulo $2\pi/4$) and the magnetic phase maps (modulo $2\pi/6$), obtained according to the procedure described in section 1.2.1.2, are displayed in figure 3.17c and 3.17d, respectively. In figure 3.17c each dark contour line connects the points with constant thickness of the sample. The thickness of the particles can be estimated from the knowledge of the phase difference between two successive contour lines, and taking into account the total number of lines displayed on the map, the mean inner potential of Fe ($V_0 = 29.0$ V [135]) and the experimental E and λ values, using the equation

$$\Delta\phi(x,y) = C_E \int V_{cryst}(x,y,z)dz - \frac{2\pi e}{h} \int\int B(x,y) \cdot dS, \tag{3.2}$$

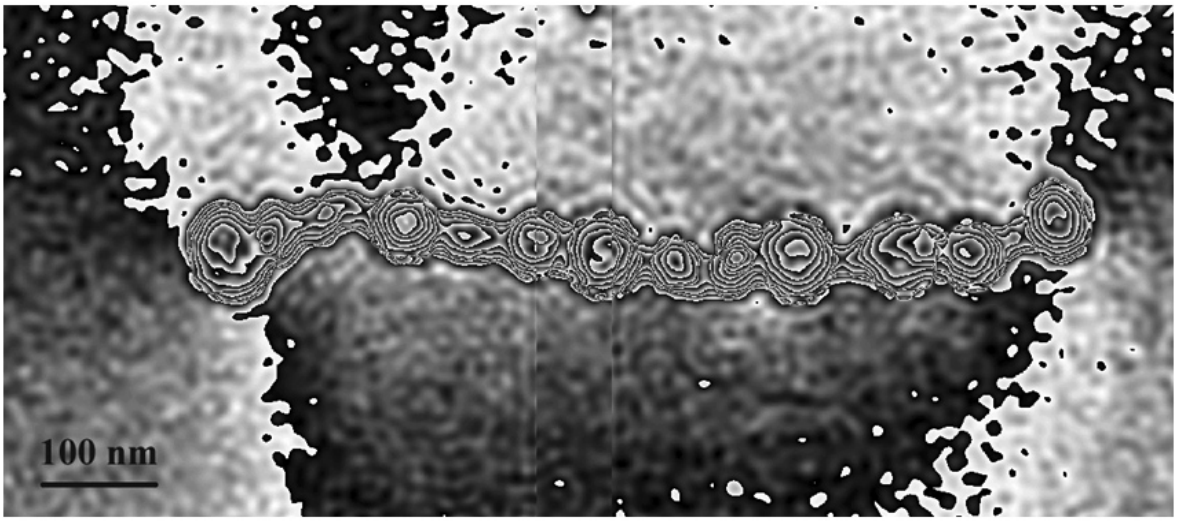

Figure 3.16: Reconstructed phase map of a typical chain composed of different iron particles. Three holograms have been recorded to compose the reconstructed image of the whole chain.

where the first integral is taken along a trajectory parallel to the beam direction z, V_{cryst} is the crystal potential of the object, B is the magnetic flux density and S is the area between the two trajectories going from the source to the detector through the vacuum and the sample respectively, both ending in the same point at the electron hologram. C_E is a wavelength-dependent constant (see equation 1.7. Note that E, λ, e are the electron's acceleration voltage, their wavelength and charge, respectively, h is Planck's constant.

The first integral is carried out along a closed path represented by the classical electron trajectories, and the second is performed over the surface enclosed by such trajectories. In general, for most of the particles, the ratio between the lateral dimension and the estimated thickness is ~ 1.3, indicating that the particles are not spherical but oblate.

In figure 3.17d, a weak magnetic flux leaking out of the chain is visible. Two fringes, one above and one below the chain of particles, can be recognized. They correspond to only $2\pi/6$ phase difference therefore, the effect of the noise is enhanced. Since the particles tend to arrange themselves in a linear chain it is expected that their magnetic moments lie along the chain axis, in the plane of observation. Under these conditions, the chain of figure 3.17d can be approximated by a cylinder of magnetization M and therefore,

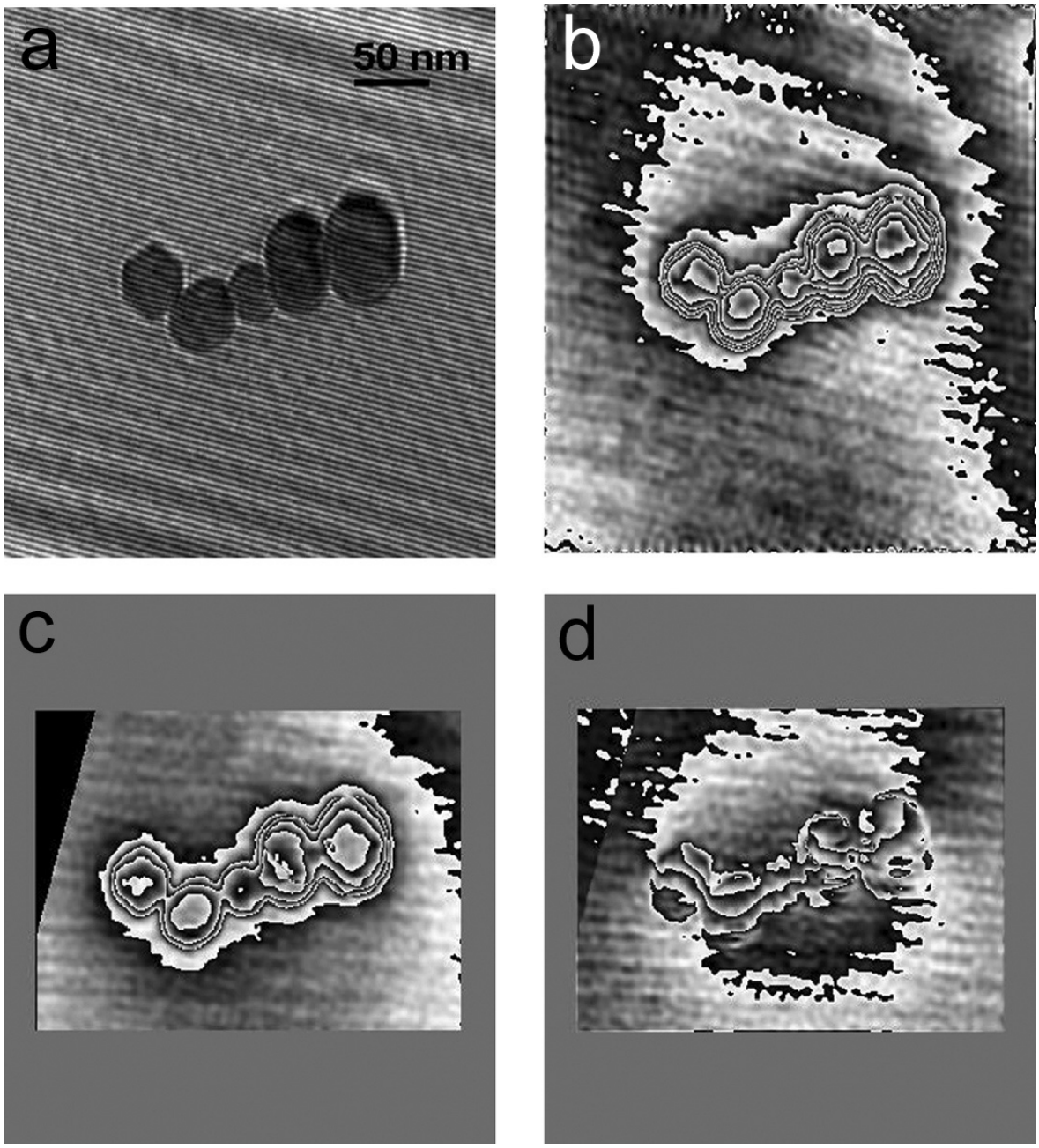

Figure 3.17: (a) Hologram of a nanoparticle chain; (b) phase contour map (modulo 2π/6) extracted from the hologram in (a); (c) phase map of thickness variations (modulo 2π/4); (d) magnetic phase map (modulo 2π/6).

M can be derived by equation 3.2, under the assumption that the detected leakage flux is a measure of (*MS*), where *S* is the average cross-sectional area of the cylinder (on account of the elongated shape of the particle chain, we assumed that the demagnetizing

field does not contribute substantially to the magnetic flux). If each particle were a pure single magnetic domain, a value of M close to the saturation magnetization of bulk-Fe ($M_S(\mathrm{Fe})$) should be expected. However, a value of $M \sim 40\%$ of $M_S(\mathrm{Fe})$ is measured [1], thus suggesting that a partial closure of the magnetic flux must occur inside each particle (note that the superparamagnetic limit for spherical Fe particles is ~ 20 nm in diameter). However, the particles are too small to support the formation of a classical multi-domain configuration, because their sizes are comparable to the domain wall thickness δ, given by the relation $\delta = \pi L$, where L, the exchange correlation length, is ~ 23 nm for bulk Fe.

In figure 3.18b, a phase map of a different particle chain is shown. Figures 3.18c and 3.18d are the thickness map and the magnetic field map projected onto the object plane, respectively. The leakage field in figure 3.18d, corresponds to a value of M below 50% of $M_S(\mathrm{Fe})$. The magnetization pattern inside the chain appears extremely complex, probably because of the presence of overlapping regions between adjacent particles. Nevertheless, in some localized regions a circular configuration of the flux lines is clearly observable. Such a pattern is consistent with an inhomogeneous state of the particle magnetization, such as the curling or vortex state.

Recently, the vortex state configuration of particle magnetization has been predicted theoretically by several groups [100, 105]. In particular, Rave and co-workers calculated the lowest energy state of small cubic particles, with uniaxial magnetic anisotropy, as a function of anisotropy strength and particle size by finite element micromagnetic calculation [100]. The study allows to draw a phase diagram, shown in figure 3.19, which reports the particle size (in units of $\sqrt{A/K_d}$, where A is the exchange stiffness constant and $K_d = B_S^2/\mu_0$, with B_S being the saturation induction) as a function of the relative anisotropy $Q = K_u/K_d$ with K_u as the uniaxial anisotropy constant.

The diagram defines the boundaries between three kinds of micromagnetic states: the single-domain state (SD) for small particle sizes, the regular multi-domain state (MD) for large particles, and for low-anisotropy particles an intermediate, continuously flowing state which it may be called vortex state (V). To find the V-MD-boundary the authors

[1] To estimate the magnetization of a particle chain we refer to the chain in figure 3.17a. In d we reveal two fringes of $2\pi/6$ phase jump, that corresponds to a total phase shift of $\phi = 2\pi/3$. Because $\phi = \mu_0 MS 2\pi e/h$, substituting the known values, we obtain $\mu_0 M = 0.98$ T. The ratio $M/M_S(\mathrm{Fe})$ is then ~ 40 %.

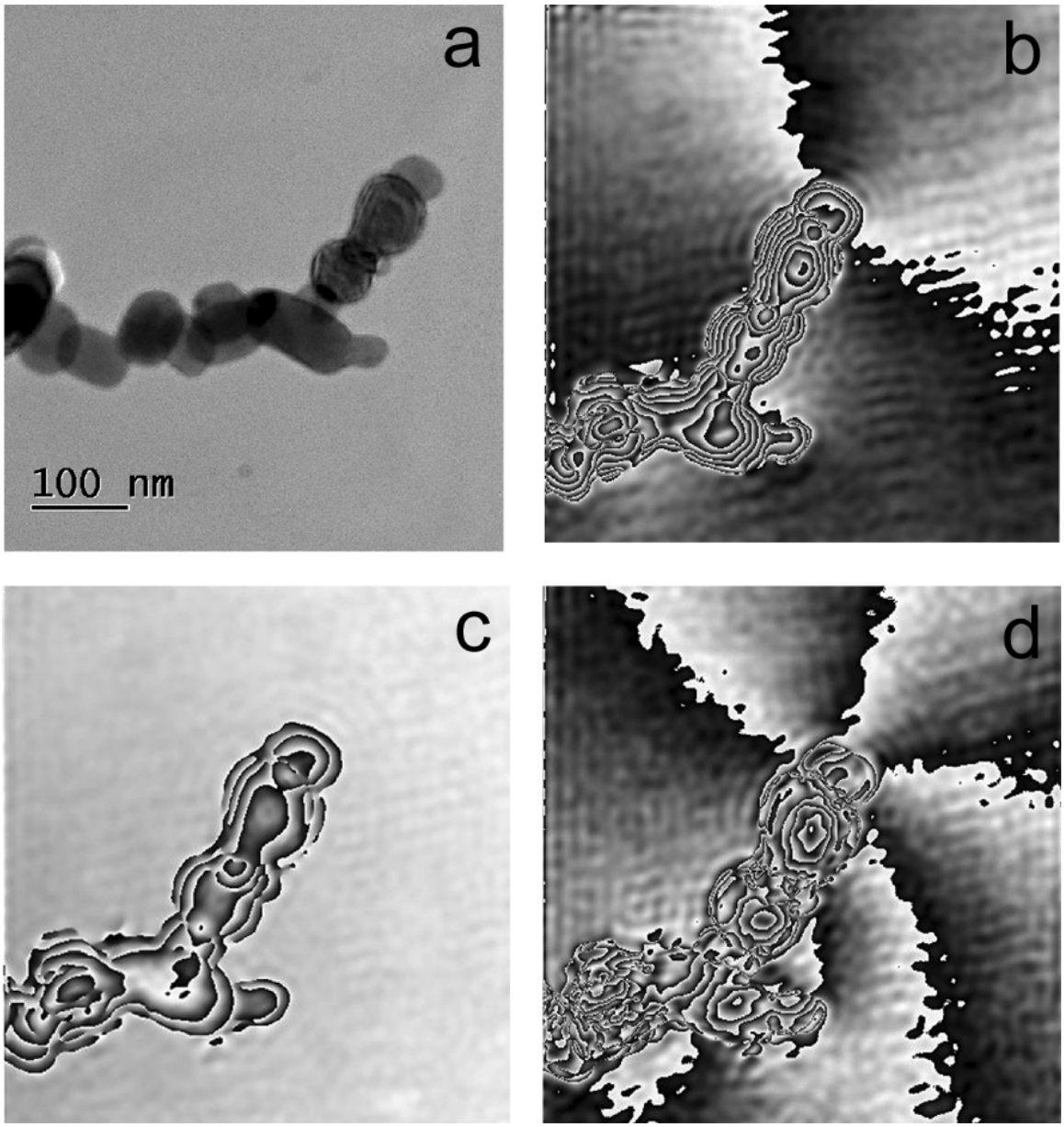

Figure 3.18: (a) Image of a chain of nanoparticles; (b) phase contour map (modulo $2\pi/4$) at the extremity of a nanoparticle chain; (c) phase map of thickness variations (modulo $2\pi/2$; (d) magnetic phase map (modulo $2\pi/8$).

defined a multi-domain state to consist of at least *three* domains. The vortex states and multi-domain states are clearly different in character for small Q. In a vortex state, the stray field energy is largely avoided at the expense of exchange stiffness energy, while the anisotropy plays no role. In multi-domain states the weak anisotropy energy begins

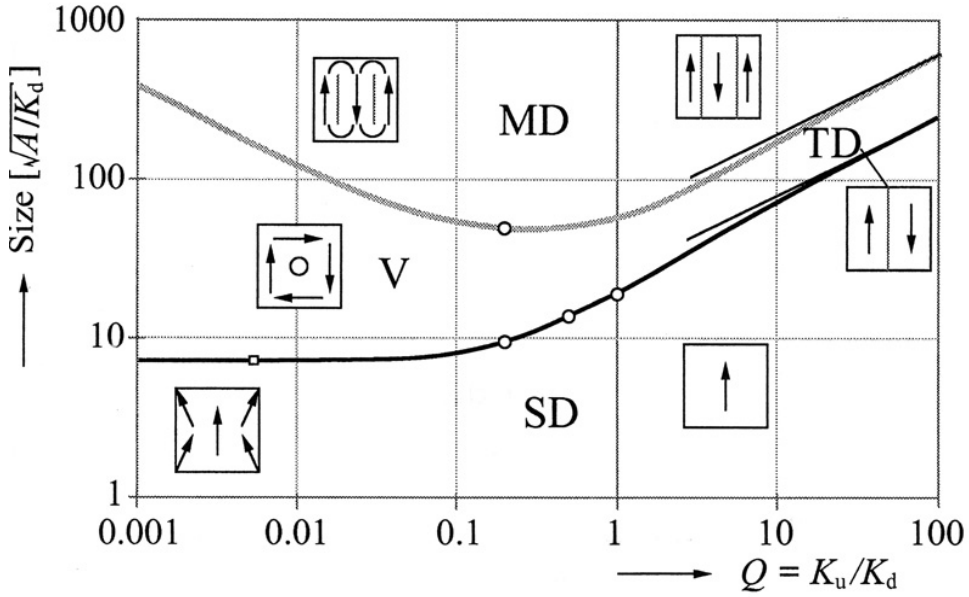

Figure 3.19: Simplified phase diagram for the presence or absence of domains, applicable to cubical particles with a uniaxial anisotropy: SD single domain state, V vortex state, TD two-domain state, MD multi-domain state. After [136].

to become important so that these states resemble ordinary domain states. This difference in character vanishes for the large Q, but all states can be continuously followed towards rising Q. The three micromagnetic state are better visualized in figure 3.20.

The observation by magnetic force microscopy by Shinjo *et al*. [106] on circular dots of permalloy, where the dot thickness becomes much smaller than the dot diameter, present clear evidence for the existence of a vortex spin structure (see figure 3.1). Moreover, Dunin-Borkowski *et al*. reported studies using electron holography on bidimensional circular magnetic Co dots [137] that also show vortex magnetization states. Ross *et al*. have inferred the presence of vortex magnetization states in conical ferromagnetic particles (cobalt and nickel particles with truncated conical shapes), by comparing their remanent states, as deduced by magnetic hysteresis measurements, with a three-dimensional micromagnetic model [105].

For bcc iron K_d is equal to $3 \cdot 10^6$ J/m^3 and A is of the order of 10^{-11} J/m and $\sqrt{A/K_d} \sim 2$ nm. Assuming the crystalline anisotropy constant of bulk Fe, $K_{Fe} = 4.8 \cdot 10^4$ J/m^3, Q is of the order of 10^{-2}. Therefore, according to figure 3.19, particles with size

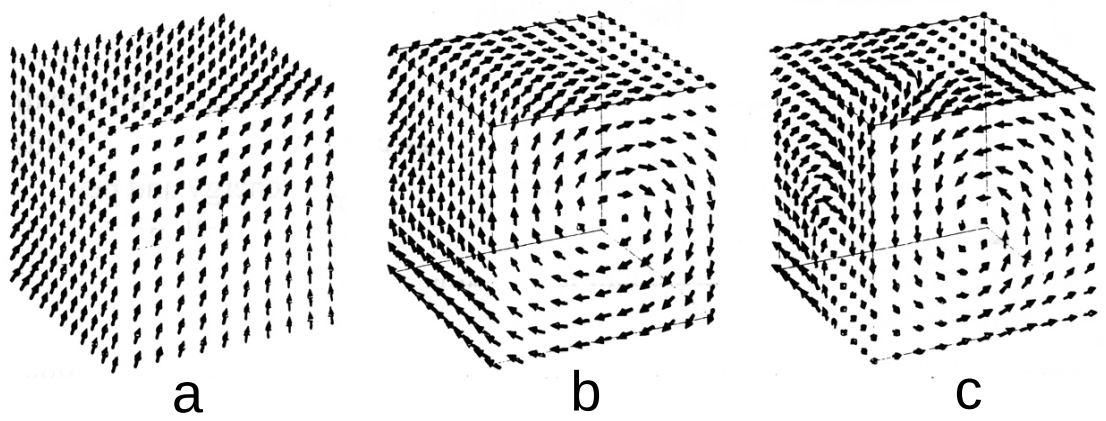

Figure 3.20: Schematic representation of micromagnetic states of small cubic particles. (a) The high-remanence flower state that continuously develops out of the uniformly magnetized state. (b) The vortex or curling state modified by trying to stray parallel to the cube edges. (c) A complex state found at larger particle sizes, which is related to a three-domain state. After [53].

between 20 and 200 nm should exhibit a vortex magnetic microstructure. Although the model by Rave *et al*. imposes severe restrictions on the particle features and hence cannot be straightforwardly applied to our case, it is worth noticing that the sizes of the analyzed Fe nanoparticles are largely within that range.

Coming back to our electron holography results, it should be recalled that the observed contour fringes represent a projection of the actual magnetization pattern onto the object plane. For an ideal, no-remanence, single-vortex state, closed contour fringes can be well distinguished if the vortex axis displays a component along the electron beam trajectory, whereas if the vortex axis is perpendicular to the electron trajectory, no fringes will appear in the contour map. In this last case, but assuming now that a remanent magnetization exists inside the particle, some (not closed) contour fringes may be observed, as seems indeed to be the case of figure 3.17d. The investigated Fe particles are not perfectly spherical and it may be expected that the shape anisotropy contributes to the total magnetic anisotropy. However, Rave's model predicts that for particles with size comparable to that of our Fe particles, the vortex state persists also for an anisotropy constant value up to one order of magnitude larger than K_{Fe}.

In the above discussion we have considered that the particles in the chain magnetize independently. The results in paragraph 3.3.3 demonstrate that the oxide layer surrounding each particle exhibits cluster-glass-like properties and, at room temperature, it prevents the exchange coupling between the moments of adjacent Fe particles. Hence, as far as exchange interactions are concerned, each particle can indeed be considered independent. As regards dipolar interactions among the particles, the presence of magnetization structures similar to vortices is expected to contribute by itself to reduce them.

In section 3.3.3, with regard to the samples D6, D10 and D15, we have explained that the high coercivity values at room temperature were consistent with a single-domain configuration of the Fe particles. The strong increase of H_C as D increases (H_C is about 760 Oe in D15, figure 3.7a) was proposed to be due to the contribution of shape anisotropy, since with increasing D the symmetry of the particles deviate more and more from the sphericity, as indicated by TEM observations. In the present case of particles with larger mean size, the foreseen formation of inhomogeneous magnetization patterns with low remanence should imply a reduced shape anisotropy contribution and hence a lower coercivity at $T = 300$K, as indeed observed (figure 3.15).

3.5 Conclusions

In this chapter, an extensive study on the magnetic properties of oxygen passivated Fe nanoparticles, synthesized by gas-phase condensation, has been presented. In particular, the nanoparticles have been investigated at room temperature by high-resolution electron holography, gaining an insight into their magnetic configuration together with valuable indications on the versatility of such imaging techniques for the study of 3-dimensional nanostructures.

To achieve this goal, we have also relied on structural and magnetic characterization results, establishing a relation between low temperature magnetic properties and particle structure and composition. In fact, samples with different mean Fe core size (D) and different Fe to oxide ratios were analysed by means of TEM, EFTEM, XRD and magnetization measurements at $5 \leqslant T \leqslant 300$ K. TEM, EFTEM and XRD results indicate

that the particles are surrounded by a poorly crystallized oxide layer about 2 nm thick, independent of the Fe core size.

The magnetic character of the oxide phase is inerently cluster-glass-like. Actually, the magnetic results for cold-compacted particle samples ($6 \leqslant D \leqslant 15$ nm) are consistent with a progressive freezing of the oxide moments, with decreasing T from 300 K. Below $T \sim 20$K, the freezing of the oxide in the glassy state is complete and the interplay between oxide-particle and particle-particle interactions results in a frozen state for the whole system. At $T = 300$ K, the high H_C values ($\sim$180 Oe for D6 and up to 760 Oe for D15) indicate that the relaxing oxide phase is not able to transmit the exchange interaction to neighboring Fe particles that are essentially single-domain. The strong increase of H_C, passing from D6 to D15, is ascribed to a shape anisotropy contribution. In fact, with increasing D, the symmetry of the particles deviates more and more from the spherical one, as indicated by TEM results.

The electron holography observations have been made on Fe nanoparticles with mean size $D \sim 50$ nm, arranged in linear chains. We have considered that the particles magnetize independently, with respect to exchange interaction. In fact, as stated above, at $T = 300$ K, the oxide shell prevents the coupling between the moments of two adjacent Fe cores.

Several holograms have been recorded on different chains. In all cases a weak leakage magnetic flux has been observed, from which a magnetization value has been derived, corresponding to about 40-50 % of the saturation magnetization of bulk-Fe. This result indicates that a partial closure of the magnetic flux occurs inside each particle, despite the small size (comparable to the characteristic Fe domain-wall thickness) that is not consistent with the formation of a classical multidomain magnetic configuration. The electric and magnetic phase maps have been disentangled by properly combining two holograms recorded before and after reversing the sample upside down. The latter represents a crucial passage in the observation of 3-dimensional particles, not free of technical difficulties. In localized regions of some chains, the phase map is characterized by a circular configuration of the flux lines, consistent with an inhomogeneous state of the particle magnetization, indicating a vortex configuration.

The formation of such low-remanence states has been discussed with reference to theoretical predictions [100] and accounting for the particle size and Fe magnetic anisotropy. The consequent decrease in the particle magnetostatic energy implies a reduction of the dipole-dipole interaction and may also explain the lower $H_C \sim 170$ Oe measured on such particles, compared to sample D15.

4 Magnetic force microscope tips: quantitative magnetic characterization

4.1 Introduction

Magnetic force microscopy has proven to be a useful tool for the characterization of magnetic systems, especially thin films, magneto-recording materials and patterned arrays of magnetic elements (for a review, see [138]). The magnetic domains of magnetic recording materials as well as technically written bit patterns can be investigated with high spatial resolution and minimal sample preparation (for an introduction to the MFM technique, see paragraph 1.4.3).

As in other scanning probe techniques, the formation of the MFM image contrast is not straightforward. In most cases it is influenced by perturbations arising from tip artifacts, surface topography, or tip-sample interactions, all of which are in general difficult to differentiate. MFM tips show different magnetic behavior according to their magnetic configurations. Therefore, in MFM observation it is essential that an appropriate tip can be used in the observation of a specific sample. To give two examples, for imaging a soft magnetic sample one can not use a strongly magnetized tip, or if a hard magnetic material is studied one should not use a soft magnetic tip. Two particular problems arise when using an MFM. One is related to the usually unknown magnetic state of the tip, and the second one is related to the stray field emanating from the sample which may lead to perturbations of the magnetic state of the tip and thus of the observed MFM signal. These problems can result in misinterpretation of the images, which then it translated in a growing interest in the quantitative analysis of experimental data obtained by MFM and

therefore, several research groups worked on the magnetic characterization of the MFM tips.

Heydon *et al*. [139] developed a new high sensitivity resonant torque magnetometry technique, enabling the in-situ determination of the magnetic properties of magnetic force microscope tips. Kong *et al*. [140] used as a calibration method metal rings with inner diameter of 1 to 5 μm, fabricated using electron-beam lithography. By the current flowing in the ring, they determined a MFM tip's effective magnetic charge q and an effective magnetic moment m along the tip axis.

In a recent paper Van-Schendel *et al*. [141] used a calibration sample to calibrate the MFM measurements that allows a quantitative determination of the sample stray field. In such a sample micron sized domains coexisted with sub-micron domains in order to probe the stray field of the MFM tip. Using a mathematical model of the tip field, they could extract quantitative data of the magnetic field of the tip.

Theoretical work on the quantitative interpretation of MFM images, e.g., the tip to sample interaction [142], MFM-image simulation ([143] and referencies therein), and micromagnetic modeling of magnetic force microscopy tips [144] has helped to understand the image formation in MFM. But the qualitative and especially quantitative characterization of an image, as well as the analysis of possible probe-induced artifacts, relies on the detailed knowledge of the magnetic structure of the ferromagnetic probes used for detecting sample stray fields. Unfortunately, it is almost impossible to obtain a detailed calculation of the internal magnetic structure as well as of the stray magnetic field produced at the near-apex of the magnetic tip.

Various experiments carried out for MFM probe characterization were mainly focused on the observation of the stray field emanating from the tips, because of the low electron transparency of common tips. Either Lorentz microscopy or electron holography have been used for revealing the magnetic field around the tip apex [145–149].

Sueoka *et al*. [145] used several direct methods to characterize the MFM probes: 1) they could get information on the field generated by the MFM probe by TEM observations in the Foucault mode, 2) they observed the fringe field emitted from the MFM tip by using the micromagnetic resistive effect and 3) in order to investigate the magnetic characteristics of an MFM tip, they observed the MFM response to an inductive recording head.

These methods gave quantitative magnetic information on the MFM tips, but related to the static magnetic state of the probe and not to the dynamic magnetic properties.

Using the technique of differential phase contrast (DPC) Lorentz electron microscopy, Scott *et al*. [146] calculated the magnetic stray field distribution from magnetic force microscopy tips in a plane in front of the tip, using tomographic reconstruction techniques. Also Ferrier *et al*. [147] carried out a similar study on an MFM probe by Lorentz electron microscopy and reconstructing the field distribution by tomography.

Frost *et al*. [150] and Matteucci *et al*. [148] applied electron holography for the study of the leakage field of thin-film ferromagnetic tips used as probes in magnetic force microscopy. To get quantitative information of the local flux emanating from the ferromagnetic tips and therefore to evaluate the perturbation induced by the microprobe stray field on the sample area, they made simulations by assuming that the magnetic domain structure of the layer could be replaced by a uniform distribution of magnetic dipoles. Later, Streblechenko *et al*. [149] applied the far-out-of-focus implementation of electron holography in a scanning transmission electron microscope (STEM) for the analysis of the magnetic field emanating from a sputtered-deposited MFM tip. For the quantitative analysis, with the challenge of analyzing the three-dimensional field emanating from the tip apex, they made simulations with the assumption that the field emanating from the tip probe can be expanded in a multipole expansion.

A sophisticated MFM tip preparation in order to study the external stray field emanating from the tips as well as their internal domain structure was proposed by Rührig *et al*. [151]. Tiny smooth carbon needles covered with a thermally evaporated magnetic thin film are transparent to the electron beam used in TEMs. A weak but highly concentrated stray field was observed emanating from the immediate apex region of the tip, consistent with the capability for high resolution in MFM imaging.

As already mentioned, a restriction to the application of electron microscopy techniques is that common MFM tips are not transparent to the electron beam. On the other hand, it has been shown that the electron holography technique is a useful tool to obtain reliable information about the near-apex field configuration of the tip and that the qualitative analysis of the images is quite straightforward. The revealed leakage flux around

the MFM tip apex can be studied at least in an integral way by measuring the total deflection along the trajectories of electrons close to the ferromagnetic tip, as described by Matteucci *et al*. [148].

In the context of our work, we investigated high coercivity tips, which were coated with CoPt permalloy magnetic crystallites, prepared by magnetron sputtering, followed by annealing at 650 °C in Argon atmosphere. Our work aimed to quantify the **B** field at different distances from the tip apex and therefore to distinguish good from bad tips for experimental use. This research work involved also the group of Prof. S.-H. Liou (Nebraska University, Lincoln) who have kindly provided us with the MFM probes and carried out the complementary magnetic characterization.

4.2 Experimental

The CoPt binary alloy with face centered tetragonal (fct) structure has chemical stability, hard magnetic properties, which are consequence of its high magnetocrystalline anisotropy ($K = 4 \cdot 10^6$ J/m^3), and a relatively large saturation magnetization ($M_s = 800$ emu/cm^3 [152–155]. These properties make CoPt alloy a suitable coating material for high coercivity MFM tips.

The $Co_{50}Pt_{50}$ alloy was magnetron-sputtered on silicon substrates using a home-made multi-gun sputtering system. Figure 4.1 displays two hysteresis loops measured at $T = 6$ and 300 K on a CoPt film (nominal thickness 5 nm) on a silicon substrate after an annealed treatment at 650 °C for 12 hours. The value of the saturation magnetization, about 800 emu/cm^3, and the high coercivity, around 20 kOe, are consistent with the presence of the desired fct structure.

The tips were fabricated following the same procedure as for the films. In this case, a 7 nm thick CoPt film was deposited on commercially available silicon cantilevers, on the two front sides, and only Pt on the back sides. A sketch of the MFM tip on a cantilever shows this orientation in figure 4.2. In particular, the tip fabrication involves three steps: magnetic thin film deposition, thermal treatment and tip magnetization. The as-deposited tips were annealed in a furnace at 650°C for 12 hours. The last step was realized using a superconducting magnet. A magnetic field of 70 kOe was applied in the direction

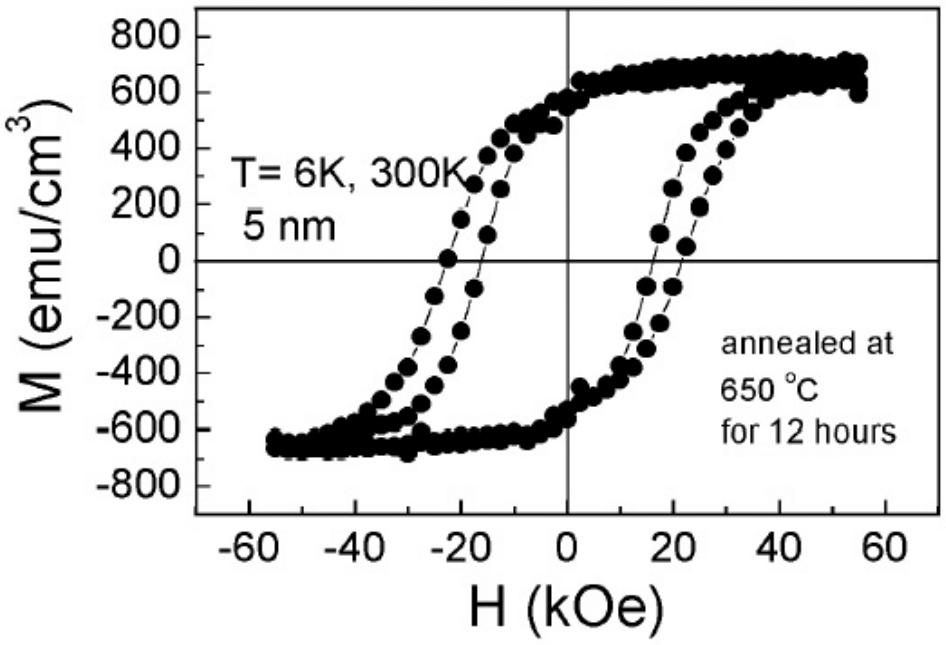

Figure 4.1: Hysteresis loops, at T = 6 and 300 K, for a sputtered CoPt film on a Si substrate, after annealing at 650 °C for 12 h.

perpendicular to the surface of a magnetic sample placed in front of the tip for MFM investigation, that is 10° off the tip-axis direction (see figure 4.2).

A scanning electron microscope (SEM) image of one of the CoPt MFM tips is shown in figure 4.3 (a and b represent the same tip with different magnifications). This image has been recorded with a SEM LEO 1530 Gemini FEG. As shown in figure 4.3a, we see that CoPt particles (the white features on the black background) are uniformly dispersed on the surface of the tip. The deposited CoPt layer is so thin, that it is no longer continuous after annealing. At higher magnification we observe that the crystallites also form at the apex of the tip. The size of the magnetic crystallites lies in the interval 10 to 200 nm.

In the following, the term "tip-axis" will indicate the axis parallel to the vector lying along the height of the pyramidal tip, and the z-axis the optical axis of the electron microscope.

Figures 4.4 illustrates the MFM images of thin-film recording heads taken with MFM tips analyzed in this research work. The images were taken with line traces horizontally across the gap of the thin-film recording head. The light and dark contrast in

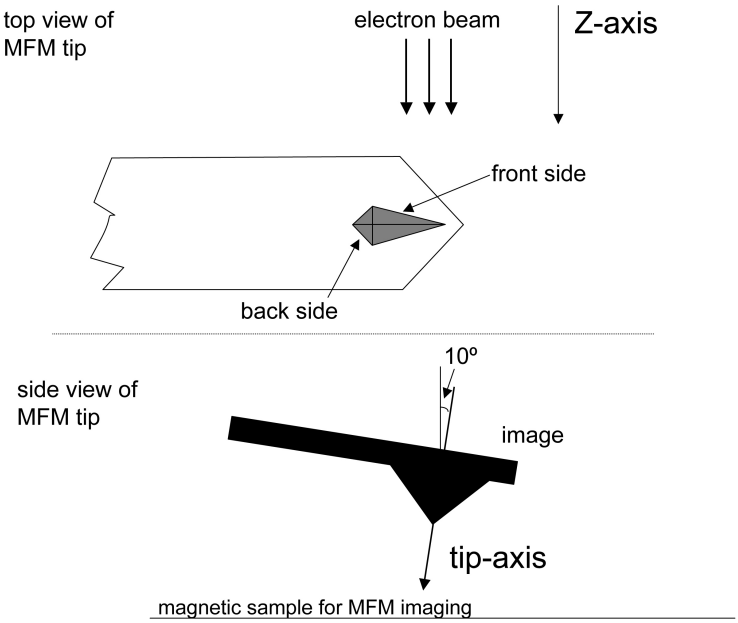

Figure 4.2: Sketch of a pyramidal tip on a cantilever to show the incident direction of the electrons on the tip. The tip-axis and the z-axis are indicated.

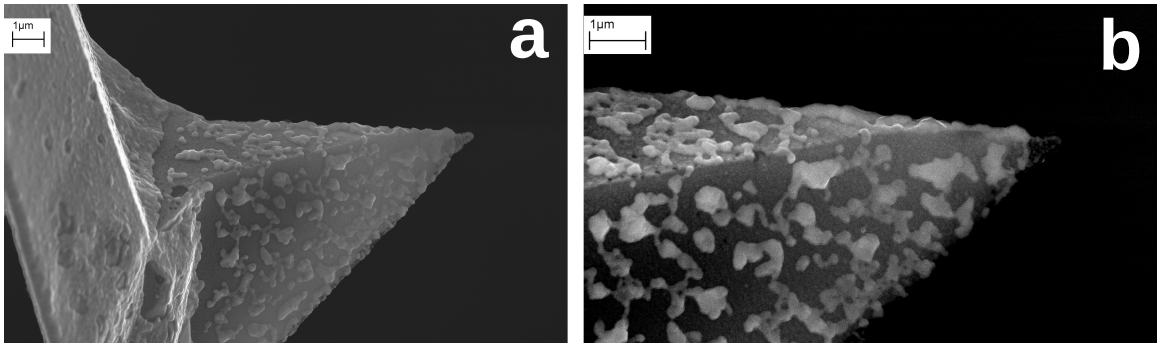

Figure 4.3: (a) Scanning electron microscopy image of a CoPt high H_C MFM tip and (b) an enlarged view of the tip area.

figure 4.4 corresponds to the strength of the stray-field gradient on the sample surface (see paragraph 1.4.3). To refer to one tip or another, in the following we will call the tips with a specific label. Therefore, the labels in figure 4.4 indicate with which tip the MFM image has been recorded. In particular, the images labeled HA90-5a/6a correspond to

images recorded using strongly magnetized tips, whereas images labeled Hp2, Hp15 and S114 are recorded with MFM probes subjected to a weaker magnetic field.

4.3 Results and Discussions

To be able to record holograms of the MFM probes, we have produced a special holder where we could fix the MFM tip including the commercial cantilever. The basis of the pyramidal microprobe is parallel to the z-axis (see figure 4.2).

The phase maps recorded on a series of different tips are represented in figure 4.5; each of them was chosen, such that a small particle occupies the apex of the tip. This is clearly visible looking at the high resolution TEM micrograph of the tip in figure 4.6. Holograms have been recorded in low-magnification mode (figures 4.5a and c) and also at high magnification mode, with the help of the Lorentz lens (figures 4.5b and d). The recording mode with the Lorentz lens switched on, allows us to image only the tip apex: in that case the full scale width of the images is 0.5 μm; in the low magnification mode the full scale width of the images is about 4.5 μm. When we record the hologram of a strongly magnetized tip at high resolution, the reference wave passes through a relatively strong leakage field region. Therefore, the phase shift is reduced compared with holograms taken with a true plane-wave reference wave. In our specific case, we observed that at high magnification, the measured leakage field is strongly modified by the perturbed reference wave, resulting in a value which is approximately half the value measured in low magnification mode. Accordingly, the low magnification holograms are important to extract the actual phase shift caused by the tip (figure 4.5c) and the high resolution hologram can help us to relate the structural configuration with the leakage field of the tip (figure 4.5d). These considerations do not apply to weakly magnetized tips because the leakage field of the tip does not interfere with the reference wave or only slightly.

The noisy region of the image represents the position of the tip. There we could not record any phase shift because the tip is not transparent to the electrons. In Table 4.1 is reported a list of the features of the analyzed tips.

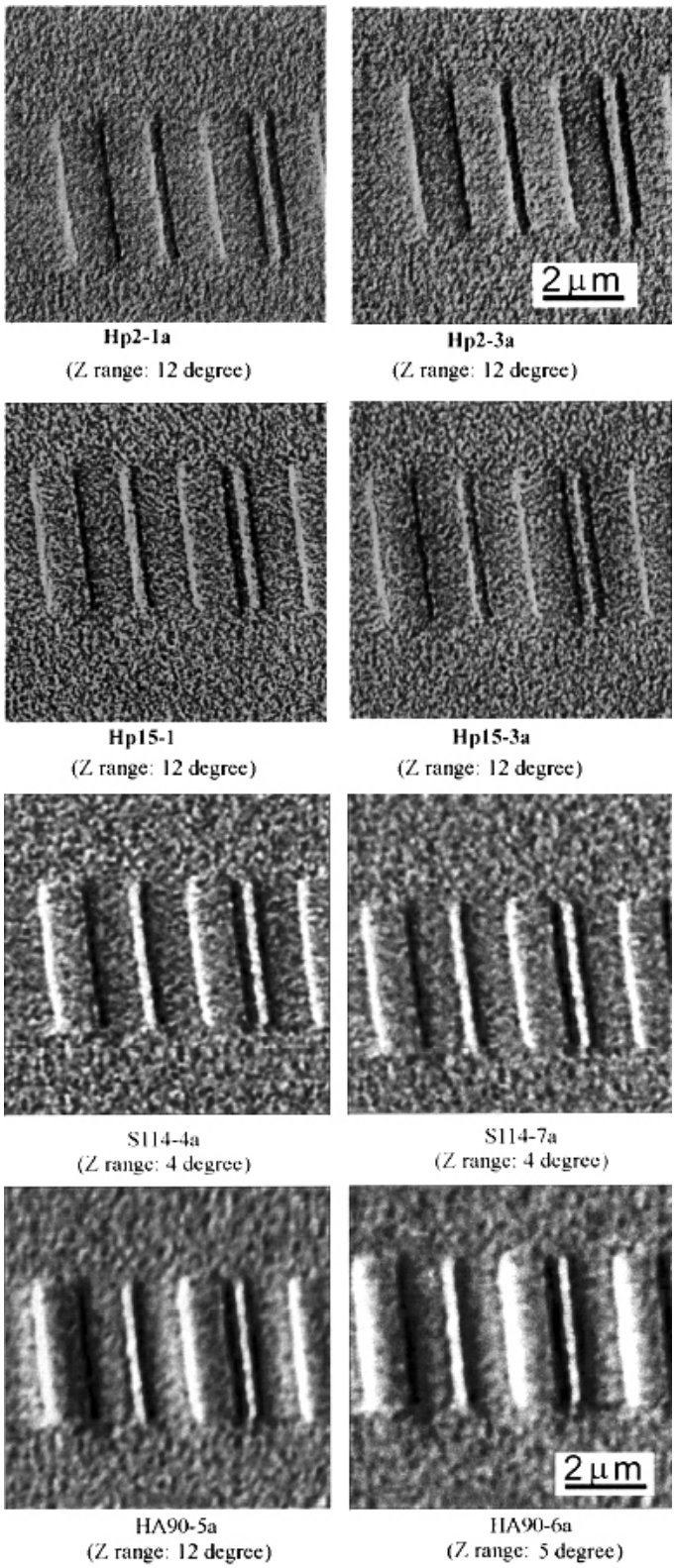

Figure 4.4: Magnetic images of thin-film recording heads using high H_c CoPt tips which were magnetized along the tip-axis. The label refer to the name of the tip used to record the respective MFM image. The different Z-ranges, reported in the images, indicates along which direction the MFM tips were magnetized with respect to the specimen normal.

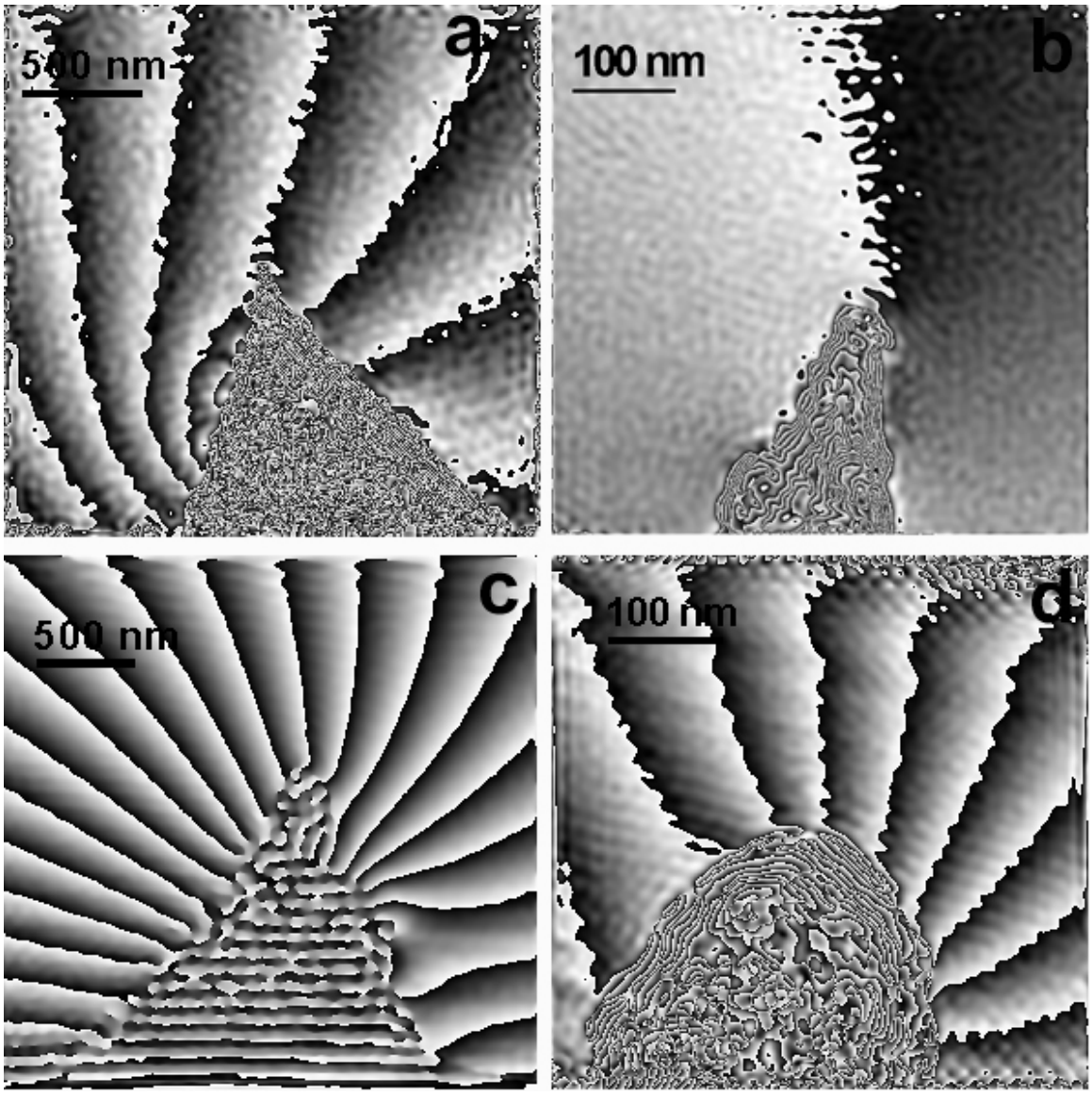

Figure 4.5: Reconstructed phase maps of different MFM tips subjected to different magnetic field intensity (before the TEM observation) and at different angles with respect to the tip axis. (a) Phase map of tip Hp15-2a recorded in low magnification mode and displayed modulo $2\pi/6$; (b) phase map of tip Hp2-3a recorded with Lorentz lens, displayed modulo $2\pi/8$; (c) and (d) are the reconstructed phase maps of the same tip HA90-6a, recorded in low magnification mode (modulo $2\pi/2$) and with Lorentz lens mode ($2\pi/4$).

Going from the reconstructed phase map to the 3-D magnetic field distribution is an ill-posed mathematical problem: many different three dimensional magnetic field distribution can result in the same two dimensional phase map. The integral equation 1.8 leads

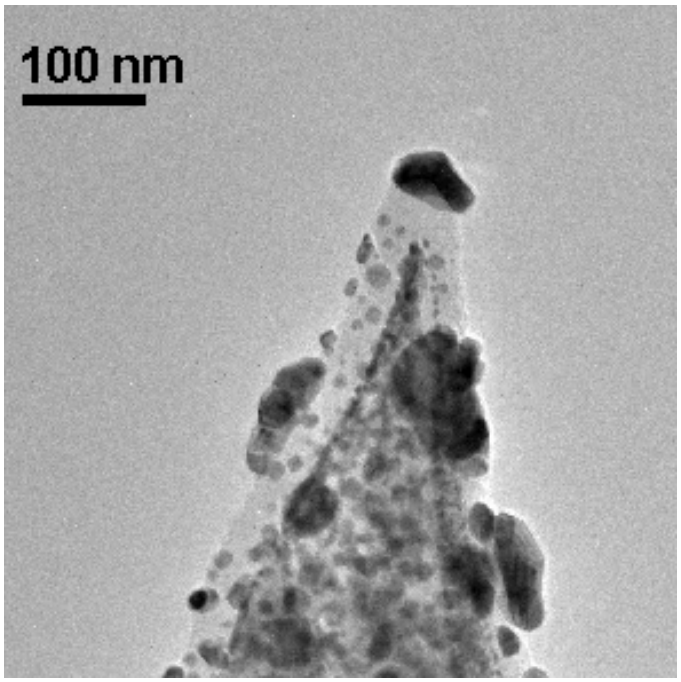

Figure 4.6: High resolution TEM image of a MFM tip. A particle of CoPt lies at the apex of the tip.

to this multiple relation between the phase map and the 3-D field. Therefore it is necessary to use a model of the tip field and to fit it to the observations. That does not mean

Table 4.1: Characteristics of the magnetic force microscope probes analyzed by electron holography.

Label	CoPt front sides	Pt back sides	M	Direction of M from tip-axis
HP15-1	20 nm	32 nm	5.5 T	12 °C
HP15-2a	20 nm	32 nm	5.5 T	12 °C
HP2-1a	10 nm	16 nm	5.5 T	12 °C
HP2-3a	10 nm	16 nm	5.5 T	12 °C
S114-4a	20 nm	-	5.5 T	12 °C
S114-7a	20 nm	-	5.5 T	12 °C
HA90-5a	$\sim$ 30 nm	-	5.5 T	0 °C
HA90-6a	$\sim$ 30 nm	-	5.5 T	0 °C

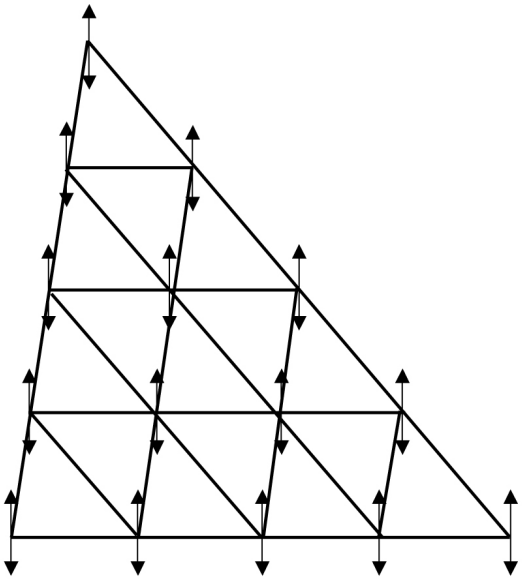

Figure 4.7: Sketch of the distribution of dipoles on the tip surface of the MFM tip. The length of each dipole is approximately L = 30 nm. This choice has been made to put a dipole in the vicinity of the position of a CoPt particle and to approximate the shape of the MFM tip. In our simulation we considered 15 dipoles.

that we achieve a unique solution but we obtain an approximated value of the B field with the correct order of magnitude.

For this purpose we consider a very simple model in which the tip apex is approximated by a series of "macroscopic" magnetic dipoles, uniformly distributed on the tip surface. The dipole length is approximately L = 30 nm (see sketch of dipole arrangement in figure 4.7). The length of the dipoles results from the best simulation obtained for the selected reconstructed phase maps.

To calculate the three components of the external field we consider the expression of a magnetostatic scalar potential associated to each dipole. This potential is given by

$$V_{\mathrm{m}}(x,y,z) = \frac{Q_{\mathrm{m}}}{4\pi}\left\{\frac{1}{[x^2+y^2+z^2]^{1/2}} - \frac{1}{[(x+L)^2+y^2+z^2]^{1/2}}\right\} \tag{4.1}$$

where Q_m and L are the hypothetical magnetic charge and the dipole length. The length and the magnetic charge of the dipoles have been determined by counting in the simulated

phase map the number of flux lines that were crossing a fictive line of a fixed length placed at a certain distance from the tip apex and comparing that with the number of flux lines in the reconstructed phase map at the same distance. The phase shifts produced between the reference and the object waves have an electrostatic and a magnetostatic component. Here only the magnetic field part relevant to the analysis of the MFM tips is examined since the electrostatic component, caused by possible charging, is negligable outside these tips.

The computer simulation of the field leaking out from the MFM probe can be written by formulating the recording principle of electron holography (see paragraph 1.2) and introducing suitable boundary conditions. The phase difference between the interfering object wave and reference waves, revealed in the recording plane, can be written as [6,32]

$$\Delta\phi = \frac{2\pi e}{h} \int\int_{S} \mathbf{B} \cdot \mathbf{n}\, dS, \tag{4.2}$$

where dS is the element of the area S between the two trajectories going from the source to the detector through the vacuum and the sample, respectively, both ending in the same point at the electron hologram. **B** is the magnetic flux densitiy, and n is a unit vector perpendicular to the surface (see also equation 1.8). If we consider $x = a$ and $x = b$, two points in the space brought to interference, we can solve the 4.2 as follow

$$\Delta\phi(x,y) = \frac{2\pi e}{h} \sum_{j} \int_{-\infty}^{+\infty} dz \int_{a}^{b} B_y(x,y,z)dx \tag{4.3}$$

where B_y is the y-component of the magnetic flux density B, generated by one linear dipole. The sum $\sum_j$ runs over all the dipoles considered in the simulation.

In paragraph 1.2 we have already said that an electron hologram is a two-dimensional projection of the total flux of the magnetic field of the sample investigated. That means that in our simulation we are looking for the two-dimensional projection of the leakage field in the symmetry plane xy, perpendicular to the beam direction z, choosing the y-axis parallel to the interference fringes at the biprism fiber. With this special choice of the coordinate system we have to consider only the y component of the magnetic flux density in the xy-plane, i.e. $B_y(x,y,0)$. This facilitates the calculation of the integral 4.3 along the z-direction in a small neighborhood of the origin, considered at the tip apex.

A simulated hologram will display the phase difference between the object wave that runs near the tip apex through the leakage field of the tip itself and along the *z*-axis, and a reference wave, which is considered at infinite distance from the tip apex. Therefore, we assume that in our model the reference is not perturbed by the leakage field of the tip. With these boundary conditions the phase shift of a single dipole at x_1 would be given by

$$\begin{aligned} \Delta\phi(x_1,y) &= \phi(x=\infty,y)-\phi(x=x_1,y)= \\ & 2y\frac{Q_{\mathrm{m}}}{4\pi}\left\{\frac{1}{y}tan^{-1}\frac{x}{y}+\frac{1}{y}tan^{-1}\frac{(x+L)}{y}\right\}_{x_1}^{\infty}. \end{aligned} \tag{4.4}$$

The projected distributions of the magnetic flux of the probes HP15-2a and Hp2-3a are displayed in figures 4.8 a and b.

In figures 4.9 a and b we report the trend of the absolute value of B in the plane of observation xy. For the tips Hp-15-2a and Hp2-3a we have calculated B at different distances from the apex of the tips. The values are reported in table 4.2.

Table 4.2: Examples of values of B_y along the tip-axis, indicated in figure 4.9, for the tips Hp-15-2a and Hp2-3a calculated at different distances from the tip apex.

	Tip 1	Tip 2
distance	B (mT)	B (mT)
25 nm	65	132
50 nm	22	72

Instead of performing a fit of a tip-model to the measured data, to extract quantitative information from the phase map, it is possible (within certain limits, see below), to measure in the phase map the number of equiphase line that penetrate a certain unit area A of a hypothetical sample placed at a certain distance in front of the tip. This results in a function f(A,x,y), and the number of equiphase lines considered is proportional to the magnetic flux (2π difference correspond to h/e). However, this function does not represent the 3-D magnetic flux since the phase shift is integrated along the z-direction, i.e. the electron beam path.

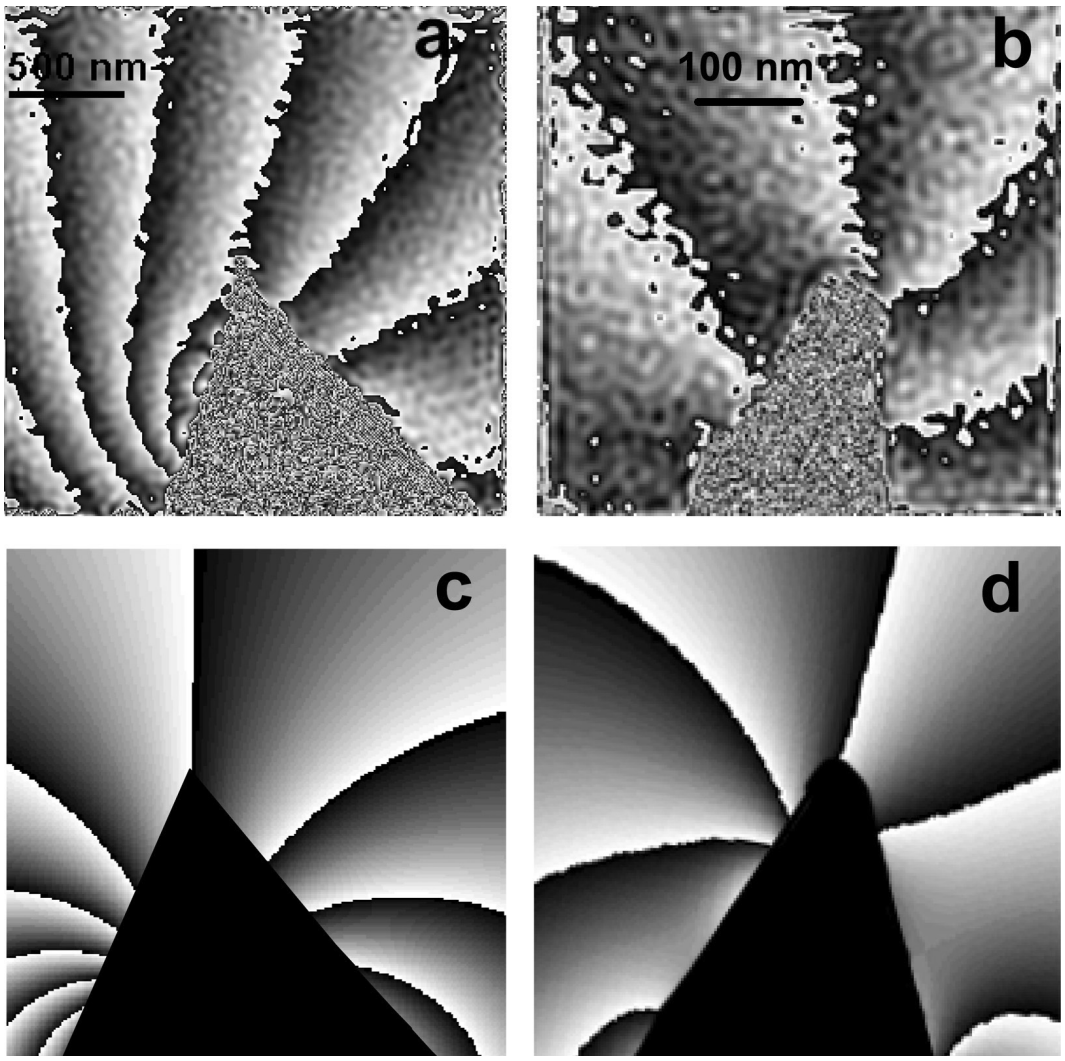

Figure 4.8: (a, b) Reconstructed phase maps of tips Hp15-2a and Hp2-3a, respectively; (c, d) simulated phase maps of the same tips. For details about the simulation, see text.

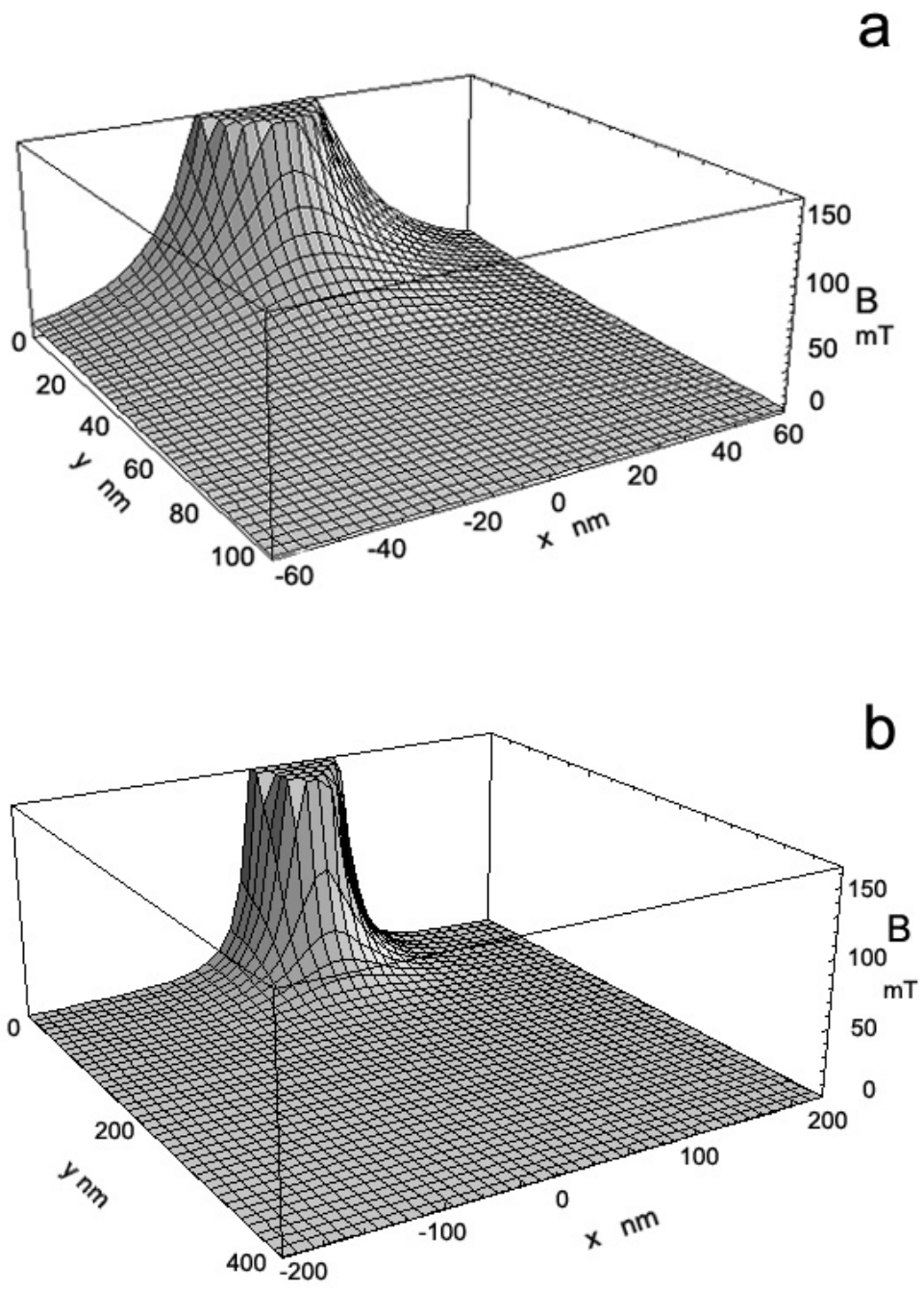

Figure 4.9: Trend of the absolute value of the B field of tip Hp15-2a (a) and Hp2-3a (b).

We tried experimentally to place a magnetic thin film sample in front of the MFM tip using our special sample holder, which could also move the sample forward and backwards with respect to the probe. Unfortunately, what has been recorded in the experimental hologram was shadowed by the sample itself, and therefore we could not yet gain the real position of the sample to respect to the MFM tip. Further optimization to avoid this shadowing effect due to the tilting of the sample are in progress, changing, for example, the geometry of the sample it self.

4.4 Conclusions

In this chapter we have presented new results on the analysis of high coercivity MFM tips. The tips, prepared by deposition of CoPt film alloy on a silicon substrate are characterized by the presence of a single small CoPt particle deposited on the tip apex of the MFM probe, a feature that should enhance the resolution of the technique itself.

This work was aiming to distinguish between good and bad magnetic probes by studying the leakage field spreading out of the tip. This allows us to establish how the magnetic field of the tip could interfere during MFM studies with the magnetic field of the sample. This has actually been one of the particular questions that many researchers (as cited in paragraph 4.1) have been trying to answer, in order to be able to deconvolute the tip-sample magnetic interaction. In this way it was possible to get a reliable quantitative interpretation of the recorded MFM images.

For this reason electron holography has proven to be a reliable technique to image the flux lines of the magnetic field of the MFM tip without introducing any magnetic perturbation during the analysis. Our experimental data could be interpreted with the help of computational simulation and we could extract quantitative values of the magnetic field B in the xy-plane (i.e., 65 and 22 mT at 25 and 50 nm away from the tip apex respectively, see also table 4.2) comparing the flux lines obtained from the reconstructed phase map of the tip with the magnetic phase lines of the simulation, as shown in figures 4.8.

However, it was impossible to find a precise simulation that could perfectly fit the reconstructed phase map. This is due to several reasons, for example, because of the

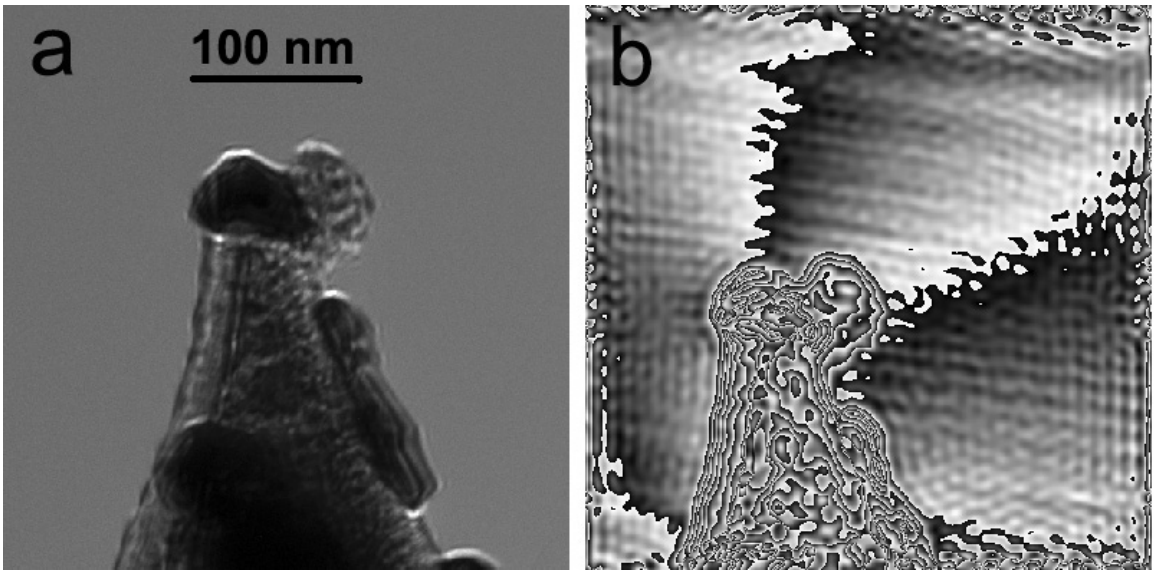

Figure 4.10: High resolution TEM micrograph and the corresponding reconstructed phase map of a MFM tip revealing an asymmetric trend of the flux lines of the magnetic field of the tip in relation to the asymmetric shape of the particles lying on top of the tip.

particular shape of the tip apex (an example is presented in figure 4.10). Apparently, the presence of a second particle and also the particle shape cause a non-symmetric flux leakage. As a result we have not been able to introduce parameters that could take into account these details. As we have observed using high resolution TEM analysis all tips are different from each other so that, each simulation would have to be adapted to the specific case.

It should be pointed out that we could have encountered other problems even if the characterization of the leakage flux of the tip would have been successful using electron holography. The reproducibility of the MFM probe itself is strongly limited, since it is difficult to manipulate a tip on the scale of about ten nanometer. Thus it is not possible to reproduce a particular tip shape and coating. Furthermore, the electron irradiation may change the structure or change the position of the magnetic particles, leading to a modification of the tips magnetic field.

5 Co, Ni, Cu and Au nanowires: determination of the mean inner potential

5.1 Introduction

The volume average of the electrostatic potential of a solid is known as its mean inner potential. This potential is negative and has a value typically between -5 and -30 V, depending on the composition and structure of the solid. The mean inner potential is given by the zero-order Fourier coefficient (V_0) of the crystal potential (for infinitely large perfect crystals), and is usually taken as an arbitrary zero of the potential [156]. However, V_0 has several important meanings [157]. It was shown that V_0 for a crystal depends on sums of dipole and quadrupole moments in the unit cell, and methods were developed for the calculation of V_0 from the mean square radii of the atoms ($< r^2 >$), or from atomic structure factors for X-ray scattering [156]. The dependence on $< r^2 >$ makes V_0 very sensitive to the redistribution of the outer valence electrons due to bonding: V_0 could intuitively be interpreted as a measure of the effective atomic sizes in a crystal.

In practice, V_0 is important in low-energy electron diffraction (LEED), reflected high-energy electron diffraction (RHEED), Fresnel imaging of interfaces and in electron holography, because it increases the effective energy of the electrons in the solid, thereby defining the refraction effect of the transmitted and diffracted beams. Accurate methods for measuring V_0 are therefore of considerable interest.

The large difference between the value of the mean inner potential and the kinetic energy of the incident electrons E ($E \gg V_0$) explains why the refraction effects due to V_0 are usually negligible in transmission electron microscopy of thin specimens. This effect can be translated in an electron-optical index of refraction n, already introduced in 1.2.1.1, (see also [33])

$$n(r) = \frac{\lambda}{\lambda_{\mathrm{m}}} = \frac{p_{\mathrm{m}}}{p} = \left[\frac{2(E-V)E_0 + (E-V)^2}{2EE_0 + E^2}\right]^{1/2}, \tag{5.1}$$

where λ is the wavelength of the electrons in vacuum and λ_{m} is the wavelength of the electrons in the material. The formula can be simplified if it is assumed that $V \ll E$ and E_0

$$n(r) = 1 - \frac{V}{E}\frac{E+E_0}{2E_0+E} + ... \tag{5.2}$$

The refractive index n causes not only the change in the propagation direction of the electron, but also a phase shift of an electron wave transmitted through a material, relative to a coherent reference wave running through vacuum. For this reason, recalling equation 1.7, the phase shift recorded in a hologram due to the refractive index n or, in other words, due to the mean inner potential of the material is given by

$$\phi = \frac{2\pi}{\lambda}\Delta = \frac{2\pi}{\lambda}(n-1)\,t = \frac{2\pi e}{\lambda E}\left(\frac{E_0+E}{2E_0+E}\right)V_0\,t = C_{\mathrm{E}}\,V_0\,t. \tag{5.3}$$

It follows that the phase image of a material with uniform structure and composition represents a map of its projected thickness $t(x,y)$

$$t(x,y) = \frac{\phi(x,y)}{C_{\mathrm{E}}V_0}, \tag{5.4}$$

where C_{E} and V_0 are proportionality factors. Knowing the thickness of the material as a function of x, the mean inner potential of a dense material can be calculated directly from equation 5.4.

In literature there are no extensive tables of experimental values, except for few materials [33, 157, 158]. In addition, the published values for the same material by different

research groups are often further apart than the reported errors (e.g., values ranging from 12.3 V to 16 V have been reported for V_0 of MgO, as summarized by Yada *et al*. [159]). Experimental measurements of V_0 have been based on quantification of refraction effects (electron diffraction methods) and phase changes (electron holography methods).

Electron interferometry was first used by Möllenstedt and Keller [160], and then by other groups [161–164], to measure the mean inner potential of films with known thickness. Amorphous and polycrystalline films of desired nominal thickness have been used, deposited in the shape of strips or disks on electron-transparent substrates. The phase change was measured directly from off-axis electron holograms (interferometric measurements), by recording the shift of a holographic fringe phase at the edge of the film, the distance between adjacent fringes corresponding to a phase change of 2π. The reported statistical accuracy in these studies ranged from 2.5% to 9.5%, although uncertainties in specimen thickness are very likely the sources of systematic errors. A recent work by Wang *et al*. [165] describes the use of transmission electron holography to determine the mean inner potential of spherical nanoparticles of amorphous polystyrene. The aim was to separate the specimen thickness on the phase shift of the incident electron wave from the intrinsic refractive properties of the specimen.

In this research work, electron holography has been employed to determine the mean inner potential V_0 of Cu, Co, Ni, and Au using single component nanowires. From the determination of the phase shift of the electron wave through the sample and deducing the thickness from the image profile of the nanowire, we could get values for the mean inner potential of these materials, and found them to be in agreement with calculated values starting from the structure factors of the corresponding crystals.

This work has been carried out in collaboration with the group of Prof. B. Doudin who kindly provided us with the samples.

5.2 Experimental

Single component nanowires have been fabricated using polycarbonate membranes, made by electrodeposition of Co, Cu, Ag and Nickel into the pores of thin foils (generally 6 μm

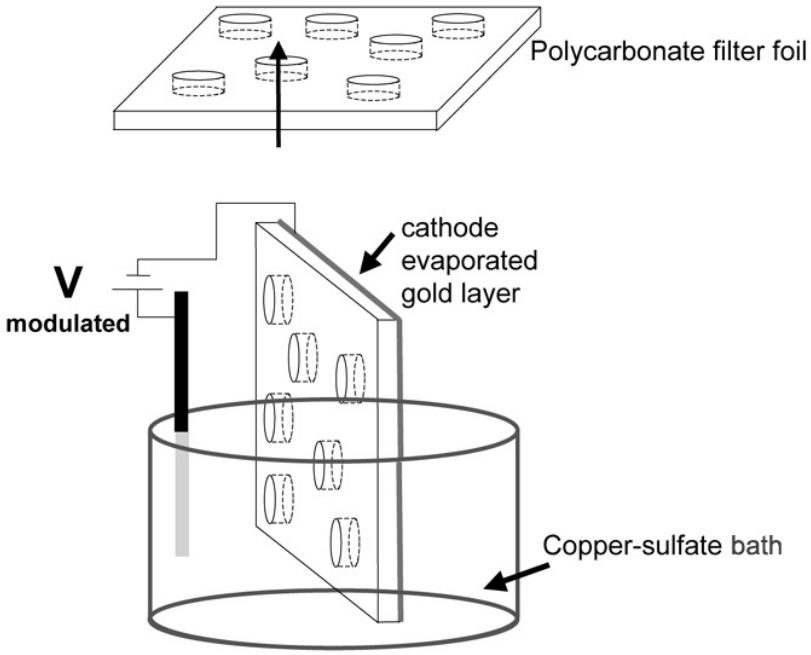

Figure 5.1: Schematic drawing of the formation of a single component nanowire using a track-etched polycarbonate membrane.

thick). These films were irradiated with heavy ions and etched chemically along the fission tracks with irradiation damage. The empty membranes were coated with gold on one side, which served as cathode in an electrolytic bath. The well documented technology of electrodeposition [166, 167] can be directly used to make deposits in the pores.

To prepare nanowires of a single material, for example Co, a single bath which contained only Co has been used : $CoSO_4$ - 7 H_2O 120 g/l, H_3BO_3 45 g/l. A constant potential V_{Co} of 1000 mV was applied in order to deposit Co into the pores. Figure 5.1 illustrates schematically the preparation technique of these nanowires. The potentials were measured with respect to a reference electrode of Ag/AgCl. The deposition rates were deduced from the time to fill the pores, which could be associated with a marked increase in the deposition current [168]. Typical deposition times of 30 s at V_{Co} for membranes 6 μm in thickness have been measured. For the nanowires made with the other materials, the same technique has been used, employing a different bath containing the element that had to be deposited.

The polycarbonate membranes were dissolved in CH_2Cl_2 and subsequently, the resulting nanowires were dispersed in ethanol. For the electron holography investigations, a few drops of the solution were poured onto copper grids, coated with a thin amorphous carbon foil .

5.3 Electron holography characterization

Since, holography can be used to directly determine the mean inner potential of a material, provided that the thickness of the specimen is known, we have employed this technique for Co, Ni, Cu and Au nanowires. Figure 5.2a shows a typical hologram of a Cu nanowire. The reconstructed phase map is presented in figure 5.2b. Another example is given in figure 5.3 for a Co nanowire.

We assumed that the nanowires have a circular cross section and we used the diameter to determine the thickness of the nanowires. The profile, displayed in figure 5.3c, shows the phase shift as a function of the position along the image plane (the asymmetric trend of the curve is related to the slight phase shift due to the weak magnetic leakage field of the Co nanowire). We measured from the TEM image, at the position indicated on the reconstructed phase map of figure 5.3b, a thickness of 25.9 ± 0.4 nm for the nanowire. The error arises from the uncertainty of the detection of the border of the nanowire and from the pixel size of the image. Knowing the thickness of the nanowire and the phase shift through it, we could then apply equation 5.4 to calculate the mean inner potential. An example of values of V_0 deduced from a Co nanowire is reported in table 5.1.

Table 5.2 shows the values of the mean inner potential for the four kind of nanowires that we have analyzed. The experimental V_0 is the average of the values determined experimentally. These values have been obtained averaging over a set of values of the mean inner potential calculated at different points of the same nanowire (an example is reported in table 5.1). The table also lists the value of the mean inner potential calculated from the structure factor of the material. The values are in good agreement with those calculated using the theory, even if we notice that the experimental value of V_0 in the case

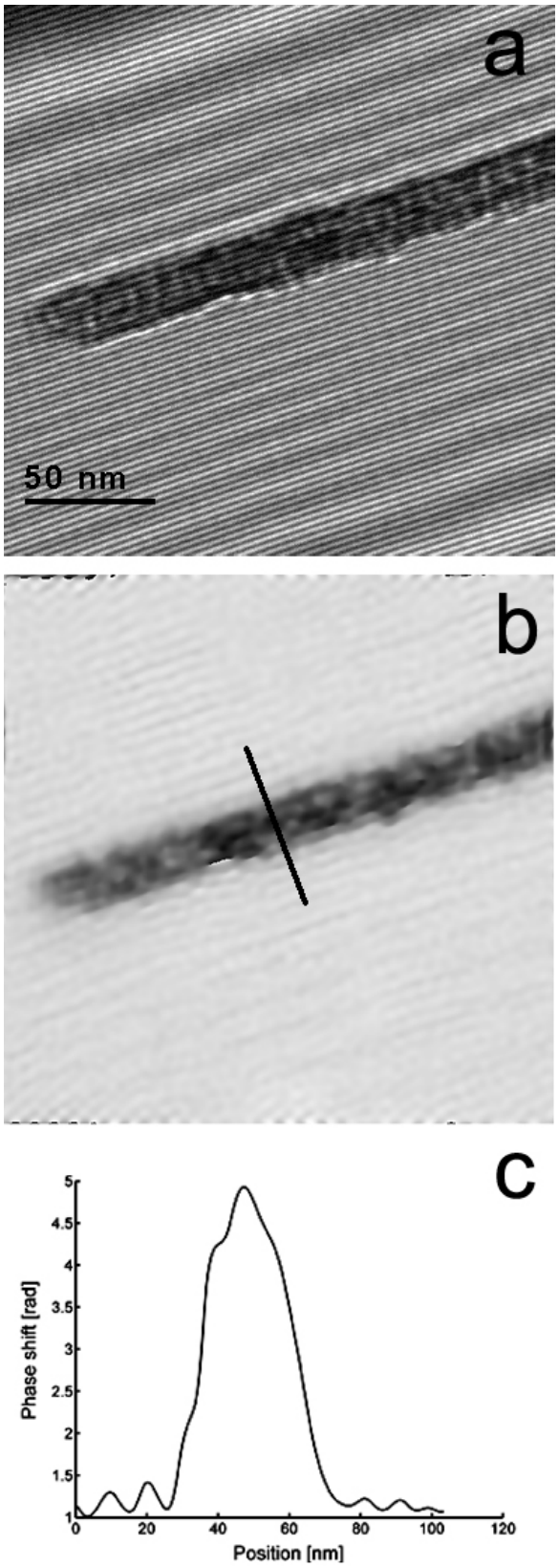

Figure 5.2: (a) Hologram of a Cu nanowire. (b) Reconstructed phase map and (c) line plot of the phase shift along the line indicated in (b).

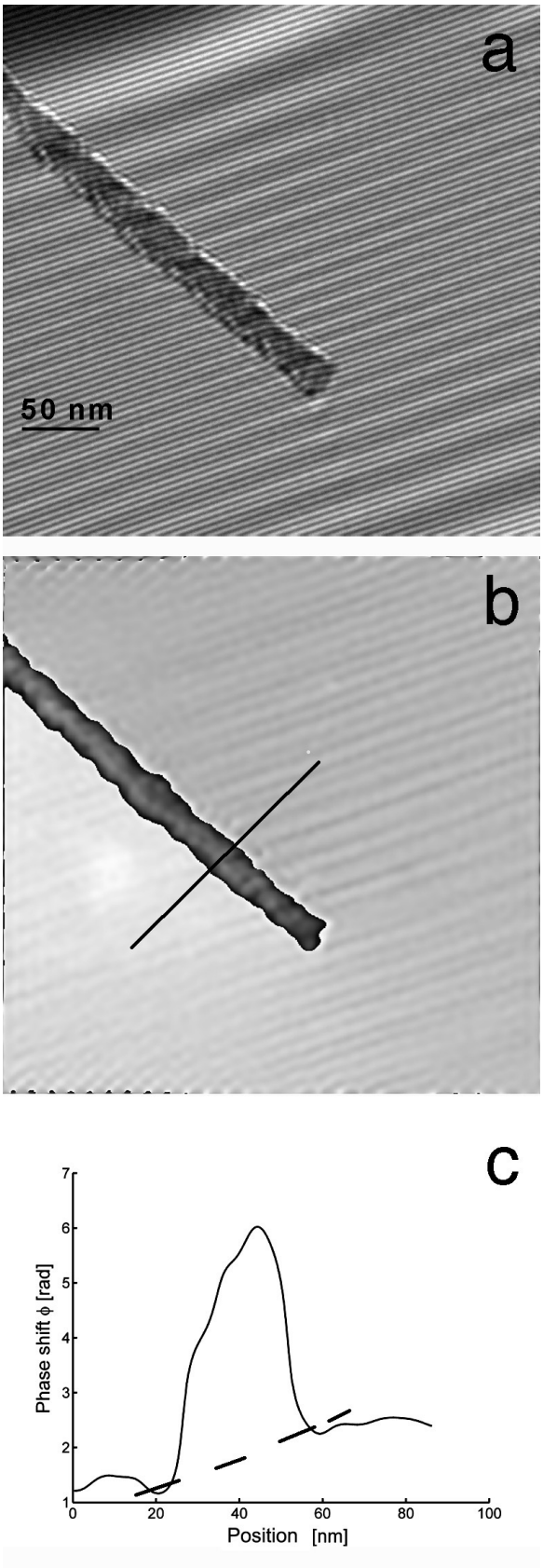

Figure 5.3: (a) Hologram of a Co nanowire. (b) Reconstructed phase map and (c) line plot of the phase shift along the line indicated in (b). The dashed line in (c) indicates the phase offset caused by the presence of the magnetic flux of the Co nanowire.

of Ni is lower than expected (we will discuss below the reasons why this result is inferred). The values reported are determined by applying the atomic scattering factors by Weickenmeier-Kohl (W-K) and Doyle-Turner (D-T), using the software JEMS established by Prof. P. Stadelmann [135].

Some theoretical remarks A general expression for the mean inner potential stems from its definition as a volume average of the atomic electrostatic potentials within the material

$$V_0 = \frac{1}{\Omega} \cdot \int_{\Omega} V(\vec{r}) d\vec{r} \tag{5.5}$$

Table 5.1: Mean inner potential of Co obtained from the phase shift ϕ and thickness t deduced from different points of the same nanowire.

ϕ (rad) $\pm$ 0.4	t (nm) $\pm$ 0.25	V_0 (V)
4.4	25.96	24.22 $\pm$ 1.43
4.12	25.91	24.38 $\pm$ 1.43
4.05	24.45	25.4 $\pm$ 1.52
4.32	24.48	27.06 $\pm$ 1.51
3.77	20.71	27.91 $\pm$ 1.78

Table 5.2: Mean inner potential of Co, Cu, Au and Ni calculated from the reconstructed phase map, using atomic scattering factors by Weickenmeier-Kohl (W-K) and Doyle-Turner (D-T). This values were obtained using the software JEMS [135].

	Co	Cu	Au	Ni
experimental	25.8 $\pm$ 1.5 V	20.1 $\pm$ 0.93 V	26.9 $\pm$ 1.36 V	21.4 $\pm$ 1.74 V
W-K	26.07	19.43	25.97	24.86
D-T/S-B	25.83	19.91	26.28	25.20

where Ω is the volume of the unit cell for a crystalline solid, or the volume of the material for a disordered solid. In principle, V_0 could be calculated from equation 5.5 for any material for which $V(\vec{r})$ is known throughout the unit cell, or throughout a given volume. Unfortunately this information is not always available and approximations should be done. The simplest approximation employed to estimate V_0 is to treat the solid as if were made of an array of neutral free atoms. In this non-binding approximation (considering for neutral atom that $V(\vec{r}) \sim \sum_i V(\vec{r} - \vec{R}_\mathrm{i})$) equation 5.5 becomes

$$\begin{aligned} V_0 &= \lim_{q\to 0} \frac{1}{\Omega} \int V(\vec{r}) e^{i\vec{q}\vec{r}} d^3r \\ &\simeq \sum_\mathrm{i} \lim_{q\to 0} \frac{1}{\Omega} \int V(\vec{r} - \vec{R}_\mathrm{i}) e^{i\vec{q}\vec{r}} d^3r \\ &= \sum_\mathrm{i} \left\{ \lim_{q\to 0} \frac{1}{\Omega} \int V(\vec{r} - \vec{R}_\mathrm{i}) e^{i\vec{q}\vec{r}} d^3(\vec{r} - \vec{R}_\mathrm{i}) \right\} \\ &= \sum_i f_\mathrm{i}(0) \end{aligned} \tag{5.6}$$

where $f_i(0)$ are the atomic scattering amplitudes for forward scattering of electrons. The summing of $f_i(0)$ is performed over the i atoms in the unit cell.

The calculations by Doyle and Turner for the atomic scattering amplitudes were based on the relativistic Hartree-Fock atomic wave functions. For high energy electrons, the atomic scattering amplitudes need to be multiplied by the relativistic factor γ equal to $m/m_0 = [1-(v/c)^2]^{-1/2}$, where v is the speed of the electron in vacuum and c is the speed of light in vacuum. In our case, we worked with 300 keV electrons that have a ratio $m/m_0 = 0.6305$, giving a relativistically corrected value of V_0 shown in table 5.2. Actually this is a limitation of the non-binding approximation for calculating the mean inner potential of a solid. From the definition given in equation 5.5, the mean inner potential is a property of the solid and not of the electrons that are used to probe the solid. This is particularly true for high energy electrons when the exchange and correlation contributions of the incident electrons to the potential of the solid $V(\vec{r})$ are negligible [169]. In this limit, the mean inner potential should indeed be a constant which is independent of the energy of the incident electrons. Within the limits of low energy electrons ($E < 100$ eV), when the exchange and correlation effect can not be ignored, the mean inner potential is expected to vary with the energy of the incident electrons [170–172].

As already mentioned above, the uncertainty on the thickness t of the sample is a source of systematic errors on the calculation of V_0. Looking at the high resolution micrograph of the nanowires, figure 5.4a, 5.5a and 5.6a, we see that the nanowire have generally very rough contours. In practice, we are not able to see if the nanowire is cylindric or oblate, a characteristic that could affect systematically the measurement of the thickness. To have more information about the shape of the nanowires, we made some tests by electron energy-loss spectroscopy (EELS) on selected nanowires in order to record thickness maps of the nanowires.

What we really measure by EELS is the strength of multiple inelastic scattering events that take place in the sample that is given by the ratio

$$I_{in}/I_0 = (1 - e^{-t/\lambda})/e^{-t/\lambda} \tag{5.7}$$

where λ is the mean free path of all inelastic collisions resulting in an energy loss of 3 eV or greater and a scattering angle smaller than the collection angle. In the limit of very thin sample, equation 5.7 become

$$I_{in}/I_0 = t/\lambda. \tag{5.8}$$

Therefore, I_{in}/I_0 provides a map reflecting the relative thickness changes of the specimen [173].

Three examples are reported in figures 5.4b, 5.5b and 5.6b. A profile line, figures 5.4c, 5.5c and 5.6c, taken at the point indicated in figures b respectively, shows that the nanowires are cylindrical (figure 5.4a) or occasionally oblate (5.5c), or in other cases (e.g. figure 5.6c) we have observed that the nanowires have holes or concavities. The thickness of the nanowire, determined from the projected image of the wire itself, overestimates the real value, and therefore, the value of the mean inner potential will result in a lower value than for example calculated from atomic scattering factors.

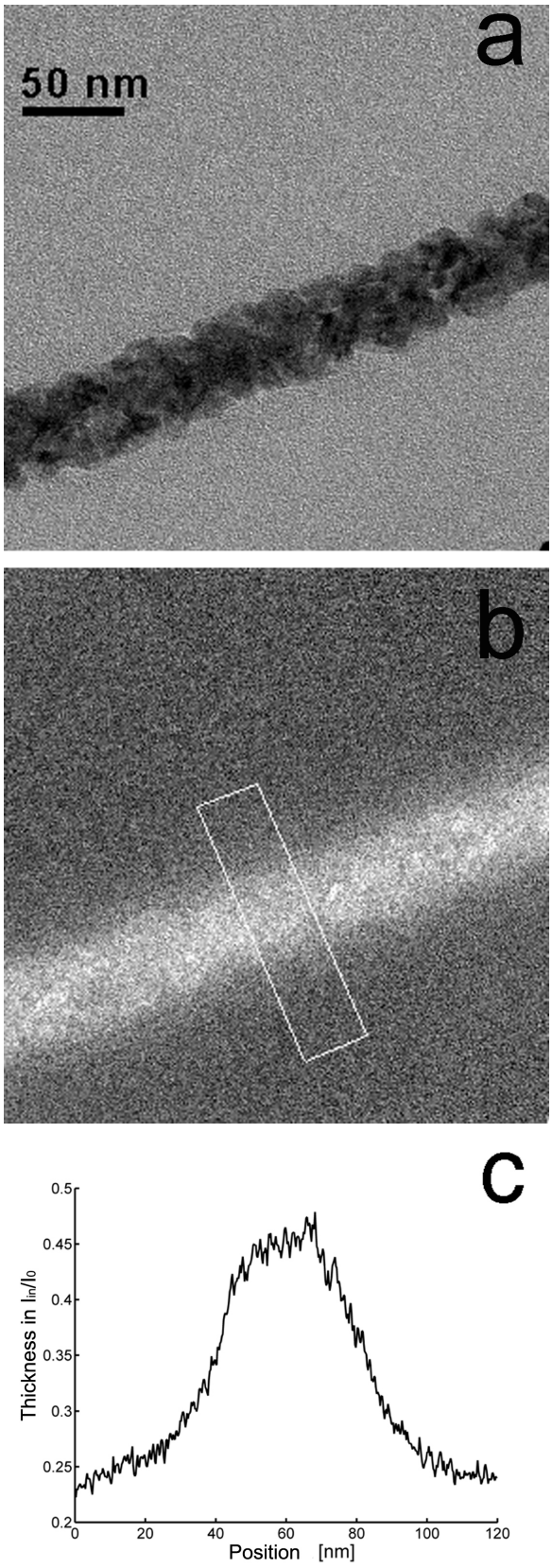

Figure 5.4: (a) High resolution TEM micrograph, (b) EELS thickness map and (c) line plot of the qualitative thickness variation of a selected nanowire, which suggests an approximately circular cross section.

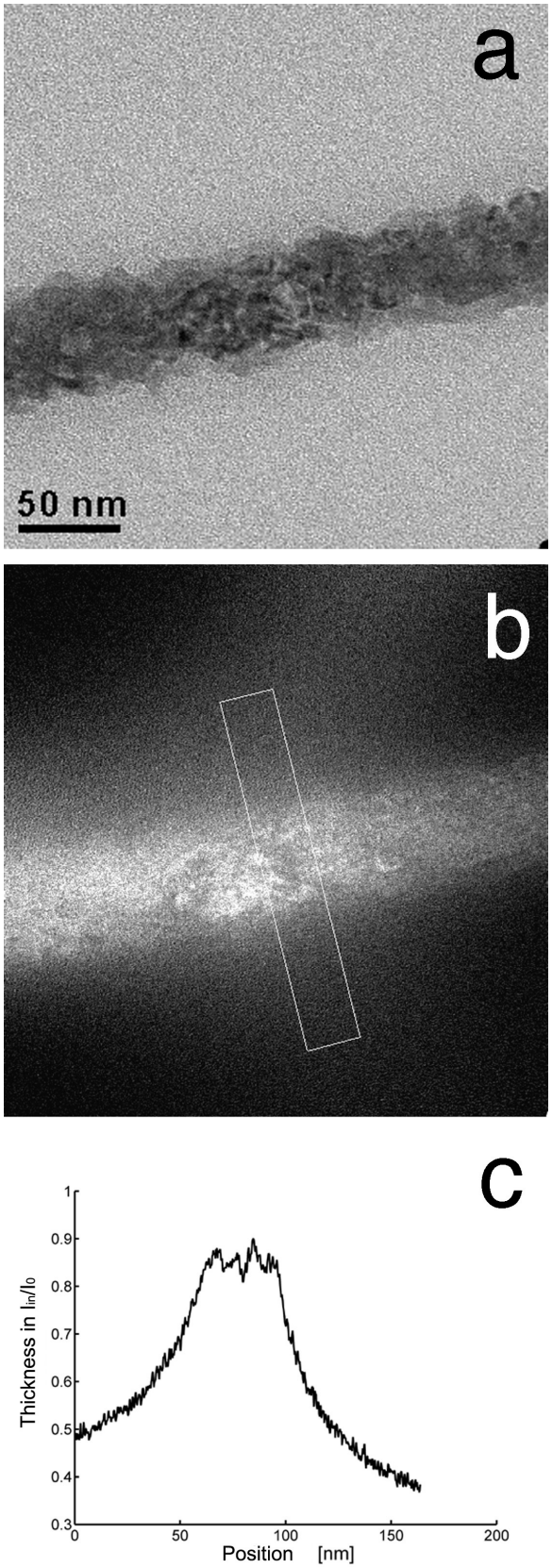

Figure 5.5: (a) High resolution TEM micrograph, (b) EELS thickness map and (c) line plot of the qualitative thickness variation of a selected nanowire, suggesting, from the flat cross section, that the nanowire has an oblate profile.

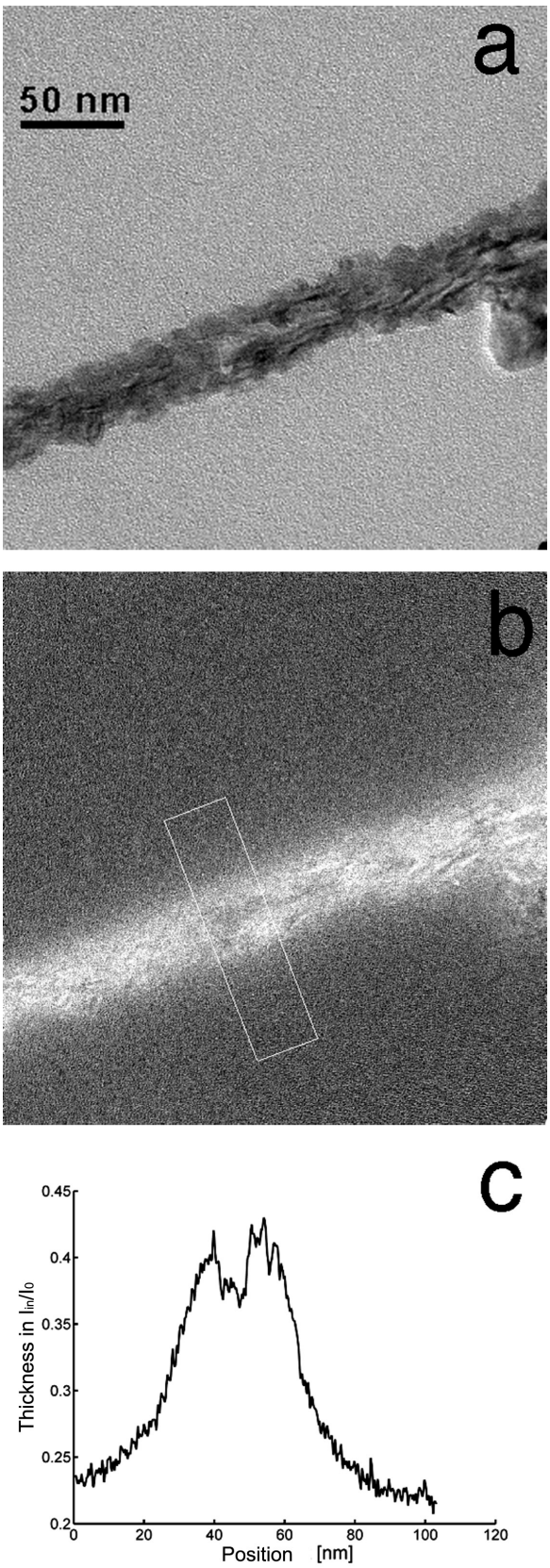

Figure 5.6: (a) High resolution TEM micrograph, (b) EELS thickness map and (c) line plot of the qualitative thickness variation of a selected nanowire, suggesting, from the very irregular cross section, that the nanowire presents holes or concavities.

5.4 Conclusions

In this chapter we presented results of measurement of the mean inner potential of a few materials (Co, Cu. Ni and Au) using single component nanowires. This work has been an attempt to test electron holography and its reliability for the measurements of this quantity, that is fundamental in electron holography as well as in other techniques dealing with low energy and high energy electrons (LEED, RHEED). Therefore, accurate methods for measuring the mean inner potential are of importance also for a further interpretation of the collected images. When the mean inner potential of the material is known, the phase image becomes a quantitative map of the projected thickness. This property is the basis for the application of electron holography to study surface topographies and shapes of nanoparticles. For example, we have used the knowledge of this quantity (from literature) to better analyze the stray field of nanophase gas condensed Fe particles illustrated in Chapter 3.

When determining the mean inner potential of the selected materials, we have encountered some problems related to the determination of the thickness of the nanowires. We initially assumed that the nanowires were circular in cross section. After a additional analysis of the nanowires by electron energy-loss spectroscopy (EELS), we realized that they were characterized by differing profiles. Besides having a quite rough surface, in most places the nanowires were oblate. Furthermore, some holes were occasionally present. Such discontinuities were affecting the calculated value of the mean inner potential, yielding a lower result than the one expected from the theory.

In principle, it is possible to use one of the standard methods for measurements of specimen thickness, such as EELS, convergent beam electron diffraction, or thickness fringes. But these methods require a priori knowledge of specimen composition and/or structure and therefore, they become particularly involved if a thickness map is desired rather than measurement at a few discrete points.

In general, we found values of the mean inner potential using electron holography that are in good agreement with the values calculated from the atomic scattering factors using the software JEMS.

Summary

With the application of the electron holography technique to multiple types of samples and materials, we have demonstrated its versatility and efficiency for studying magnetic fields and electrostatic mean inner potentials in nanostructured materials.

First, we have applied electron holography to study the *in-situ* thermal evolution of the magnetization of micromagnetic Fe particles prepared by mechanical alloying, with grains on the nanometer scale. Considering the Random Anisotropy Model (RAM), we have been able to establish a direct relationship between the variation with temperature of the stray field and the structural evolution inside the particle.

Second, the interpretation of electron holography results on Fe nanoparticles, with size comparable to the characteristic domain-wall thickness as produced by gas-phase condensation, has been made possible in light of structural and magnetic characterization of similar systems. This has indicated the existence of flux-closure magnetic configurations inside the particles. The reconstructed magnetic phase maps are consistent with the presence of low-remanence vortex states of the magnetization.

Third, as a practical application of this technique, we employed electron holography to investigate the magnetic flux leaking out from magnetic force microscope tips in order to extract quantitative information on their B-field. This allowed us to distinguish between good and bad tips, contributing therefore to the improvement of the resolution of the MFM technique.

Finally, single component nanowires of few materials (Au, Co, Cu, Ni) have been analyzed to study their electrostatic potential. New results on the evaluation of the mean

inner potential of these materials have been made available from the reconstructed phase maps.

During our work we have encountered some limitations of the electron holography technique, the most important being related to the sample preparation. Sample should be thinner than 100 nm and clean in order to generate an insight on the interior magnetic configuration of the sample. Additionally, in most cases holography should be performed at an edge of the sample (in order to compare the object wave with the unperturbed reference wave) thus increasing the effort of the preparation and limiting the usable part of the sample. Finally, a further limitation is introduced by the noise that comes from the thin amorphous carbon foil used as support of the specimen. Therefore, the recorded holograms contain a considerable background noise (corresponding to a phase shift of 3% of h/e on 2π).

Appendix

The Random Anisotropy Model for nanocrystalline materials

The magnetic properties of an assembly of small grains depend strongly on the interplay of local magnetic anisotropy energy and ferromagnetic exchange energy.

For large grains the magnetization can follow the easy magnetic directions in the single grains and domains can be formed within the grains. The magnetization process, thus, is determined by the magneto-crystalline anisotropy K_1 of the crystallites [62].

For very small grains, however, ferromagnetic exchange interaction forces the magnetic moments more and more to align parallel, thus, prohibiting the magnetization from following the easy directions of each individual grain. As a consequence the effective anisotropy for the magnetic behavior is an average over several grains and, thus, reduced in magnitude.

The dividing line between these two cases is given by the ferromagnetic exchange length

$$L_{\mathrm{ex}}^{0} = \sqrt{A/K_1} \tag{9}$$

(A denotes the exchange stiffness) which is a basic parameter in domain wall theory [174] representing a characteristic minimum scale over which the magnetization can vary appreciably.

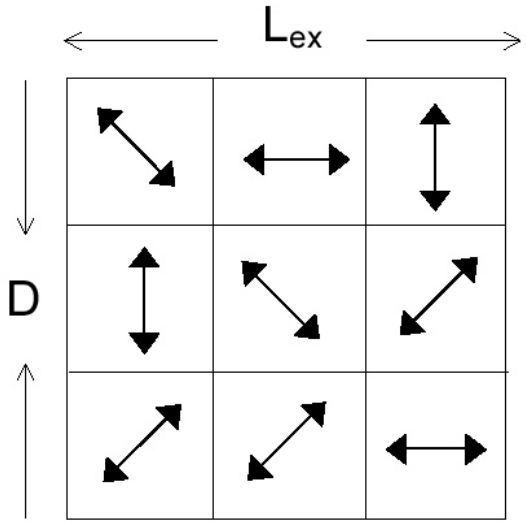

Figure 7: Schematic representation of the random anisotropy model. The arrow indicate the randomly fluctuating magneto-crystalline anisotropies

In order to interpret the behavior of the magnetic properties for very small grain sizes, Herzer makes use of the random anisotropy model originally proposed by Alben *et al*. [77] for amorphous ferromagnets. The basic idea is sketched in figure 7 and starts from an assembly of ferrimagnetically coupled grains of size D with magneto-crystalline anisotropies K_1 oriented at random.

The effective anisotropy affecting the magnetization process results from averaging over the $N = (L_{ex}/D)^3$ grains within the volume $V = L_{ex}^3$ of the exchange length. For a finite number of grains N there will always be some easiest direction determined by statistical fluctuations. As a consequence the resulting anisotropy density $< K >$ is determined by the mean fluctuation amplitude of the anisotropy energy of the N grains, i.e.,

$$< K > \approx \frac{K_1}{\sqrt{N}} = K_1 \left(\frac{D}{L_{\mathrm{ex}}} \right)^{3/2} \tag{10}$$

In turn the exchange length L_{ex} now is related self-consistently to the average anisotropy by substituting $< K >$ for K_1 in eq. 9, i.e.

$$L_{\mathrm{ex}} = \sqrt{\frac{A}{< K >}}. \tag{11}$$

This renormalization of L_{ex} results from the interplay of anisotropy and exchange energies: as magneto-crystalline anisotropy is suppressed by exchange interaction the scale on which exchange interactions dominate expands at the same time, thus, the local anisotropies are averaged out even more effectively.

The combination of equations 10 and 11 finally yields

$$< K > \approx \frac{K_1^4}{A^3} \cdot D^6 \tag{12}$$

$$L^* \approx \frac{A^2}{K^2 D^3} \tag{13}$$

which holds as long as the grain size D is smaller than the exchange length L_{ex}. It should be noted that this result is essentially based on statistical and scaling arguments and is not limited to the case of uniaxial anisotropies (as might be anticipated from figure 7) but also holds for cubic or other symmetries.

The most significant feature of the above analysis is the strong variation of $< K >$ with the sixth power D^6 of the grain size. If the coercivity and initial permeability are related to $< K >$ using the results for coherent spin rotation we find

$$H_C = p_C \frac{< K >}{J_S} \approx p_C \frac{K_1^4 \cdot D^6}{J_S \cdot A^3}. \tag{14}$$

The Herzer model discussed so far presumes that the randomly oriented grains are perfectly coupled via the exchange interaction.

Hernando et al have generalized the model for the case of two phase nanocrystalline material composed of an assembly of crystallites embedded in a ferromagnetic matrix. According to their model, the crystallites are expected to be coupled by the exchange interaction when their dimension is smaller than the ferromagnetic exchange length of the grain and their distance is smaller than the ferromagnetic exchange length of the matrix (L_m). If the latter condition does not hold, the grains are uncoupled with respect to the exchange interaction [63].

Bibliography

[1] R. O'Handley, in *Modern magnetic Material: principles and applications*, edited by D. MacAdam (John Wiley, New York, 2000), p. 432.

[2] J. Chapmann and M. Scheinfein, J. Magn. Magn. Mater. **200**, 729 (1999).

[3] E. D. Dahlberg and R. Proksch, J. Magn. Magn. Mater. **200**, 720 (1999).

[4] M. Hale, H. Fuller, and H. Rubistein, J. Appl. Phys. **30**, 789 (1959).

[5] H. Lichte, in *Advances in Optical and Electron Microscopy*, edited by T. Mulvey and C. Sheppard (Academic Press, New York, 1991), Vol. 12, p. 25.

[6] A. Tonomura, *Electron Holography* (Springer-Verlag, Heidelberg, 1993), Vol. 70 of Springer Series in Optical Science.

[7] D. Gabor, Nature **161**, 777 (1948).

[8] H. Lichte, Optik **70**, 16 (1985).

[9] H. Lichte, Ultramicroscopy **20**, 293 (1996).

[10] E. Völkl and H. Lichte, Ultramicroscopy **32**, 177 (1990).

[11] K. Brand, C. Guo, M. Lehmann, and H. Lichte, Proc. Conf. Microscopy and Microanalysis **1**, 284 (2001).

[12] J. Cowley, Ultramicroscopy **41**, 335 (1992).

[13] G. Möllensted and H. Düker, Naturwissenschaften **42**, 41 (1955).

[14] A. Tonomura, Rev. Mod. Phys. **59**, 639 (1987).

[15] W. de Ruijter and J. Weiss, Ultramicroscopy **50**, 269 (1993).

[16] D. Smith and M. McCartney, in *Introduction to Electron Holography*, edited by E. Voelkl, L. Allard, and D. Joy (Kluwer Academic, New York, 1999), p. 87.

[17] S. Frabboni, G. Matteucci, G. Pozzi, and M. Vanzi, Phys. Rev. Lett. **55**, 2196 (1985).

[18] B. Frost, L. Allard, E. Völkl, and D. Joy, *Electron Holography* (Elsevier, Amsterdam, 1995), p. 169.

[19] M. McCartney and M. Gajadardziska-Josifovska, Ultramicroscopy **53**, 283 (1994).

[20] W. Rau, P. Schwander, F. Baumann, W. Hoppner, and A. Ourmazdd, Phys. Rev. Lett. **82**, 2614 (1999).

[21] V. Ravikumar, R. Rodrigues, and V. Dravid, Phys. Rev. Lett. **75**, 4063 (1995).

[22] N. Osakabe, K. Yoshiba, Y. Horiuchi, T. Matsuda, H. Tanabe, T. Okuwaki, J. Endo, H. Fujiwara, and A. Tonomura, Appl. Phys. Lett. **42**, 792 (1983).

[23] A. Tonomura, N. Osakabe, T. Matsuda, T. Kawasaki, J. Endo, and H. Yamada, Phys. Rev. Lett. **56**, 792 (1986).

[24] J. Bonevich, K. Harada, T. Matsuda, H. Kasai, T. Yoshiba, G. Pozzi, and A. Tonomura, Phys. Rev. Lett. **70**, 2952 (1993).

[25] J. Chapmann, R. Ferrier, L. Heyderman, S. McVitie, W. Nicholson, and B. Bormans, *Micromagnetics, Microstructures and Microscopy* (Adam Hilger, Bristol, 1993), Vol. 138, p. 1.

[26] G. Ade, Adv. Electron. Electr. Phys. **89**, 1 (1994).

[27] H. Lichte, Ultramicroscopy **51**, 15 (1993).

[28] W. de Ruijter, Micron **26 (3)**, 247 (1995).

[29] L. Reimer, in *Transmission Electron Microscopy*, edited by D. MacAdam (Springer, Berlin, 1989), p. Chapter 6.

[30] E. Völkl, L. Allard, and B. Frost, J. Microscopy **180**, 39 (1995).

[31] J. Bonevich, HolograFREE, software located at 'http://metallurgy.nist.gov/webpages/JEBonevich/' , 2003.

[32] J. Cowley and J. Spence, in *Introduction to Electron Holography*, edited by E. Voelkl, L. Allard, and D. Joy (Kluwer Academic, New York, 1999), p. 17.

[33] L. Reimer, in *Transmission Electron Microscopy*, edited by D. MacAdam (Springer, Berlin, 1989), p. 57.

[34] G. Missiroli, G. Pozzi, and U. Valdré, J. Phys. E **14**, 649 (1981).

[35] B. Frost and G. Matteucci, in *Introduction to Electron Holography*, edited by E. Voelkl, L. Allard, and D. Joy (Kluwer Academic, New York, 1999), p. 183.

[36] H. Boersch and H. Raith, Naturwissenschaften **20**, 574 (1959).

[37] J. Chapman, J. Phys. D **17**, 623 (1984).

[38] C. Beeli, Image taken from the lecture on "Electron Microscopy" held by Dr. C. Beeli and Dr. H. Heinrich, 2002.

[39] J. Chapman, G. Morrison, J. Jakubovics, and R. Taylor, *Electron Microscopy and Analysis, 1983, IOP Conf. Ser. No. 68* (P. Doig Edition, -, 1984), p. 197.

[40] J. Chapman, A. Johnston, L. Heyderman, S. McVitie, W. Nicholson, and B. Bormans, IEEE Trans. Magn. **30**, 4479 (1994).

[41] A. Johnston and J. Chapman, J. Microsc. **179**, 119 (1995).

[42] N. Dekkers and H. de Lang, Optik **41**, 452 (1974).

[43] H. Rose, Ultramicroscopy **2**, 251 (1977).

[44] G. Morrison, H. Gong, J. Chapman, and V. Hrnciar, J. Appl. Phys. **64**, 1388 (1988).

[45] J. Unguris, D. Pierce, A. Galejs, and R. Celotta, Phys. Rev. Lett. **49**, 72 (1982).

[46] J. Unguris, G. Hembree, R. Celotta, and D. Pierce, J. Microscopy **139**, RP1 (1985).

[47] K. Koike and K. Hayakaawa, Jpn. J. Appl. Phys. **23**, L187 (1984).

[48] G. Hembree, J. Unguris, R. Celotta, and D. Pierce, Scanning Microsc. (Suppl.) **1**, 229 (1987).

[49] K. Koike, H. Matsuyama, and K. Hayakaawa, Scanning Microsc. (Suppl.) **1**, 241 (1987).

[50] H. Oepen and J. Kirschner, Scanning Microsc. **5**, 1 (1991).

[51] J. Unguris, M. Scheinfein, D. Pierce, and R. Celotta, Appl. Phys. Lett. **55**, 2553 (1989).

[52] I. Tomas, H. Niedoba, M. Ruhrig, and G. Wittmann, Phys. Stat. Sol. (a) **131**, 201 (1992).

[53] A. Hubert and R. Schäfer, *Magnetic Domains* (Springer Verlag, Berlin, 1998).

[54] P. Grütter, D. Rugar, H. Mamin, G. Castillo, S. Lambert, C.-J. Lin, R. Valletta, O. Walter, T. Bayer, and J. Greschner, Appl. Phys. Lett. **57**, 1820 (1990).

[55] W. Rave, L. Billard, M. Labrune, A. Thiaville, and J. Miltat, IEEE Trans. Magn. **30**, 4473 (1994).

[56] P. Grütter, A. Wadas, E. Meyer, H. Heinzelmann, H.-R. Hidber, and H.-J. Güntherodt, J. Vac. Sci. Technol. **A 8**, 406 (1990).

[57] H. Mamin, D. Rugar, J. Stern, R. F. Jr., and P. Kasiraj, Appl. Phys. Lett. **55**, 318 (1989).

[58] M. Schneider, st. Müller-Pfeiffer, and W. Zinn, J. Appl. Phys. **79**, 8578 (1996).

[59] R. Proksch, S. Foss, and E. Dahlberg, IEEE Trans. Magn. **30**, 4467 (1994).

[60] H. Gleiter, Nanostructured Mater. **6**, 747 (1995).

[61] R. Siegel, in *Foundamental Properties of Nanostructured Materials D*, edited by D. Fiorani and G. Sberveglieri (Word Scientific, London, 1993), pp. 3–20.

[62] G. Herzer, IEEE Trans. Magn. **26**, 1397 (1990).

[63] J. Arcas, A. Hernando, J. Barandirán, C. Prados, M. Vázquez, P. Marín, and A. Neuweiler, Phys. Rev. B **58**, 5193 (1998).

[64] E. Bonetti, L. D. Bianco, D. Fiorani, D. Rinaldi, R. Caciuffo, and A. Hernando, Phys. Rev, Lett. **83**, 2829 (1999).

[65] B. Cullity, *Introduction to Magnetic Materials* (Addison-Wesley, London, 1972), p. 263.

[66] R. Schäfer, H. Hubert, and G. Herzer, J. Appl. Phys. **69**, 5325 (1991).

[67] C. Koch, Nanostruct. Mater. **2**, 109 (1993).

[68] A. Tschöpe and R. Birringer, J. Appl. Phys. **71**, 5391 (1992).

[69] H. Fecht, Nanostruct. Mater. **6**, 33 (1995).

[70] B. Warren, *X-Ray Diffraction* (Dover, Cambridge, 1990).

[71] S. Fagherazzi, A. Benedetti, and S. Polizzi, J. Appl. Cryst. **21**, 536 (1988).

[72] E. Völkl and L. Allard, Microscopy **180**, 39 (1995).

[73] L. D. Bianco, A. Hermando, E. Bonetti, and C. Ballesteros, Phys. Rev. B **59**, 14788 (1999).

[74] T. Malow and C. Koch, Acta Mater. **45**, 2177 (1997).

[75] H. Fecht and C. Moelle, Mater. Res. Soc. Symp. Proc. **457**, 113 (1997).

[76] H. Kronmüller, Nanostruct. Mater. **6**, 157 (1995).

[77] R. Alben, J. Becker, and M. Chi, J. Appl. Phys. **49**, 1653 (1990).

[78] A. Hubert and R. Schäfer, *Magnetic Domains* (Springer Verlag, Berlin, 1998), p. 168.

[79] D. Martin, Proc. Phys. Soc. B **70**, 77 (1957).

[80] A. Hubert and M. Rührig, J. Appl. Phys. **69**, 6072 (1991).

[81] E. Bonetti, E. Campari, L. Pasquini, and E. Sampaolesi, J. Appl. Phys. **84**, 4219 (1998).

[82] *Magnetic Properties of Fine Particles*, edited by J. Dormann and D. Fiorani (Springer, North-Holland, Amsterdam, 1992).

[83] C. Chien, J. Xiao, and J. S. Jiang, J. Appl. Phys. **30**, 120S (1959).

[84] J. L. Dormann, D. Fiorani, and E. Tronc, Adv. Chem. Phys. **98**, 283 (1997).

[85] J. L. Dormann, F. D'Orazio, F. Lucari, E. Tronc, P. Prené, J. Jolivet, D. Fiorani, R. Cherkaoui, and M. Nogues, Phys. Rev. B **53**, 14291 (1996).

[86] H. Mamiya, I. Nakatani, and T. Furubayashi, Phys. Rev. Lett. **80**, 177 (1998).

[87] T. Jonsson, P. Svedlindh, and M. Hansen, Phys. Rev. Lett. **81**, 3976 (1998).

[88] G. Hadjipanayis, in *Science and Technology of Nanostructured Magnetic Materials*, edited by G. Hadjipanayis and G. P. Eds. (Plenum, New York, 1991), pp. 607–626.

[89] Y. Yoshizawa, S. Oguma, and K. Yamauchi, J. Appl. Phys. **64**, 6044 (1998).

[90] E. Bonetti, E. Campari, L. Pasquini, E. Sampaolesi, and G. Scipione, Nanostruct. Mater. **12**, 891 (1999).

[91] A. Berkowitz, J. Mitchell, M. Carey, A. Young, S. Zhang, F. Spada, F. Parker, A. Hutten, and G. Thomas, Phys. Rev. Lett. **68**, 3745 (1992).

[92] P. Allia, M. Knobel, P. Tiberto, and F. Vinai, Phys. Rev. B **52**, 15398 (1995).

[93] R. Kodama, A. Berkowitz, E. McNiff, and S. Foner, Phys. Rev. Lett. **77**, 394 (1996).

[94] B. Martinez, X. Obradors, L. Balcells, A. Rouanet, and C. Monty, Phys. Rev. Lett. **80**, 181 (1998).

[95] E. Tronc, A. Ezzir, R. Cherkaoui, C. Chanéac, M. Noguès, H. Kachkachi, D. Fiorani, A. Testa, J. Grenèche, and J. Jolivet, J. Magn. Magn. Mater. **63**, 221 (2000).

[96] S. Chou, P. Krauss, and L. Kong, J. Appl. Phys. **79**, 6101 (1996).

[97] S. Sun and C. Murray, J. Appl. Phys. **85**, 4325 (1999).

[98] S. Sun, C. Murray, D. Weller, L. Folks, and A. Moser, Science **287**, 1989 (2000).

[99] C. Dennis, R. Borges, L. Buda, U. Ebels, J. Gregg, M. Hehn, E. Jouguelet, K. Ounadjela, I. Petej, I. Prejbeanu, and M. Thornton, J. Phys.: Condens. Matter **14**, R1175 (2002).

[100] W. Rave, K. Fabian, and A. Hubert, J. Magn. Magn. Mater. **190**, 332 (1998).

[101] D. Altbir, P. Vargas, and J. d'Albuquerque e Castro, Phy. Rev. B **64**, 012410 (2001).

[102] N. Usov, L. Kurkina, and J. Tucker, J. Appl. Phys. **35**, 2081 (2002).

[103] W. Wernsdorfer, K. Hasselbach, A. Sulpice, A. Benoit, J. Wegrowe, L. Thomas, B. Barbara, and D. Mailly, Phys. Rev. B **53**, 3341 (1996).

[104] R. Cowburn, D. Koltsov, A. Adeyeye, M. Welland, and D. Tricker, Phys. Rev. Lett. **83**, 1042 (1999).

[105] C. Ross, M. Farhoud, M. Hwang, H. Smith, M. Redjdal, and F. Humphrey, J. Appl. Phys. **89**, 1310 (2001).

[106] T. Shinjo, T. Okuno, R. Hassdorf, K. Shigeto, and T. Ono, Science **289**, 930 (2000).

[107] M. Natali, I. Prejbeanu, A. Lebib, L. Buda, K. Ounadjela, and Y. Chen, Phys. Rev. Lett. **88**, 157203 (2002).

[108] A. Fernandez and C. J. Cerjan, J. Appl. Phys. **87**, 1395 (2000).

[109] C. Stamm, F. Marty, A. Vaterlaus, V. Weich, S. Egger, U. Maier, U. Ramsperger, H. Fuhrmann, and D. Pescia, Science **282**, 449 (1998).

[110] S. Majetich and Y. Jin, Science **284**, 470 (1999).

[111] G. Matteucci and C. Beeli, J. Magn. Magn. Mater. **196-197**, 920 (1999).

[112] G. Matteucci and C. Beeli, Found. Phys. Lett. **Accepted for publication**, 1 (2003).

[113] C. Beeli, P. Stadelmann, J.-P. Ansermet, and B. Doudin, J. Magn. Magn. Mater. **164**, 77 (1996).

[114] C. Beeli, NanoStructured Material **11**, 697 (1999).

[115] E. Snoeck, R. E. Dunin-Borkowski, F. Dumestre, P. Renaud, C. Amiens, B. Chaudret, and P. Zurcher, Appl. Phys. Lett. **82**, 88 (2003).

[116] R. E. Dunin-Borkowski, M. R. McCartney, B. Kardynal, and D. J. Smith, J. Appl. Phys. **84**, 374 (1998).

[117] S. Seraphin, C. Beeli, J.-M. Bonard, J. Jiao, P. Stadelmann, and A. Châtelain, J. Mater. Res. **14**, 2861 (1999).

[118] L. D. Bianco, D. Fiorani, A. Testa, E. Bonetti, L. Savini, and S. Signoretti, Phys. Rev. B **66**, 174418 (2002).

[119] S. Signoretti, L. D. Bianco, L. Pasquini, G. Matteucci, C. Beeli, and E. Bonetti, J. Magn. Magn. Mater. **262**, 142 (2003).

[120] L. D. Bianco, D. Fiorani, A. Testa, E. Bonetti, L. Savini, and S. Signoretti, J. Magn. Magn. Mater. **262**, 128 (2003).

[121] L. Savini, E. Bonetti, L. D. Bianco, l. Pasquini, S. Signoretti, P. Allia, M. Coisson, J. Moya, V. Selvaggini, P. Tiberto, and F. Vinai, J. Appl. Phys. **91**, 8593 (2002).

[122] C. Granquist and R. Burham, J. Appl. Phys. **47**, 2200 (1976).

[123] H. Gleiter, J. Appl. Cryst **24**, 79 (1991).

[124] L. Savini, PhD Thesis, University of Bologna, 2002.

[125] R. Flagan, in *Nanostructured Materials, Science & Technology-NATO ASI Series*, edited by G. Chow and N. N. Eds. (Kluver Academic Publisher, The Netherlands, 1998), p. 15.

[126] L. Lutterotti and P. Scardi, J. Appl. Cryst. **23**, 246 (1990).

[127] H. Rietveld, Acta Crystallogr. **20**, 508 (1966).

[128] A. M. K. Haneda, Nature **282**, 186 (1979).

[129] S. Gangopadhyay, G. Hadjipanayis, B. Dale, C. Sorensen, K. Klabunde, V. Papaefthymiou, and A. Kostikas, Phys. Rev. B **45**, 9778 (1992).

[130] R. Kadoma, A. Berkowitz, E. McNiff, and S. Foner, Phys. Rev. Lett. **77**, 394 (1996).

[131] J. Coey, Phys. Rev. Lett. **27**, 1140 (1971).

[132] J. Mydosh, J. Magn. Magn. Mater. **200**, 606 (1996).

[133] J. Loffler, J. Meier, B. Doudin, J. Ansermet, and W. Wagner, Phys. Rev. B **57**, 2915 (1998).

[134] E. Stoner and E. Wohlfarth, Proc. Phys. Soc. A **240**, 599 (1948).

[135] P. Stadelmann, Ultramicroscopy **21**, 131 (1987).

[136] A. Hubert and R. Schäfer, *Magnetic Domains* (Springer Verlag, Berlin, 1998), p. 168.

[137] R. Dunin-Borkowski, M. McCartney, B. Kardynal, and D. Smith, J. Appl. Phys. **84**, 374 (1998).

[138] S. Porthun, L. Abelmann, and C. Lodder, J. Magn. Magn. Mater. **182**, 238 (1998).

[139] G. Heydon, A. Farley, E. Hoon, O. Valera, and S. Tomlinson, IEEE on Trans. Magnet. **33**, 4059 (1997).

[140] L. Kong and S. Chou, J. Appl. Phys. **81**, 5026 (2000).

[141] P. Van-Schendel, H. Hug, B. Stiefel, S. Martin, and H.-J. Güntherodt, J. Appl. Phys. **88**, 435 (2000).

[142] U. Hartmann, Adv. Electron. Electron Phys. **47**, 49 (1994).

[143] H. Hug, P. van Schendel, A. Moser, R. Hofer, S. Martin, H.-J. Güntherodt, S. Porthun, L. abelmann, J. Lodder, G. Bochi, and R. O'Handley, J. Appl. Phys. **83**, 5609 (1998).

[144] S. Tomlinson and A. Farley, J. Appl. Phys. **81**, 5029 (1997).

[145] K. Sueoka, F. Sai, K. Parker, and T. Arnoldussen, J. Vac. Sci. Technol. B **12**, 1618 (1994).

[146] J. Scott, S. McVitie, R. Ferrier, and A. Gallagher, J. Phys. D: Appl. Phys. **34**, 1326 (2001).

[147] R. Ferrier, S. McVitie, A. Gallagher, and W. Nicholson, IEEE on Trans. Magnet. **33**, 4062 (1997).

[148] G. Matteucci, M. Muccini, and U. Hartmann, Phys. Rev. B **50**, 6823 (1994).

[149] D. Streblechenko, M. Scheinfein, M. Mankos, and K. Badcock, IEEE on Trans. Magnet. **32**, 4124 (1996).

[150] B. Frost, N. vam Hulst, E. Lunedei, G. Matteucci, and E. Rikkers, Appl. Phys. Lett. **68**, 1865 (1996).

[151] M. Rürig, S. Porthun, J. Lodder, S. McVitie, L. Heyderman, A. Johnston, and J. Chapman, J. Appl. Phys. **79**, 2913 (1996).

[152] S. Liou, Y. Liu, S. Malhotra, M. Yu, and D. Sellmyer, J. Appl. Phys. **79**, 5060 (1996).

[153] A. Darling, Plat. Met. Rev. **7**, 96 (1963).

[154] R. MacGuire and P. Gaunt, Phil. Magn. **13**, 567 (1966).

[155] G. Hadjipanayis, J. Appl. Phys. **50**, 2358 (1979).

[156] P. Becker and P. Coppens, Acta Cryst. **A 46**, 254 (1990).

[157] J. Spence, Acta Cryst. **A 49**, 231 (1993).

[158] S. Myake, Proc. Phys.-Math. Soc. Jpn **22**, 666 (1940).

[159] K. Yada, K. Shibata, and T. Hibi, J. Electron Microscopy **22**, 223 (1973).

[160] G. Möllensted and M. Keller, Zeitschrift für Physik **148**, 34 (1957).

[161] R. Buhl, Zeitschrift für Physik **155**, 395 (1959).

[162] H. Hoffmann and C. Jönsson, Zeitschrift für Physik **182**, 360 (1965).

[163] C. Jönsson, H. Hoffmann, and G. Möllensted, Phys. Kondens. Mater. **3**, 193 (1965).

[164] M. Keller, Zeitschrift für Physik **164**, 274 (1961).

[165] Y. Wang, T. Chou, M. Libera, E. Voelkl, and B. Frost, Microsc. Microanal. **4**, 146 (1998).

[166] M. Dariel, L. Bennett, D. Lashmore, P. Lubitz, and M. Rubinstein, J. Appl. Phys **61**, 4067 (1987).

[167] C. Ross, Ann. Rev. Mater. Sci. **24**, 159 (1994).

[168] M. Moskovits, U.S. Patent 5,202,290, 1993.

[169] J. Spence and J. Zuo, *Electron Microdiffraction* (Plenum Press, New York, 1992), pp. 31, 104.

[170] J. Pendry, *Low Energy Electron Diffraction* (Academic Press, Boston, 1974), pp. 32, 262.

[171] D. Saldin and J. Spence, Ultramicroscopy **55**, 397 (1994).

[172] M. V. Hove, W. Weinberg, and C.-M. Chan, *Low-Energy Electron Diffraction* (Springer, Berlin, 1986), p. 132.

[173] C. Ahn and O. Krivanek, in *EELS Atlas*, edited by C. Ahn and O. Krivanek (Gatan Inc., Warrendale, PA, 1983).

[174] R. Trebble and D. Craik, *Magnetic Materials* (Wiley-Interscience, London, 1969), pp. 33–35.

Acknowledgments

Without friendship there is no life.
Cicero

In these three years at the ETH I learned that a PhD is more than scientific work, namely an opportunity both to gain experience in a field of research and to get to know unique people, who leave a lasting impression on you. It has been a great privilege to meet special people also outside the ETH, all of them contributing to make these three years very special.

I would like to acknowledge foremost Prof. Dr. H. R. Ott because he gave me the opportunity to work in his group.

Special thanks go to Conradin Beeli for his help and for introducing me to the world of electron microscopy and especially the fascinating field of electron holography. I would like to express my gratitude and admiration to Roland Wessicken and Peter Wägli, who, besides offering technical support, were always there to help and giving me good advice or lending their shoulder! Many thanks to Christian Soltmann for his helping hand any time I was looking for it.

The presence of a team of interesting and friendly people provided me with an optimal atmosphere to have an enjoyable stay in the institute. So I would like to thank May Chiao, Gerald Wigger, Matthias Weller, René Monnier, Jorge Gavilano, Igor Landau, Erich Felder, Shpent Mushkolaj, Dominik Rau, Stefan Siegrist, Hans Thomas, Bill Pedrini, Alexandr Sologubenko, Ingreed Heer and Doris Amstad. Although Maria Luisa

van der Mark is no longer part of the group, she deserves a special acknowledgment for being so kind to me and for being my mother when I needed a mother in Zurich! Thanks for still giving me advice and showing me your friendship!

I am indebted to the people of my former group in Bologna, with whom I did my Diploma thesis and with whom I have continued a fruitful collaboration. In this respect I thank Prof. Ennio Bonetti for all kinds of support that he gave me. In particular I would like to address my special thanks to Dr. Lucia Del Bianco, mostly for being the best friend I ever had, for all the love that could possibly be in a friendship and for all the attention and care she gave me during the last 5 years. Thanks to her unusual capability for teaching I was able to learn the most important and more difficult aspects of research. I'm grateful to Dr. Luca Pasquini and Dr. Lorenzo Savini for their collaboration and active participation in the work done in the framework of this thesis. Special thanks go to Dr. Giorgio Matteucci for fruitful discussion and for his help during the preparation of the thesis.

Thanks al mio gigante buono Paolo because you have always encouraged me to go on. Thank you for what we have always shared together. To Mafalda and Cesare I express all my gratitude and admiration for their love and for following me in every step of these experience and for caring so much for me. I love you all.

Thanks Konrad! Thank you for your great help, your support and your love. Un bacio, una carezza ed un sorriso per te!

I have here the opportunity to thank all my friends, brilliant people that have shared so many experiences with me and with whom I could enjoy my time in Zurich. All of them contributed to my happiness here:
The Cirillo's team (Roberto, Mary and Carlo), Francesca Quattrini, Rebecca Taraborrelli, Fabio Torrisi, Andrea Gentilini, Monica Bollani, Monique Calisti, Stefano Piotto, Marta Brozzi, Gabriel Sphüler, Alessandro Butté, Donal Whooley, Mathias Terheggen and Sam Broderick (not only for the best pancakes I ever had!). Thanks to all the special people whom I met through the Kosta: Stefan, Rebecca, Johannes and Chrigu. A particular acknowledgment to Frank and Sophie for loving me and caring for me so much!

Infine, rivolgo i miei ringraziamenti più profondi a tutta la mia famiglia. Ai miei genitori per avermi sempre dato la possibilità di soddisfare i miei desideri con la più

grande libertà. Per essere stati i migliori genitori di questa terra pronti a soccorermi e ad ascoltarmi in ogni momento. Al mio saggio fratello maggiore Enrico e a Giorgia che hanno contribuito alla realizzazione di tutto questo e che si occuperanno della mia formazione in barca a vela!

Curriculum Vitae

5 February 1975	Born in Pesaro, Italy
1981-1986	Primary school in Pesaro, Italy
1986-1989	College in Pesaro, Italy
1989-1994	High School in Pesaro, Italy
July 1994	Maturity type C
1994-1999	Study in Physics at the University of Bologna, Italy
October 1999	Diploma thesis in Solid State Physics at the University of Bologna and Universite' de Paris VII, France, supervised by Prof. E. Bonetti on *"Synthesis and Characterization of Fe/Fe_3O_4 Nanocrystalline Systems"*
2000-2003	Research and teaching assistance at the Laboratory for Solid State Physics of the ETH Zürich in the group of Prof. Dr. H. R. Ott
June 2003	Ph.D. thesis at the ETH Zürich on *"Electron Holography for the Analysis of Magnetic and Electric Microfield in Nanostructured Systems"*

List of Publications

1. S. Signoretti, L. Del Bianco, L. Pasquini, G. Matteucci, C. Beeli, E. Bonetti
   "Electron Holography of Gas-phase Condensed Fe Nanoparticles"
   J. Magn. Magn. Mater. **262**, 142, 2003

2. L. Del Bianco, D. Fiorani, A.M. Testa, E. Bonetti, L. Savini, S. Signoretti,
   "Magnetic properties of the Fe/FeOxide Granular System"
   J. Magn. Magn. Mater. **262**, 128, 2003

3. L. Del Bianco, D. Fiorani, A.M. Testa, E. Bonetti, S. Signoretti,
   "Magneto-thermal Behaviour of nanoscale Fe/FeOxide Granular System"
   Phys. Rev. B **66**, 174418, 2002

4. M. Bollani, E. Müller, S. Signoretti, C. Beeli, G. Isella, M. Kummer and H. Von Känel,
   "Compressively Strained Ge Channels on Relaxed SiGe Buffer Layers" Materials Science & Engineering B, **100**, 102, 2003

5. E. Bonetti, L. Del Bianco, L. Pasquini, G. Matteucci, C. Beeli, S. Signoretti
   "Electron Holography Investigation of Nanocrystalline Iron Particles"
   Physica Status Solidi (a) **189**, 459, 2002

6. L. Savini, E. Bonetti, L. Del Bianco, L. Pasquini, S. Signoretti, P. Allia, M. Coisson, J. Moja, V. Selvaggino, P. Tiberto, F. Vinai
   "Observation on Magnetoresistance in Core-Shell Fe-Fe Oxide Systems"
   Proceeding for the "Conference on Magnetism and Magnetic Materials", J. Appl. Phys. **91**, 8593, 2002

7. E. Bonetti, L. Del Bianco, L. Pasquini, G. Matteucci, C. Beeli, S. Signoretti
   "Thermal evolution of the magnetization in nanocrystalline Fe particles investigated by electron holography"
   J. Appl. Phys **90**, 4152, 2001

8. E. Bonetti, L. Del Bianco, L. Pasquini, G. Matteucci, C. Beeli, S. Signoretti
   "Synthesis by ball milling and characterization of nanocrystalline Fe_3O_4 and Fe/Fe_3O_4 composite system"
   J. Appl. Phys **89**, 1806, 2001